NUCLEAR ELECTROMAGNETIC CURRENTS IN CHIRAL EFFECTIVE FIELD THEORY

by

Saori Pastore
B.S. December 2002, Università degli Studi di Lecce, Italy
M.S. May 2005, Old Dominion University, Norfolk, Virginia

A Dissertation Submitted to the Faculty of
Old Dominion University in Partial Fulfillment of the
Requirement for the Degree of

DOCTOR OF PHILOSOPHY

PHYSICS

OLD DOMINION UNIVERSITY
May 2010

Approved by:

Rocco Schiavilla (Director)

John A. Adam (Member)

Sebastian E. Kuhn (Member)

Charles I. Sukenik (Member)

J. Wallace Van Orden (Member)

ABSTRACT

NUCLEAR ELECTROMAGNETIC CURRENTS IN CHIRAL EFFECTIVE FIELD THEORY

Saori Pastore
Old Dominion University, 2010
Director: Dr. Rocco Schiavilla

A nucleon-nucleon potential and consistent nuclear electromagnetic currents are derived in chiral effective field theory retaining pions and nucleons as explicit degrees of freedom. The calculation of the potential is carried out up to next-to-next-to leading order (N^2LO), while the currents include up to N^3LO corrections. The potential at N^2LO and currents at N^3LO consist of two-pion-exchange and contact contributions. The currents are then utilized to study a number of low-energy electromagnetic observables induced by magnetic dipole transitions, such as the deuteron and trinucleon magnetic moments and the np, nd, and n^3He radiative capture cross sections at thermal neutron energies. The study shows that predictions obtained within this theoretical framework are in good agreement with the experimental data.

TABLE OF CONTENTS

LIST OF TABLES

LIST OF FIGURES

CHAPTER I

INTRODUCTION

Nuclei are composite systems made up of interacting quarks and gluons. At low energies, quantum chromodynamics (QCD), the theory describing the quarks and gluons dynamics does not have a simple solution. At these energies, the strong coupling constant becomes too large and perturbative techniques cannot be applied to solve QCD. Despite the tremendous effort focused on lattice calculations of QCD, we are still far from a quantitative understanding of low-energy nuclear physics by *ab initio* calculations in terms of fundamental degrees of freedom, *i.e.* quarks and gluons.

The relevant degrees of freedom, in terms of which nuclear systems are described, are bound states of QCD, such as pions, nucleons, and Δ-isobars. The symmetries exhibited by QCD in the low-energy regime, in particular chiral symmetry, are exploited to constrain the interactions of pions among themselves and with other baryons [1]. In particular, the pion couples to these particles by powers of its momentum Q, and the Lagrangians describing these interactions can be expanded in powers of Q/M, where $M \sim 1$ GeV represents the chiral-symmetry breaking scale and characterizes the convergence of the expansion. Therefore, the effectiveness of the theory is confined to kinematic regions where the constraint $Q \ll M$ is realized. The coefficients of the chiral expansion, the so called low-energy constants (LECs), are unknown and need to be fixed by comparison with experimental data. This approach, known as chiral effective field theory (χEFT), provides an expansion of the Lagrangians in powers of a small momentum as opposed to an expansion in the strong coupling constant, restoring *de facto* the applicability of perturbative techniques also in the low-energy regime. Due to the chiral expansion it is then possible, in principle, to evaluate an observable to any degree of desired accuracy and to know *a priori* the hierarchy of interactions contributing to the (low-energy) process under study.

Since the pioneering work of Weinberg [1], this calculational scheme has been widely utilized in nuclear physics and nuclear χEFT has developed into an intense field of research. Nuclear two– and three–body interactions were first investigated by Ordòñez, Ray, and van Kolck within the standard time ordered perturbation theory (TOPT) framework [2]. More recently, a chiral two–nucleon potential has been developed by Epelbaum *et al.* in Ref. [3], where the authors derive the nuclear

potential with the method of the unitary transformation. Electroweak interactions have also been described in a χEFT formulation. Interactions of nuclei with external electroweak probes have been studied in covariant perturbation theory by Park, Min, and Rho in Refs. [4, 5].

In this work we derive the nuclear electromagnetic current operator within a χEFT formulation in which pions and nucleons are retained as relevant degrees of freedom. Heavier degrees of freedom, such as nucleons' excited states and/or heavier mesons, are 'integrated out' and their interactions are implicitly accounted for through the inclusion of contact terms. We use TOPT to evaluate the $\gamma NN \to NN$ transition amplitude. The Hamiltonians employed in the calculation are derived from the chiral Lagrangians formulated in Refs. [1, 2, 6], describing the interactions among relativistic pions and non-relativistic nucleons. The electromagnetic current operator is calculated up to next-to-next-to-next-to leading order (or N^{3}LO) in the chiral expansion. At this order, it includes up to one– and two–pion–exchange (OPE and TPE, respectively) contributions, as well as contact currents. The latter encode the short-range physics, and their strengths are specified by the unknown LECs of the theory. Some of these same LECs also enter the chiral nucleon-nucleon (NN) potential at leading (LO) and next-to-next-to leading order (N^{2}LO). Therefore, in order to determine these LECs, we derive the chiral NN potential up to N^{2}LO and constrain it to fit NN scattering data as well as deuteron static properties. The nuclear potential up to N^{2}LO describes the long-range part of the interaction via the static OPE potential. The intermediate– and short–range parts of the chiral NN potential involve TPE contributions and four-nucleon contact interactions.

An important aspect of the derivation of the electromagnetic currents and two-nucleon potential is that, in evaluating the corresponding transition amplitudes, we retain both irreducible contributions and recoil-corrected reducible ones. The latter arise from expanding the energy denominators (in reducible diagrams) in powers of nucleon kinetic energy differences to pion energies (these ratios are of order Q). Partial cancellations between the irreducible and recoil-corrected reducible contributions occur at N^{2}LO and N^{3}LO in the case of the current operator, and at N^{2}LO in the case of the potential. This approach leads to N^{3}LO electromagnetic currents which are conserved with the corresponding N^{2}LO two-body potential.

The current and nuclear potential present ultraviolet divergences which need to be removed by a proper regularization procedure. There are two kinds of regularization

employed here: the first is the usual regularization of the one loop corrections to the potential and currents, and the second is the regularization necessary for solving the Schrödinger equation and for the calculation of the current matrix elements. The former is accomplished via dimensional regularization of the loop integrals entering the TPE and loop corrections to the tree-level expressions for the potential and electromagnetic current operators. The latter is implemented through the inclusion of a short-range cutoff. The regularization of the potential and electromagnetic current operators is followed by a renormalization procedure, *i.e.* divergences isolated by the dimensional regularization scheme are reabsorbed, order by order, by the LECs entering the potential and currents. The renormalized LECs are then determined by fitting experimental data.

We use the chiral N^{3}LO electromagnetic current operator to study the magnetic moments of $A = 2$ and 3 nuclei, as well as the cross sections for the radiative capture of thermal neutrons on p, d, and ^{3}He. The capture involving $A = 3$ and 4 systems are especially interesting, since they are known to be very sensitive to both the nuclear model utilized to generate the nuclear wave functions and the many-body electromagnetic current operators [7, 8, 9, 10]. Therefore, they provide us with an important tool to test the χEFT electromagnetic currents derived in the present work. The calculation of the electromagnetic observables is carried out in the hybrid approach, that is we use the χEFT currents sandwiched between wave functions obtained from realistic potentials. Of course, intrinsic to this approach is a mismatch between the short-range behavior of the adopted realistic potential and that of the χEFT currents. This inconsistency could be avoided by using wave functions derived from the χEFT potential developed in this thesis. However, this program has yet to be implemented. Hence, in order to have an estimate of the ensuing model dependence, the variation of the predictions is studied as function of i) the short-range cutoff mentioned above, which is used to regularize the current operator, and ii) of the input potentials—either the Argonne v_{18} (AV18) [11] or chiral N^{3}LO (N3LO) [12] in combination with, respectively, the Urbana IX [13] or chiral N^{2}LO [14]—used to generate the wave functions. We will compare the results obtained in this work for the ^{2}H$(n,\gamma)^3$H and ^{3}He$(n,\gamma)^4$He cross sections with those obtained in Refs. [7, 8, 9, 15] in the conventional approach (also referred to as the standard nuclear physics approach, SNPA).

This thesis is organized into seven chapters and five appendices. In Chapter II, after defining our notation and calculational scheme, we discuss the interaction Hamiltonians obtained from chiral Lagrangians with pions, nucleons and photons, and define the power counting rules. In Chapter III we derive the renormalized chiral nuclear potential up to order Q^2 (N^{2}LO), and present the fits of the nuclear potential to the np phase shifts. The derivation of the chiral electromagnetic current operator up to order $e\,Q$ (N^{3}LO) is carried out in Chapter IV. Chapter V is devoted to the construction of the magnetic moment operator associated with the N^{3}LO currents. In Chapter VI, we present and discuss the results for the magnetic moments of $A = 2$ and 3 nuclei, and for the radiative-capture cross sections of thermal neutrons on p, d, and ^{3}He. Finally, in Chapter VII we summarize our conclusions. A number of details are relegated in the Appendices, including: expressions for the interaction Hamiltonians (Appendix A) and corresponding vertices (Appendix B); dimensional regularization of loop integrals (Appendix C); details on the evaluation of loop corrections to the OPE currents (Appendix D); and, lastly, a listing of the translationally invariant components of the magnetic moment operator associated with the N^{3}LO one-loop currents (Appendix E).

CHAPTER II

PRELIMINARIES

The nuclear two-body potential and electromagnetic current operators are obtained by considering suitable transition amplitudes, $\langle f \mid T \mid i \rangle$, where the final state $\mid f \rangle$ consists of two nucleons and the initial state $\mid i \rangle$ consists of two nucleons or two nucleons and a photon depending on whether we are dealing with the potential or electromagnetic current. We use time-ordered perturbation theory (TOPT) [16, 17] to calculate the transition amplitude:

$$\langle f \mid T \mid i \rangle = \langle f \mid H_1 \sum_{n=1}^{\infty} \left(\frac{1}{E_i - H_0 + i\,\eta} H_1 \right)^{n-1} \mid i \rangle \, , \tag{1}$$

where E_i and $E_f = E_i$ are the initial and final energies, H_0 is the Hamiltonian describing free pions and nucleons, and H_1 is the Hamiltonian describing the interactions of these particles, as well as their couplings to the electromagnetic field. In the following, because of the smallness of the electromagnetic coupling $\sqrt{\alpha}$ (α is the fine structure constant), we will treat the electromagnetic interactions in first order. We also note that the interaction Hamiltonians are expressed in the Schrödinger picture and therefore are time-independent.

This introductory Chapter is devoted to define our notation and calculational scheme. We introduce the nuclear and electromagnetic interaction Hamiltonians and specify the power counting scheme adopted in the present work.

II.1 NOTATION

Before listing the interaction Hamiltonians, it is useful to define our notation and conventions. The relativistic expressions of the isospin triplet of pion fields, $\pi_a(\mathbf{x})$, and canonical conjugates, $\Pi_a(\mathbf{x})$, are given in the Schrödinger picture [16] by

$$\pi_a(\mathbf{x}) \;=\; \sum_{\mathbf{p}} \frac{1}{\sqrt{2\,\omega_p L^3}} \left[c_{\mathbf{p},a}\, \mathrm{e}^{i\mathbf{p}\cdot\mathbf{x}} + \mathrm{h.c.} \right] \, , \tag{2}$$

$$\Pi_a(\mathbf{x}) \;=\; \sum_{\mathbf{p}} -i \sqrt{\frac{\omega_p}{2\,L^3}} \left[c_{\mathbf{p},a}\, \mathrm{e}^{i\mathbf{p}\cdot\mathbf{x}} - \mathrm{h.c.} \right] \, , \tag{3}$$

where the normalized plane waves $e^{i\mathbf{p}\cdot\mathbf{x}}/L^{3/2}$ satisfy periodic boundary conditions in a cubic box of volume L^3, $a = x, y, z$, denotes the Cartesian component in isospin

space, and $c_{\mathbf{p},a}$ and $c_{\mathbf{p},a}^{\dagger}$ respectively annihilate and create pions with momentum $\mathbf{p}$. They satisfy the following commutation relations:

$$[c_{\mathbf{p},a},\, c_{\mathbf{p}',a'}^{\dagger}] = \delta_{\mathbf{p}\,\mathbf{p}'}\,\delta_{a\,a'}\,. \tag{4}$$

The energy of the pion is given by $\omega_p \equiv (p^2 + m_\pi^2)^{1/2}$, where the pion mass $m_\pi \sim 138$ MeV is averaged over its charge states. For the time being, we neglect the effect of isospin breaking, which leads to differences between the charged and neutral pion masses. This effect will be discussed, in the case of the NN interaction, in Sec. III. The charged pion field $\pi_\pm$ is expressed in terms of Cartesian components as

$$\pi_\pm(\mathbf{x}) = \frac{1}{\sqrt{2}}\left[\pi_x(\mathbf{x}) \mp i\pi_y(\mathbf{x})\right]\,, \tag{5}$$

and π_+ (π_-) annihilates a positively (negatively) charged pion, or creates a negatively (positively) charged pion.

In Eqs. (2) and (3), a limit $L \to \infty$ is implicit. In this limit, the discrete sum over $\mathbf{p}$ is replaced by the integral below

$$\sum_{\mathbf{p}} \to L^3 \int \frac{d\mathbf{p}}{(2\pi)^3}\,. \tag{6}$$

Since physical observables do not depend on the normalization volume, we set $L^3 = 1$ throughout the rest of this work.

The nucleon field $N(\mathbf{x})$ is taken in the non-relativistic limit as

$$N(\mathbf{x}) = \sum_{\mathbf{p},\sigma\tau} b_{\mathbf{p},\sigma\tau}\, e^{i\mathbf{p}\cdot\mathbf{x}} \chi_{\sigma\tau}\,, \tag{7}$$

where $b_{\mathbf{p},\sigma\tau}$ is the annihilation operator for a nucleon with momentum $\mathbf{p}$, and spin and isospin specified by the quantum numbers σ and τ, respectively. Its canonical conjugate is $iN^{\dagger}(\mathbf{x})$. The short-hand notation $\chi_{\sigma\tau}$ is introduced to denote the spin-isospin state $\chi_\sigma \eta_\tau$. The b's and $b^{\dagger}$'s satisfy the standard anticommutation relations, appropriate for fermionic fields, $i.e.$

$$\left[b_{\mathbf{p},\sigma\tau},\, b_{\mathbf{p}',\sigma'\tau'}^{\dagger}\right]_{+} = \delta_{\mathbf{p}\mathbf{p}'}\delta_{\sigma\sigma'}\delta_{\tau\tau'}\,, \tag{8}$$

where $[\ldots,\ldots]_+$ denotes the anticommutator.

In the present non-relativistic theory, antinucleon degrees of freedom are ignored, hence no nucleon-antinucleon pair can be created or annihilated.

II.2 INTERACTION HAMILTONIANS

The Hamiltonian describing nucleons, pions, and photons, and their interactions is defined as

$$H = H_0 + H_1 \ , \tag{9}$$

where

$$H_0 = H_\pi + H_N + H_\gamma \ , \tag{10}$$

and H_π, H_N, and H_γ are the free pion, nucleon, and photon Hamiltonians, respectively, while

$$H_1 = H_{\text{strong}} + H_{\text{e.m.}} \ , \tag{11}$$

consists of H_{strong}, which describes interacting pions and nucleons, and $H_{\text{e.m.}}$ which describes their couplings to the external electromagnetic field. We derive these Hamiltonians from the χEFT Lagrangians constructed in Refs. [1, 2, 6]. Here we discuss the terms of H_1 required to evaluate the NN potential and the electromagnetic current at the order we are interested in. This statement will become clear once we define our power counting and introduce a scheme to disregard contributions which go beyond our level of required accuracy. For ease of reading, we defer the listing of the explicit expressions of the interaction Hamiltonians to Appendix A.

The strong interaction Hamiltonian consists of the following terms

$$H_{\text{strong}} \ = \ H_{\pi NN} + H_{\pi\pi NN} + H_{\text{CT0}} + \sum_{i=1,9} H_{\text{CT2},i} \ . \tag{12}$$

The interactions above are schematically represented in Fig. 1 where we denote pions and nucleons with dashed and solid lines, respectively. The πNN as well as the Weinberg-Tomozawa interaction, describing the $\pi\pi NN$ coupling, involve a derivative of the pion field. These Hamiltonians are expressed in terms of "known" LECs, *i.e.* the axial coupling constant $g_A \simeq 1.25$ and the pion decay amplitude $F_\pi \simeq 186$ MeV.

Unknown LECs enter in the four-nucleon contact interactions. Specifically, H_{CT0} is expressed in terms of two LECs, namely C_S and C_T. The contact Hamiltonians $H_{\text{CT2},i}$, denoted in the figure with a full circle, involve two derivatives acting on the nucleon fields, and they expressed in terms of fourteen LECs, here denoted as C_i', $i = 1, \ldots, 14$.
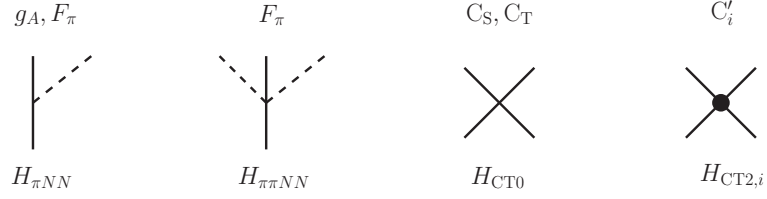
FIG. 1: Schematic representation of the strong interaction Hamiltonians involved in the calculation with indicated LECs. Pions are represented by dashed lines, and nucleons by solid lines. The solid dot represents four-nucleon contact interactions with two derivative couplings.

The electromagnetic interaction Hamiltonian has the following structure

$$
\begin{aligned}
H_{\text{e.m.}} \;=\;& H_{\gamma\pi\pi} + H_{\gamma\pi NN} + H_{\gamma\pi\pi NN} + \sum_{i=1,9} H_{\text{CT}\gamma,i} \\
+\;& H_{\gamma NN} + H^{(2)}_{\gamma\pi NN} + H_{\text{CT}\gamma,\text{nm}} \,,
\end{aligned}
\tag{13}
$$

and its individual contributions are represented in Figs. 2 and 3. The first four terms in the equation above are obtained via minimal substitution into the pion and nucleon derivative couplings entering H_0 and H_{strong}. Specifically, the $\gamma\pi\pi$, $\gamma\pi NN$, and $\gamma\pi\pi NN$ interactions are obtained from H_π, $H_{\pi NN}$, $H_{\pi\pi NN}$ by gauging the spatial derivatives acting on the pion field:

$$
\nabla \pi_\mp(\mathbf{x}) \to \left[\nabla \mp i\,e\mathbf{A}(\mathbf{x})\right] \pi_\mp(\mathbf{x}) \,,
\tag{14}
$$

where $\pi_\pm$ are the charged pion fields defined in Eq. (5), $e\,(> 0)$ is the electric charge, and $\mathbf{A}(\mathbf{x})$ is the transverse photon field in Coulomb gauge. The latter is expanded as

$$
\mathbf{A}(\mathbf{x}) = \sum_{\mathbf{p}} \sum_{\lambda=1,2} \frac{1}{\sqrt{2\omega_p}} \left[a_{\mathbf{p},\lambda}\, \mathrm{e}^{i\mathbf{p}\cdot\mathbf{x}}\, \hat{\mathbf{e}}_{\mathbf{p},\lambda} + \text{h.c.} \right] \,,
\tag{15}
$$

and the linear polarization (unit) vectors $\hat{\mathbf{e}}_{\mathbf{p},1}$, $\hat{\mathbf{e}}_{\mathbf{p},2}$ form along with $\hat{\mathbf{p}}$ a right-handed orthonormal system of axes, $\hat{\mathbf{e}}_{\mathbf{p},1} \times \hat{\mathbf{e}}_{\mathbf{p},2} = \hat{\mathbf{p}}$.

The contact electromagnetic Hamiltonians $H_{\text{CT}\gamma,i}$ are obtained from the $H_{\text{CT2},i}$ via minimal substitution into the nucleon derivative couplings

$$
\nabla N(\mathbf{x}) \to \left[\nabla - i\,e\,e_N \mathbf{A}(\mathbf{x})\right] N(\mathbf{x}) \,,
\tag{16}
$$

$$H_{\gamma\pi\pi} \qquad\qquad H_{\gamma\pi NN} \qquad\qquad H_{\gamma\pi\pi NN} \qquad\qquad H_{\mathrm{CT}\gamma,i}$$
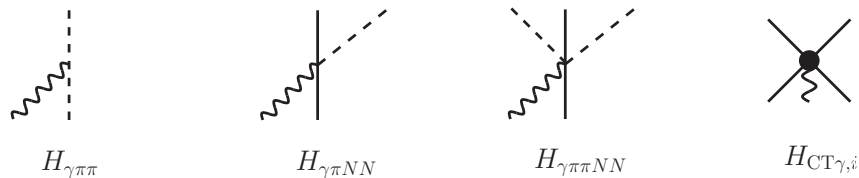
FIG. 2: Schematic representation of the minimal electromagnetic interaction Hamiltonians involved in the calculation. Notation is as in Fig. 1 but for the wavy lines which denote photons.

where $e_N = (1 + \tau_z)/2$.

We refer to the electromagnetic Hamiltonians generated by gauging the derivative couplings as 'minimal' Hamiltonians. The LECs involved in these interactions, are the same as those entering the strong sector.

The gauging of space-time derivatives is not sufficient to reproduce all the electromagnetic interactions compatible with the symmetries satisfied by the underlying theory. In addition, one has to account for interactions involving the electromagnetic field tensor (a gauge invariant quantity) $F_{\mu\nu} = (\partial_\mu A_\nu - \partial_\nu A_\mu)$. The Hamiltonians describing these interactions are referred to as 'non-minimal', and involve additional LECs which are not constrained by the strong interactions. In particular, at the order we are interested in, there are three 'non-minimal' electromagnetic Hamiltonians—the last three terms in Eq. (13). The γNN Hamiltonian is obtained by considering the non-relativistic limit of the corresponding covariant single-nucleon Hamiltonian, as specified in Appendix A. The resulting γNN interaction consists of a 'minimal' and a 'non-minimal' term. The former is obtained by gauging the derivative couplings entering the free-nucleon Hamiltonian. The 'non-minimal' interaction is expressed in terms of the proton and neutron anomalous magnetic moments ($\kappa_p = 1.793$ n.m. and $\kappa_n = -1.931$ n.m.). Thus this Hamiltonian is already determined by the experimental data. The $H^{(2)}_{\gamma\pi NN}$ Hamiltonian involves two derivatives, one acting on the pion field and the other on the photon field, and is expressed in terms of the LECs d'_8, d'_9, and d'_{21}. Lastly, the 'non-minimal' electromagnetic contact Hamiltonian $H_{\mathrm{CT}\gamma,\mathrm{nm}}$ involves two additional LECs, *i.e.* C'_{15} and C'_{16}.

9

10

$$\mu_p, \mu_n \qquad\qquad d'_8, d'_9, d'_{21} \qquad\qquad C'_{15}, C'_{16}$$

$$H_{\gamma NN} \qquad\qquad H^{(2)}_{\gamma\pi NN} \qquad\qquad H_{\mathrm{CT}\gamma,\mathrm{nm}}$$
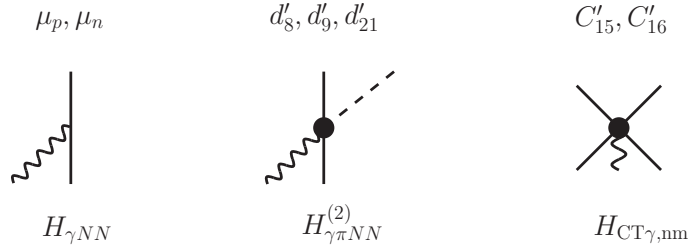
FIG. 3: Schematic representation of non-minimal electromagnetic interaction Hamiltonians involved in the calculation with indicated LECs. Notation is as in Fig. 2.

II.3 TRANSITION AMPLITUDE IN TIME ORDERED PERTURBATION THEORY

The evaluation of the transition amplitude is carried out, in practice, by inserting complete sets of eigenstates of H_0 between successive terms of H_1 in the expansion defined in Eq. (1), *i.e.*

$$\langle f \mid T \mid i \rangle = \langle f \left| H_1 \right| i \rangle + \sum_{I_1} \langle f \left| H_1 \right| I_1 \rangle \frac{1}{E_i - E_1 + i\,\eta} \langle I_1 \left| H_1 \right| i \rangle$$
$$+ \sum_{I_1, I_2} \langle f \left| H_1 \right| I_2 \rangle \frac{1}{E_i - E_2 + i\,\eta} \langle I_2 \left| H_1 \right| I_1 \rangle \frac{1}{E_i - E_1 + i\,\eta} \langle I_1 \left| H_1 \right| i \rangle + \ldots, \quad (17)$$

where $\mid I_1 \rangle$ and $\mid I_2 \rangle$ are eigenstates of H_0 with energies E_1 and E_2, respectively, and H_1 is the interaction Hamiltonian defined in Sec. II.2. The n-th order of the perturbative series has n vertices $\langle I_j \left| H_1 \right| I_i \rangle$, and $(n-1)$ energy denominators of the form $(E_i - E_j + i\,\eta)^{-1}$, with $j = 1, \ldots, (n-1)$.

As an example, we discuss in detail the following second order term of the transition amplitude, which involves two πNN interaction Hamiltonians:

$$\mathcal{A} = \sum_I \langle f \left| H_{\pi NN} \right| I \rangle \frac{1}{E_i - E_I + i\,\eta} \langle I \left| H_{\pi NN} \right| i \rangle. \qquad (18)$$

To this end, we introduce a simplified notation for the nucleon states. We drop the spin-isospin indices, thus a nucleon with momentum $\mathbf{p}_i$ has spin-isospin quantum

numbers σ_i, τ_i, and spin-isospin state χ_i. For example, in this notation the two-nucleon initial and final states read

$$
\begin{aligned}
\mid i\rangle &= \mid \mathbf{p}_1, \chi_1; \mathbf{p}_2, \chi_2\rangle = b_{\mathbf{p}_1}^\dagger\, b_{\mathbf{p}_2}^\dagger \mid 0\rangle, \\
\mid f\rangle &= \mid \mathbf{p}_1', \chi_1'; \mathbf{p}_2', \chi_2'\rangle = b_{\mathbf{p}_1'}^\dagger\, b_{\mathbf{p}_2'}^\dagger \mid 0\rangle,
\end{aligned}
\tag{19}
$$

where $\mid 0\rangle$ represents the vacuum state (no mesons and nucleons are present).

Insertion of the explicit expressions for the pion and nucleon fields in the πNN interaction Hamiltonian of Eq. (235) in Appendix A.1 leads to

$$
\begin{aligned}
H_{\pi NN} &= i\frac{g_A}{F_\pi} \sum_{\mathbf{p}_i \mathbf{p}_j} \sum_{\mathbf{k}',b} \frac{1}{\sqrt{2\,\omega_{k'}}} \chi_i^\dagger\, \mathbf{k}' \cdot \boldsymbol{\sigma}\, \tau_b\, \chi_j \\
&\quad \times \left[\int d\mathbf{x}\, e^{-i\,(\mathbf{p}_i - \mathbf{p}_j - \mathbf{k}') \cdot \mathbf{x}}\, b_{\mathbf{p}_i}^\dagger\, b_{\mathbf{p}_j}\, c_{\mathbf{k}',b} - \int d\mathbf{x}\, e^{-i\,(\mathbf{p}_i - \mathbf{p}_j + \mathbf{k}') \cdot \mathbf{x}}\, b_{\mathbf{p}_i}^\dagger\, b_{\mathbf{p}_j}\, c_{\mathbf{k}',b}^\dagger \right] \\
&= i\frac{g_A}{F_\pi} \sum_{\mathbf{p}_i \mathbf{p}_j} \sum_{\mathbf{k}',b} \frac{1}{\sqrt{2\,\omega_{k'}}} \chi_i^\dagger\, \mathbf{k}' \cdot \boldsymbol{\sigma}\, \tau_b\, \chi_j \\
&\quad \times \left[\delta_{\mathbf{p}_i - \mathbf{p}_j, \mathbf{k}'}\, b_{\mathbf{p}_i}^\dagger\, b_{\mathbf{p}_j}\, c_{\mathbf{k}',b} - \delta_{\mathbf{p}_j - \mathbf{p}_i, \mathbf{k}'}\, b_{\mathbf{p}_i}^\dagger\, b_{\mathbf{p}_j}\, c_{\mathbf{k}',b}^\dagger \right],
\end{aligned}
\tag{20}
$$

where a summation over the spins σ_i, σ_j, and isospins τ_i, τ_j, is implicit. The previous interaction Hamiltonian either annihilates or creates a pion with momentum $\mathbf{k}'$, and isospin component b. The initial and final states contain only two nucleons, and hence, in order to have a non vanishing amplitude, the intermediate state $\mid I\rangle$ has to include a pion. Consequently, the complete set of eigenstates of H_0 to be inserted in between the two successive $H_{\pi NN}$ of Eq. (18) is

$$
\sum_I \mid I\rangle\langle I \mid = \frac{1}{2} \sum_{\mathbf{p}_l \mathbf{p}_m} \sum_{\mathbf{k},a} \mid b_{\mathbf{p}_l}^\dagger b_{\mathbf{p}_m}^\dagger; c_{\mathbf{k},a}^\dagger \mid 0\rangle\langle 0 \mid c_{\mathbf{k},a}; b_{\mathbf{p}_m} b_{\mathbf{p}_l} \mid,
\tag{21}
$$

where the factor $1/2$ is needed to avoid double counting, since the two-nucleon states are antisymmetrized.

We can now evaluate the vertices $\langle f \mid H_{\pi NN} \mid I\rangle$ and $\langle I \mid H_{\pi NN} \mid i\rangle$ entering the amplitude of Eq. (18), in particular

$$
\begin{aligned}
\langle f \mid H_{\pi NN} \mid \mathbf{p}_l, \chi_l; \mathbf{p}_m, \chi_m; \mathbf{k}, a\rangle &= -i\frac{g_A}{F_\pi} \sum_{\mathbf{p}_i \mathbf{p}_j} \sum_{\mathbf{k}',b} \frac{1}{\sqrt{2\,\omega_{k'}}} \chi_i^\dagger\, \mathbf{k}' \cdot \boldsymbol{\sigma}\, \tau_b\, \chi_j\, \delta_{\mathbf{p}_j - \mathbf{p}_i, \mathbf{k}'} \\
&\quad \times \langle 0 \mid b_{\mathbf{p}_2'} b_{\mathbf{p}_1'}\, b_{\mathbf{p}_i}^\dagger b_{\mathbf{p}_j}\, b_{\mathbf{p}_l}^\dagger b_{\mathbf{p}_m}^\dagger\, c_{\mathbf{k}',b} c_{\mathbf{k},a}^\dagger \mid 0\rangle \\
&= -i\frac{g_A}{F_\pi} \frac{1}{\sqrt{2\omega_k}} \Big[\chi_{1'}^\dagger\, \mathbf{k} \cdot \boldsymbol{\sigma}\, \tau_a\, \chi_l\, \delta_{\mathbf{p}_l - \mathbf{p}_1', \mathbf{k}}\, \delta_{\mathbf{p}_2', \mathbf{p}_m} - \chi_{2'}^\dagger\, \mathbf{k} \cdot \boldsymbol{\sigma}\, \tau_a\, \chi_l\, \delta_{\mathbf{p}_l - \mathbf{p}_2', \mathbf{k}}\, \delta_{\mathbf{p}_1', \mathbf{p}_m} \\
&\quad + \chi_{2'}^\dagger\, \mathbf{k} \cdot \boldsymbol{\sigma}\, \tau_a\, \chi_m\, \delta_{\mathbf{p}_m - \mathbf{p}_2', \mathbf{k}}\, \delta_{\mathbf{p}_1', \mathbf{p}_l} - \chi_{1'}^\dagger\, \mathbf{k} \cdot \boldsymbol{\sigma}\, \tau_a\, \chi_m\, \delta_{\mathbf{p}_m - \mathbf{p}_1', \mathbf{k}}\, \delta_{\mathbf{p}_2', \mathbf{p}_l} \Big],
\end{aligned}
\tag{22}
$$

where we used the standard commutation (anticommutation) relations of boson (fermion) fields to reduce the product of $c_{\mathbf{k},a}$'s ($b_{\mathbf{p}_i}$'s) operators. Note that only the $c_{\mathbf{k}',b}$ term in the $H_{\pi NN}$ Hamiltonian of Eq. (20) contributes to the previous matrix element. Similarly, we find

$$
\begin{aligned}
&\langle \mathbf{p}_l, \chi_l; \mathbf{p}_m, \chi_m; \mathbf{k}, a \mid H_{\pi NN} \mid i \rangle \\
&= i\frac{g_A}{F_\pi} \frac{1}{\sqrt{2\,\omega_{k_a}}} \Big[\chi_l^\dagger \, \mathbf{k} \cdot \boldsymbol{\sigma}\, \tau_a\, \chi_1\, \delta_{\mathbf{p}_l'-\mathbf{p}_1,\mathbf{k}}\, \delta_{\mathbf{p}_2,\mathbf{p}_m} - \chi_l^\dagger \, \mathbf{k} \cdot \boldsymbol{\sigma}\, \tau_a\, \chi_2\, \delta_{\mathbf{p}_l-\mathbf{p}_2,\mathbf{k}}\, \delta_{\mathbf{p}_1',\mathbf{p}_m} \\
&+ \chi_m^\dagger\, \mathbf{k} \cdot \boldsymbol{\sigma}\, \tau_a\, \chi_2\, \delta_{\mathbf{p}_m-\mathbf{p}_2,\mathbf{k}}\, \delta_{\mathbf{p}_1,\mathbf{p}_l'} - \chi_m^\dagger\, \mathbf{k} \cdot \boldsymbol{\sigma}\, \tau_a\, \chi_1\, \delta_{\mathbf{p}_m-\mathbf{p}_1,\mathbf{k}}\, \delta_{\mathbf{p}_2,\mathbf{p}_l} \Big] .
\end{aligned}
\tag{23}
$$

Nucleons are treated non-relativistically, and the initial energy E_i, and the energy E_I of the intermediate state are

$$
\begin{aligned}
E_i &= E_1 + E_2 = 2m_N + \frac{p_1^2}{2\,m_N} + \frac{p_2^2}{2\,m_N} , \\
E_I &= E_l + E_m + \omega_k = 2m_N + \frac{p_l^2}{2m_N} + \frac{p_m^2}{2m_N} + \omega_k ,
\end{aligned}
\tag{24}
$$

where m_N denotes the nucleon mass. In fact, we adopt the static limit approximation, i.e. $m_N \to \infty$, and neglect the nucleons' kinetic energies for the time being. Thus, in this limit the energy denominator entering the amplitude of Eq. (18) becomes

$$
\frac{1}{(E_i - E_I + i\eta)} \bigg|_{\text{static}} = \frac{1}{-\omega_k} .
\tag{25}
$$

Combining the results obtained so far, we find the following amplitude

$$
\begin{aligned}
\mathcal{A} &= \frac{1}{2} \sum_{\mathbf{p}_l\, \mathbf{p}_m} \sum_{\mathbf{k},a} \langle f \mid H_{\pi NN} \mid b_{\mathbf{p}_l}^\dagger b_{\mathbf{p}_m}^\dagger; c_{\mathbf{k},a}^\dagger \mid 0 \rangle \frac{1}{-\omega_k} \langle 0 \mid c_{\mathbf{k},a}; b_{\mathbf{p}_m} b_{\mathbf{p}_l} \mid H_{\pi NN} \mid i \rangle \\
&= -\frac{g_A^2}{F_\pi^2} \sum_{\mathbf{k},a} \frac{1}{2\,\omega_k^2} \Big[\chi_{1'}^\dagger\, \mathbf{k} \cdot \boldsymbol{\sigma}\, \tau_a\, \chi_1\; \chi_{2'}^\dagger\, \mathbf{k} \cdot \boldsymbol{\sigma}\, \tau_a\, \chi_2\; \delta_{\mathbf{p}_2-\mathbf{p}_2',\mathbf{k}} \delta_{\mathbf{p}_1'-\mathbf{p}_1,\mathbf{k}} \\
&+ \chi_{1'}^\dagger\, \mathbf{k} \cdot \boldsymbol{\sigma}\, \tau_a\, \chi_1\; \chi_{2'}^\dagger\, \mathbf{k} \cdot \boldsymbol{\sigma}\, \tau_a\, \chi_2\; \delta_{\mathbf{p}_1-\mathbf{p}_1',\mathbf{k}} \delta_{\mathbf{p}_2'-\mathbf{p}_2,\mathbf{k}} - (\text{exchange terms}) \Big] \\
&- \frac{g_A^2}{F_\pi^2} \sum_{\mathbf{k},a} \sum_{\mathbf{p}_l} \frac{1}{2\,\omega_k^2} \chi_{1'}^\dagger\, (\mathbf{k} \cdot \boldsymbol{\sigma}\, \tau_a)^2\, \chi_1\; \delta_{\mathbf{p}_1'+\mathbf{k},\mathbf{p}_l}\, \delta_{\mathbf{p}_1+\mathbf{k},\mathbf{p}_l}\, \delta_{\mathbf{p}_2',\mathbf{p}_2} \\
&- \frac{g_A^2}{F_\pi^2} \sum_{\mathbf{k},a} \sum_{\mathbf{p}_m} \frac{1}{2\,\omega_k^2} \chi_{2'}^\dagger\, (\mathbf{k} \cdot \boldsymbol{\sigma}\, \tau_a)^2\, \chi_2\; \delta_{\mathbf{p}_2'+\mathbf{k},\mathbf{p}_m}\, \delta_{\mathbf{p}_2+\mathbf{k},\mathbf{p}_m}\, \delta_{\mathbf{p}_1',\mathbf{p}_1} ,
\end{aligned}
\tag{26}
$$

where the exchange terms are derived by making the substitution $(\mathbf{p}_1', \sigma_1', \tau_1') \rightleftharpoons (\mathbf{p}_2', \sigma_2', \tau_2')$, and changing the overall sign. The terms of the amplitude $\mathcal{A}$ can be represented by the diagrams shown in Fig. 4. These diagrams can also be regarded
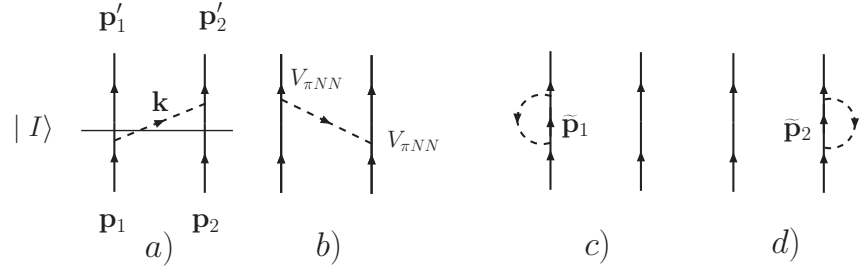
FIG. 4: The time-ordered diagrams in panels a) and b) illustrate one-pion exchange contributions to the transition amplitude. The disconnected diagrams in panels b) and c) illustrate "self-energy" nucleon corrections. Notation is as in Fig. 1.

as time-ordered diagrams in which the time increases from down to up. The first two terms of $\mathcal{A}$, ignoring the exchange in the final state, are represented by one-pion exchange (OPE) time-ordered diagrams in panels a) and b). The Kronecker's delta $\delta_{\mathbf{p}'_i,\mathbf{p}_i}$ in the last two terms of $\mathcal{A}$ indicates that one of the nucleons is not interacting. These terms are represented by the disconnected diagrams of panels c) and d).

In the expression given in Eq. (26), a limit $L^3 \to \infty$ is implicit, which implies

$$\sum_{\mathbf{p}_i} \;\; \to \;\; \int \frac{d\mathbf{p}_i}{(2\pi)^3} \equiv \int_{\mathbf{p}_i}, \tag{27}$$

$$\delta_{\mathbf{p}_i,\mathbf{p}_j} \;\; \to \;\; (2\pi)^3 \delta(\mathbf{p}_i - \mathbf{p}_j) \equiv \bar{\delta}(\mathbf{p}_i - \mathbf{p}_j). \tag{28}$$

After making the above substitutions in the amplitude $\mathcal{A}$, and summing over the isospin components a of the pion field, we find

$$
\begin{aligned}
\mathcal{A} \;=\; & -\frac{g_A^2}{F_\pi^2} \, \boldsymbol{\tau}_1 \cdot \boldsymbol{\tau}_2 \, \frac{\mathbf{k} \cdot \boldsymbol{\sigma}_1 \, \mathbf{k} \cdot \boldsymbol{\sigma}_2}{\omega_k^2} \, \bar{\delta}(\mathbf{p}'_1 + \mathbf{p}'_2 - \mathbf{p}_1 - \mathbf{p}_2) \\
& - \frac{g_A^2}{F_\pi^2} \int_{\mathbf{k}} \frac{1}{2\,\omega_k^2} \, \boldsymbol{\tau}_1^2 \, (\mathbf{k} \cdot \boldsymbol{\sigma}_1)^2 \, \bar{\delta}(\mathbf{p}'_1 - \mathbf{p}_1)\bar{\delta}(\mathbf{p}'_2 - \mathbf{p}_2) \\
& - \frac{g_A^2}{F_\pi^2} \int_{\mathbf{k}} \frac{1}{2\,\omega_k^2} \, \boldsymbol{\tau}_2^2 \, (\mathbf{k} \cdot \boldsymbol{\sigma}_2)^2 \, \bar{\delta}(\mathbf{p}'_2 - \mathbf{p}_2) \, \bar{\delta}(\mathbf{p}'_1 - \mathbf{p}_1) \Big] \\
=\; & \mathcal{A}_{\text{OPE}} + \mathcal{A}_{\text{disconnect}}, \tag{29}
\end{aligned}
$$

where the operator $\boldsymbol{\sigma}_i$ ($\boldsymbol{\tau}_i$) acts on the spin (isospin) state of nucleon i, with $i = 1, 2$, and we indicate with $\mathcal{A}_{\text{OPE}}$ the OPE amplitude—first line of Eq. (29)—and with $\mathcal{A}_{\text{disconnect}}$ the amplitude of the disconnected contributions—last two lines of Eq. (29).

The actual calculation of the transition amplitude is highly simplified once its contributions are identified with time-ordered diagrams. To clarify this point, consider the amplitude associated with the OPE contribution. We start off by drawing all the possible time-ordered diagrams. Since there are two vertices, there are 2! time-ordered diagrams, which are illustrated in panels a) and b) of Fig. 4. We fix the direction of the initial and final nucleon momenta, as well as that of the virtual pion momentum, and associate with the vertices the following matrix elements implied by the πNN interaction Hamiltonian

$$V_{\pi NN}(j, \mathbf{k}) = \langle \mathbf{p}'_j, \chi'_j; \mathbf{k}, a \mid H_{\pi NN} \mid \mathbf{p}_j, \chi_j, \rangle = -i \frac{g_A}{F_\pi} \frac{\boldsymbol{\sigma}_j \cdot \mathbf{k}}{\sqrt{2\,\omega_k}} \tau_{j,a} \bar{\delta}(\mathbf{k} + \mathbf{p}'_j - \mathbf{p}_i), \quad (30)$$

where $j = 1, 2$ indicates that the pion with momentum $\mathbf{k}$, and isospin component a, is hooked up with nucleon j. Note that this vertex describes the emission of a pion, while the vertex associated with the absorption of a pion has the same structure as that one given above, but for the overall sign due to $\mathbf{k} \to -\mathbf{k}$. The $\bar{\delta}(\dots)$ function follows from the momentum conservation at each vertex. In the static limit, the energy denominator $-1/\omega_k$ is associated with the intermediate state, and an integration over all the possible momenta of each virtual pion must be included. Therefore, the OPE amplitude results from the sum of the amplitudes described by the two time-ordered diagrams in panels a) and b) of Fig. 4, *i.e.*

$$
\begin{aligned}
\mathcal{A}_{\text{OPE}} &= \int_{\mathbf{k}} V_{\pi NN}(2, \mathbf{k}) \frac{1}{-\omega_k} V_{\pi NN}(1, \mathbf{k}) + \int_{\mathbf{k}} V_{\pi NN}(1, \mathbf{k}) \frac{1}{-\omega_k} V_{\pi NN}(2, \mathbf{k}) \\
&= -2 \frac{g_A^2}{F_\pi^2} \int_{\mathbf{k}} \boldsymbol{\tau}_1 \cdot \boldsymbol{\tau}_2 \frac{\mathbf{k} \cdot \boldsymbol{\sigma}_1 \, \mathbf{k} \cdot \boldsymbol{\sigma}_2}{2\,\omega_k^2} \, \bar{\delta}(\mathbf{k} + \mathbf{p}'_1 - \mathbf{p}_1) \bar{\delta}(\mathbf{k} + \mathbf{p}'_2 - \mathbf{p}_2) \\
&= -\frac{g_A^2}{F_\pi^2} \boldsymbol{\tau}_1 \cdot \boldsymbol{\tau}_2 \frac{\mathbf{k} \cdot \boldsymbol{\sigma}_1 \, \mathbf{k} \cdot \boldsymbol{\sigma}_2}{\omega_k^2} \, \bar{\delta}(\mathbf{p}'_1 + \mathbf{p}'_2 - \mathbf{p}_1 - \mathbf{p}_2),
\end{aligned}
\quad (31)
$$

where $\mathbf{k} = \mathbf{p}'_1 - \mathbf{p}_1 = \mathbf{p}_2 - \mathbf{p}'_2$. Thus the OPE potential (OPEP) in the static limit is defined as

$$v_\pi(\mathbf{k}) = \mathcal{A}_{\text{OPE}} = -\frac{g_A^2}{F_\pi^2} \boldsymbol{\tau}_1 \cdot \boldsymbol{\tau}_2 \frac{\mathbf{k} \cdot \boldsymbol{\sigma}_1 \, \mathbf{k} \cdot \boldsymbol{\sigma}_2}{\omega_k^2}, \quad (32)$$

where we dropped the $\bar{\delta}(\dots)$ indicating an overall momentum conservation. Diagrams like those illustrating the OPE are called tree diagrams. In this type of contributions the momenta of the intermediate states are fixed via momentum conservation by the momenta of the initial and final states.

We apply the method described above to evaluate the amplitude $\mathcal{A}_{\text{disconnect}}$. Again, we start off by drawing the time-ordered diagrams. Consider the diagram
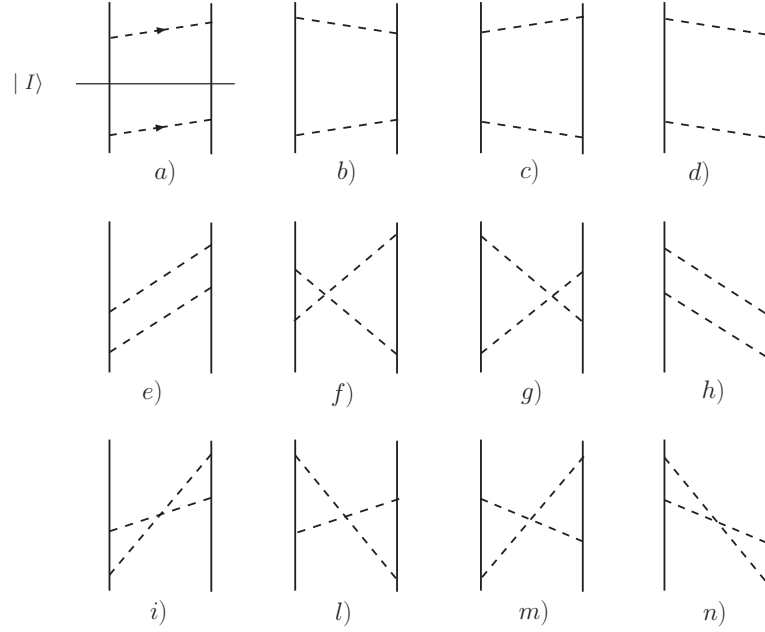
FIG. 5: Time-order diagrams for the two-pion exchange amplitude. Notation is as in Fig. 1.

in panel c) of Fig. 4. In principle, there should be another time-ordered diagram obtained by switching the order of the vertices. In fact, such a diagram would give the same contribution as the original one illustrated in panel c), therefore it does not enter the amplitude. In this diagram, there are two virtual particles, the pion with momentum $\mathbf{k}$, and the nucleon with momentum $\widetilde{\mathbf{p}}_1$, as shown in the figure. Therefore, we have to account for an integration over the pion momenta, as well as an integration over the nucleon momenta. A similar argument applies to the contribution in panel d) of Fig. 4. The amplitude $\mathcal{A}_{\text{disconnect}}$ is then given by

$$
\begin{aligned}
\mathcal{A}_{\text{disconnect}} &= -\int_{\widetilde{\mathbf{p}}_1}\int_{\mathbf{k}} V_{\pi NN}(1,\mathbf{k})\frac{1}{\omega_k}V'_{\pi NN}(1,\mathbf{k})\bar{\delta}(\mathbf{p}'_2 - \mathbf{p}_2) \\
&\quad - \int_{\widetilde{\mathbf{p}}_2}\int_{\mathbf{k}} V_{\pi NN}(2,\mathbf{k})\frac{1}{\omega_k}V'_{\pi NN}(2,\mathbf{k})\bar{\delta}(\mathbf{p}'_1 - \mathbf{p}_1) \\
&= -\frac{g_A^2}{F_\pi^2}\int_{\mathbf{k}}\frac{1}{2\,\omega_k^2}\,\boldsymbol{\tau}_1^2\,(\mathbf{k}\cdot\boldsymbol{\sigma}_1)^2\,\bar{\delta}(\mathbf{p}'_1 - \mathbf{p}_1)\bar{\delta}(\mathbf{p}'_2 - \mathbf{p}_2) \\
&\quad - \frac{g_A^2}{F_\pi^2}\int_{\mathbf{k}}\frac{1}{2\,\omega_k^2}\,\boldsymbol{\tau}_2^2\,(\mathbf{k}\cdot\boldsymbol{\sigma}_2)^2\,\bar{\delta}(\mathbf{p}'_2 - \mathbf{p}_2)\,\bar{\delta}(\mathbf{p}'_1 - \mathbf{p}_1)\,,
\end{aligned} \tag{33}
$$

where in the first two lines, a $\bar{\delta}$-function in the initial and final three momenta has

been introduced to account for the non-interacting nucleon. These diagrams involve loops. In this type of contributions the momenta entering the intermediate states are not fixed by momentum conservation. Each loop is expressed in terms of one unknown momentum, and its evaluation involves an integration over all the possible values of this momentum.

We have introduced a practical calculational scheme to evaluate the contributions to the transition amplitude. Once the vertices implied by the interaction Hamiltonians listed in Appendix A are derived, the calculation of the amplitude is fairly straightforward. In Appendix B, we derived the strong and electromagnetic vertices induced by the interaction Hamiltonians. The calculation of the vertices follows that one we outlined here. In general, we distinguish between two major classes of diagrams: i) tree diagrams and ii) loops diagrams. The latter involve integrations over internal momenta. Divergences arising from the integration are removed employing dimensional regularization [18, 19, 20]. Loop diagrams in which the virtual pion is emitted and absorbed by the same nucleon, as in those shown in panels c) and d) of Fig. 4, are referred to as "self-energy" corrections.

Contributions to the transition amplitude, which involve pure nucleonic intermediate states, are referred to as reducible contributions. Those whose intermediate states involve at least one pion are called irreducible. For example, consider the two-pion exchange (TPE) 'box' contribution to the NN transition amplitude represented by the time-ordered diagrams shown in Fig. 5. Diagrams illustrated in the first row are reducible, while the remaining ones are irreducible. Reducible contributions are generated when one iterates the static OPEP into the Lippmann-Schwinger equation. Thus reducible contributions, evaluated within the static limit approximation, need to be disregarded, since they are already embedded into the iterated solution of the Lippmann-Schwinger equation (see Sec. IV.1.1). The TOPT framework enables us to correctly identify these redundant contributions, moreover it allows us to properly account for deviations from the static limit approximation. The latter are referred to as recoil corrections, and will be discussed later in this work.

II.4 POWER COUNTING

The Hamiltonians describing nuclear dynamics have been derived from χEFT Lagrangians constructed in terms of pion and nucleon degrees of freedom. Contributions arising from the inclusion of additional degrees of freedom, such as the Δ-resonance

and heavier mesons, are effectively accounted for in the LECs entering the interaction Hamiltonians. The Lagrangians provided by χEFT are expanded in powers Q/M, where $Q \ll M$ is the pion momentum-coupling and $M \sim 1$ GeV is the chiral-symmetry breaking scale and characterizes the convergence of the expansion. In principle, these Lagrangians contain an infinite number of interactions compatible with the symmetries exhibited by QCD. However, the transition amplitudes obtained from them can be expanded in terms of $(Q/M)^n$. For each given order n of the expansion, the number of terms contributing to the amplitudes is finite [1].

The NN potential (electromagnetic current) operator is related to the $NN \to NN$ ($\gamma NN \to NN$) transition amplitude given in TOPT by the perturbative series of Eq. (1). Due to the chiral expansion, we can arrange the contributions to the transition amplitude $T_{fi} = \langle f \mid T \mid i \rangle$ as

$$T_{fi} = T_{fi}^{\text{LO}} + T_{fi}^{\text{NLO}} + T_{fi}^{\text{N}^2\text{LO}} + \dots \; , \tag{34}$$

where

$$T_{fi}^{\text{N}^n\text{LO}} \sim \left(\frac{Q}{M} \right)^n T_{fi}^{\text{LO}} \; . \tag{35}$$

Each $T_{fi}^{\text{N}^n\text{LO}}$ term in the expansion above is suppressed by a factor of $(Q/M)^n$ with respect to the leading order (LO) contribution.

The power counting allows us to evaluate the scaling, with respect to Q, of the terms entering the transition amplitude. These terms are conveniently represented by time-ordered diagrams characterized by a certain number, n, of vertices, β_i pions absorbed or emitted at each vertex i, $n-1$ energy denominators, and possibly L loops. The power counting implied by the interaction Hamiltonians is easily inferred by examining the structures of the vertices listed in Appendix B. In particular, since the pion couples to nucleons, and other pions, by power of its low-momentum Q, a vertex i scales as Q^{α_i} where α_i is the power of the pion momentum, or equivalently the number of derivatives of the pion field (or of pion mass factors). The scaling of the strong interaction Hamiltonians (vertices) listed in Appendix A.1 (Appendix B.1) is reported in Table 1.

Each of the $n-1$ energy denominators, entering the contributions to the transition amplitude, involves pion energies, $\omega_k = \sqrt{k^2 + m_\pi^2}$, and differences between nucleons' energies, $\Delta E = E_i - E_I$, where E_I represents the energies of the nucleons in an intermediate state. We assume that the pion mass m_π, and its energy ω_k are of order Q, while ΔE, which involves only nucleons' kinetic energies, is suppressed by

a factor Q/M relative to the pion energy, that is $\Delta E \sim Q^2/M$. In our formulation, where we utilize the static limit approximation, the energy denominators scale as $\sim \omega_k^{-1} \sim Q^{-1}$, since the term due to ΔE vanishes in this limit. Thus the $n-1$ energy denominators are of order $\sim Q^{-(n-1)}$.

The Hamiltonians' power counting reported in Table 1 does not account for the normalization factor $1/\sqrt{2\,\omega_k}$ included in the expression of the pion field. There is one normalization factor for each pion absorbed (or emitted) at vertex i, thus an additional factor of $Q^{-\beta_i/2}$ is associated with the vertices.

	Q-scaling
$H_{\pi NN}$	Q
$H_{\pi\pi NN}$	Q
H_{CT0}	Q^0
$H_{\text{CT2},i}$	Q^2

TABLE 1: Powers of Q, the small momentum scale, associated with the vertices from the strong-interaction Hamiltonians of Sec. A.1.

Finally, loops contribute a factor Q^3 each, since they involve integrations over intermediate three momenta. Hence the power counting associated with an irreducible contribution is

$$\text{irreducible contribution} = \left(\prod_{i=1}^{n} Q^{\alpha_i - \beta_i/2}\right) \times Q^{-(n-1)} \times Q^{3L} \,, \tag{36}$$

in the static limit. Explicit inclusion of the nucleon kinetic energy differences in the evaluation of the energy denominators leads to an additional factor of Q on the r.h.s. of Eq. (36). Following the counting defined in Eq. (36), it is easy to see that the OPE amplitude evaluated in Sec. II.3—panels a) and b) of Fig. 4—scales as Q^0, and occurs at LO. In this work we evaluate the NN potential up to next-to-next-to leading order (N²LO), that is up to order Q^2 in the power counting.

Disconnected diagrams, like those illustrated in panels c) and d) of Fig. 6, are enhanced by a factor of Q^{-3}, owing to the presence of a δ-function in the initial and final three momenta of one of the two non-interacting particles. For example, panel c) of Fig. 6 $\propto \delta(\mathbf{p}_2' - \mathbf{p}_2)$, and the total scaling of this disconnected contribution is Q^0.

	Q-scaling
$H_{\gamma\pi\pi}$	$e\,Q$
$H_{\gamma\pi NN}$	$e\,Q^0$
$H_{\gamma\pi\pi NN}$	$e\,Q$
$H_{\mathrm{CT}\gamma}$	$e\,Q$
$H_{\gamma NN}$	$e\,Q$
$H^{(2)}_{\gamma\pi NN}$	$e\,Q^2$
$H_{\mathrm{CT}\gamma,\mathrm{nm}}$	$e\,Q$

TABLE 2: Powers of Q, the small momentum scale, associated with the vertices from the electromagnetic-interaction Hamiltonians of Sec. A.2.

The $\gamma NN \to NN$ transition amplitude can be schematically represented by the diagrams illustrated in Fig. 6, where we show both disconnected and connected contributions. The power counting is not affected by the introduction of the photon field and follows the relation defined in Eq. (36). The photon's energy is denoted by ω_q, and is assumed to scales as $\sim Q^2/M$. This scaling follows from energy conservation between the initial and final states, that is $E_i - E_f = \Delta E + \omega_q = 0$.
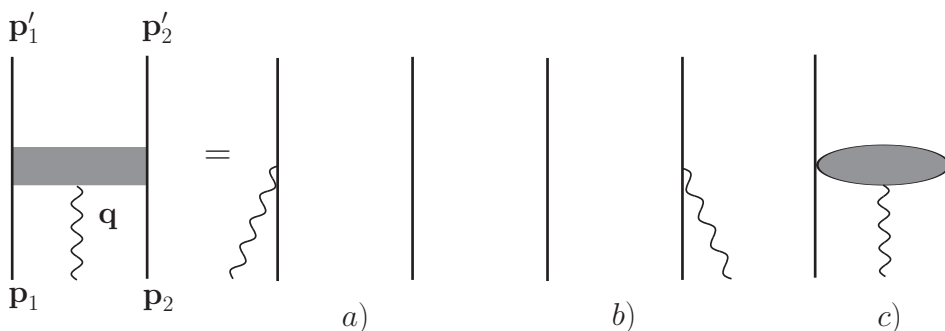
FIG. 6: Schematic representation of the disconnected, a) and b), and connected, c), contributions to the $\gamma NN \to NN$ amplitude. Notation is as in Fig. 2.

Each electromagnetic Hamiltonian scales as $e\,Q^{\alpha_i}$, where α_i is related to the power of pion or photon momenta entering the vertex, and e is the electric charge brought in by the electromagnetic coupling. The scaling of these Hamiltonians is summarized in Table 2, and can be easily inferred from the expressions of the vertices listed in Appendix B.2.

Following the power counting of Eq. (36), we can evaluate the scaling of the disconnected diagrams shown in panels a) and b) of Fig. 6. According to Table 2, the γNN vertex scales as $e\,Q$, while the δ-function in the initial and final three momenta

of the non-interacting nucleon brings in a factor of Q^{-3}, thus these diagrams scale as $e\,Q^{-2}$. These disconnected contributions are enhanced by a factor Q^{-3} relative to the connected contributions in panel c). In fact, these diagrams are the LO contributions to the nuclear electromagnetic current, which will be evaluate here up to N^{3}LO, that is up to order $e\,Q$.

CHAPTER III

NUCLEON-NUCLEON POTENTIAL IN χEFT

The main objective of the analysis reported in this chapter is to determine the LECs entering the strong Hamiltonians defined in Appendix A.1. These LECs are also present in the electromagnetic interactions implied by minimal substitution in the pion and nucleon derivative couplings, consequently they are fundamental to determine the nuclear electromagnetic current operator of interest here. In order to constrain the LECs, we derive the NN potential v_{12}, and fix these LECs so as to reproduce NN scattering data as well as deuteron static properties.

In our formulation, where nucleons are treated non-relativistically, the Hamiltonian describing the two-nucleon system consists of a term which results from the sum of the single-nucleon non-relativistic kinetic energies, and the two-body potential v_{12}

$$H = \frac{p_1^2}{2\,m_N} + \frac{p_2^2}{2\,m_N} + v_{12} \; . \tag{37}$$

The contributions to the $NN \to NN$ transition amplitude, up to order Q^2 are represented in Fig. 7. Specifically, at LO (Q^0) there is a contact interaction, panel a), along with the static OPE contribution, panel b). At N^{2}LO we distinguish among three different categories, which are: i) contact interactions involving two gradients acting on the nucleons' fields, panel c); ii) TPE loop contributions, panels d)-f); and iii) loop corrections to the LO contact interaction, panels g) and i), and to the OPE contribution, panel h). Note that in the figure we display only one among the possible time orderings.

The evaluation of the transition amplitude follows the steps outlined in Sec. II.3. Diagrams in panels a)-e) are irreducible, while those in panels f)-i) have both reducible and irreducible topologies. The evaluation of the reducible diagrams is carried out by subtracting static contributions which are already accounted for in the iterated solution of the Lippmann-Schwinger equation.

The phase-shift analysis is reported in Sec. III.3, where we list the values of the LECs obtained from the fits.
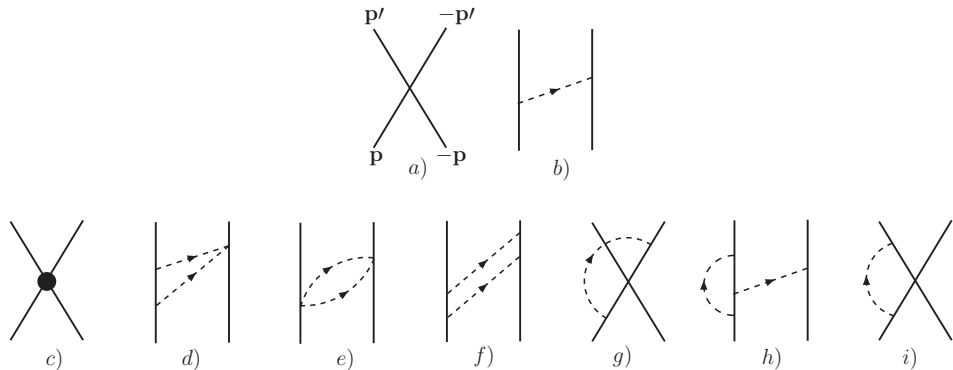
FIG. 7: Diagrams illustrating contributions to the NN potential entering at LO (Q^0), panels a) and b), and N^{2}LO (Q^2), panels c)-i). Notation is as in Fig. 1. The filled circle in panel c) represents the vertex from contact Hamiltonians containing two gradients of the nucleons' fields. Only one among the possible time orderings is shown for each contribution with more than one vertex.

III.1 NN POTENTIAL UP TO N^{2}LO: FORMAL EXPRESSIONS

In what follows, the potential is derived in the center-of-mass frame where the nucleons' initial and final relative momenta are $\mathbf{p}$ and $\mathbf{p}'$, respectively. We also define $\mathbf{k} = \mathbf{p}' - \mathbf{p}$, $\mathbf{K} = (\mathbf{p}' + \mathbf{p})/2$, and $\omega_k = \sqrt{k^2 + m_\pi^2}$.

III.1.1 Tree-Level and Contact NN Potential

We start off by evaluating the NN potential at LO. The amplitude resulting from the contact interaction Hamiltonian H_{CT0} of Eq. (237) is illustrated by the diagram in panel a) of Fig. 7 and gives rise to the LO order contact potential v^{CT0}, which is expressed in terms of the two LECs C_S and C_T as

$$v^{\mathrm{CT0}} = C_S + C_T\, \boldsymbol{\sigma}_1 \cdot \boldsymbol{\sigma}_2 \ . \tag{38}$$

The static OPEP is illustrated panel b) of Fig. 7 and has been evaluated in Sec. II.3, where we found

$$v^\pi(\mathbf{k}) = -\frac{g_A^2}{F_\pi^2}\, \boldsymbol{\tau}_1 \cdot \boldsymbol{\tau}_2\, \frac{\boldsymbol{\sigma}_1 \cdot \mathbf{k}\, \boldsymbol{\sigma}_2 \cdot \mathbf{k}}{\omega_k^2} \ . \tag{39}$$

Next we consider the contributions arising from panel c). These are implied by the contact Hamiltonians involving two gradients acting on the nucleons' fields given

in Eqs. (239)–(247), therefore the corresponding *NN* potential is of order Q^2, or N²LO. As an example, we consider the contribution due to the Hamiltonian $H_{\mathrm{CT2,1}}$. The evaluation of the vertex implied by this contact interaction has been carried out in a generic frame with nucleon $i = 1, 2$ having initial and final momenta $\mathbf{p}_i$ and $\mathbf{p}'_i$, respectively, and its expression is given in Eq. (287) of Appendix B.3. The corresponding contact potential $v^{\mathrm{CT2,1}}$ then reads

$$v^{\mathrm{CT2,1}}(\mathbf{p}_1, \mathbf{p}_2) = -2\, C'_1 \left(\mathbf{p}_1 \cdot \mathbf{p}_2 + \mathbf{p}'_1 \cdot \mathbf{p}'_2\right)\ , \tag{40}$$

which reduces to

$$v^{\mathrm{CT2,1}}(k^2, K^2) = C'_1 \left(k^2 + 4\,K^2\right)\ , \tag{41}$$

in the center-of-mass frame. Similar expressions are found for the remaining contact interactions, and the resulting contact potential at N²LO is in practice given by the sum of the matrix elements listed in Eqs. (287)–(295), evaluated in the center-of-mass frame. In this frame, it is expressed in terms of seven independent operatorial structures, each multiplied by a coefficient which is a linear combination of the C'_i LECs entering the contact interaction Hamiltonians. Specifically,

$$
\begin{aligned}
v^{\mathrm{CT2}}(\mathbf{k}, \mathbf{K}) =\ & C_1\, k^2 + C_2\, K^2 + (C_3\, k^2 + C_4\, K^2)\,\boldsymbol{\sigma}_1 \cdot \boldsymbol{\sigma}_2 + i\, C_5\, \frac{\boldsymbol{\sigma}_1 + \boldsymbol{\sigma}_2}{2} \cdot \mathbf{K} \times \mathbf{k} \\
+\ & C_6\, \boldsymbol{\sigma}_1 \cdot \mathbf{k}\, \boldsymbol{\sigma}_2 \cdot \mathbf{k} + C_7\, \boldsymbol{\sigma}_1 \cdot \mathbf{K}\, \boldsymbol{\sigma}_2 \cdot \mathbf{K}\ ,
\end{aligned}
\tag{42}
$$

where the C_i's $(i = 1, \ldots, 7)$ are linear combinations of the C'_i's $(i = 1, \ldots, 14)$, given by

$$
\begin{aligned}
C_1 &= C'_1 - C'_3 + C'_2/2\ , \\
C_2 &= 4\,C'_1 - 4\,C'_3 - 2\,C'_2\ , \\
C_3 &= C'_9 + C'_{12}/2 - C'_{14}\ , \\
C_4 &= 4\,C'_9 - 2\,C'_{12} + 4\,C'_{14}\ , \\
C_5 &= 2\,C'_5 - 4\,C'_4 - 2\,C'_6\ , \\
C_6 &= C'_7 + C'_8 + C'_{10}/2 + C'_{11}/2 - C'_{13}\ , \\
C_7 &= 4\,C'_7 + 4\,C'_8 - 2\,C'_{10} - 2\,C'_{11} + 4\,C'_{13}\ .
\end{aligned}
\tag{43}
$$

In Ref. [21] we showed that the number of C'_i is redundant, since it is possible to relate the contact interactions proportional to C'_4, C'_5, and C'_6 and those proportional to C'_7, C'_8, C'_{10}, and C'_{11} by means of partial integrations in the corresponding Lagrangians. For the sake of clarity, we utilize the same notation adopted in Ref. [2, 3], but one

should keep in mind that relations among contact interactions exist which reduce the number of independent LECs.
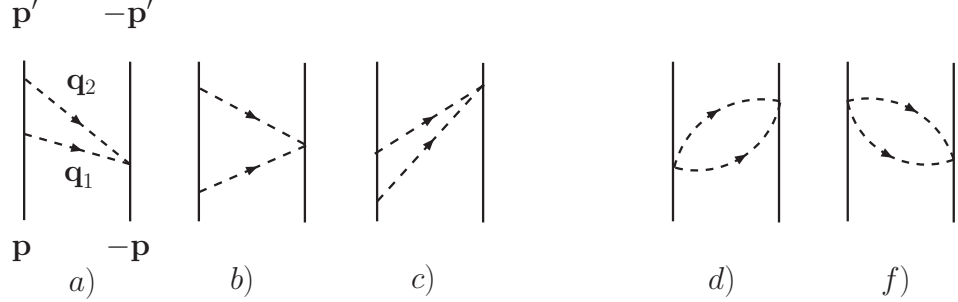
FIG. 8: Complete set of time-ordered diagrams for the TPE 'triangle' contribution, panels a)-c); complete set of time-ordered diagrams for the TPE 'football' contribution, panels d) and e). Notation is as in Fig. 1.

III.1.2   Loop Corrections to the NN Potential

Loop contributions enter at N²LO, and are represented in panels d)-i) of Fig. 7. The TPE 'triangle' and 'football' contributions illustrated in panels d) and e), respectively, are irreducible, and the complete set of time-ordered diagrams is shown in Fig. 8. The evaluation of the corresponding amplitudes leads to the following contributions

$$
\begin{aligned}
v_{\mathrm{d}}(\mathbf{k}) &= -2\frac{g_A^2}{F_\pi^4}\boldsymbol{\tau}_1 \cdot \boldsymbol{\tau}_2 \int_{\mathbf{q}_1}\int_{\mathbf{q}_2} \frac{1}{\omega_1\,\omega_2(\omega_1+\omega_2)}\bar{\delta}(\mathbf{q}_1+\mathbf{q}_2+\mathbf{k}) \\
&\times\ [\mathbf{q}_1\cdot\mathbf{q}_2 - i\boldsymbol{\sigma}_1\cdot(\mathbf{q}_1\times\mathbf{q}_2)] + (1\rightleftharpoons 2)\,, \tag{44}
\end{aligned}
$$

$$
v_{\mathrm{e}}(\mathbf{k}) = -\frac{1}{2}\frac{1}{F_\pi^4}\boldsymbol{\tau}_1\cdot\boldsymbol{\tau}_2 \int_{\mathbf{q}_1}\int_{\mathbf{q}_2} \frac{(\omega_1-\omega_2)^2}{\omega_1\,\omega_2(\omega_1+\omega_2)}\bar{\delta}(\mathbf{q}_1+\mathbf{q}_2+\mathbf{k})\,, \tag{45}
$$

where $\omega_i = (q_i^2 + m_\pi^2)^{1/2}$, and $\mathbf{q}_i$ are energies and momenta of the exchanged virtual pions, as specified in Fig. 8. The $(1\rightleftharpoons 2)$ in Eq. (44) indicates the operation of exchanging the two nucleons, thus it corresponds to exchange $(\boldsymbol{\tau}_1, \boldsymbol{\sigma}_1, \mathbf{p}, \mathbf{p}') \rightleftharpoons (\boldsymbol{\tau}_2, \boldsymbol{\sigma}_2, -\mathbf{p}, -\mathbf{p}')$. Note that the factor 1/2 multiplying the 'football' contribution—panels d and f)—is a symmetrization factor, avoiding double counting of the closed pion loop. Changing the variables of integration in the above expressions to

$$
\mathbf{P} = \mathbf{q}_1 + \mathbf{q}_2, \qquad\qquad \mathbf{p} = \mathbf{q}_1 - \mathbf{q}_2\,, \tag{46}
$$

and integrating over $\mathbf{P}$, lead to

$$v_{\mathrm{d}}(k) = \frac{g_A^2}{F_\pi^4} \boldsymbol{\tau}_1 \cdot \boldsymbol{\tau}_2 \int_{\mathbf{p}} \frac{p^2 - k^2}{\omega_+ \omega_- (\omega_+ + \omega_-)}, \tag{47}$$

$$v_{\mathrm{e}}(k) = -\frac{1}{8\,F_\pi^4} \boldsymbol{\tau}_1 \cdot \boldsymbol{\tau}_2 \int_{\mathbf{p}} \frac{(\omega_+ - \omega_-)^2}{\omega_+ \omega_- (\omega_+ + \omega_-)}, \tag{48}$$

where $\omega_\pm = \sqrt{(\mathbf{p} \pm \mathbf{k})^2 + 4\,m_\pi^2}$. Note that the term $\boldsymbol{\sigma}_1 \cdot (\mathbf{q}_1 \times \mathbf{q}_2)$ in Eq. (44) becomes, after the change of variables $\boldsymbol{\sigma}_1 \cdot (\mathbf{p} \times \mathbf{k})/2$, and gives a vanishing contribution since it is odd under $\mathbf{p} \to -\mathbf{p}$.
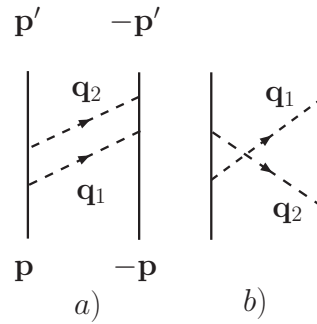
FIG. 9: Irreducible direct TPE 'box' diagram, panel a); irreducible crossed TPE 'box' diagram, panel b). Notation is as in Fig. 1. Only one among the possible time-ordered diagrams is shown.

The TPE 'box' contribution is shown in panel f) of Fig. 7. As illustrated in Fig. 5, this TPE amplitude results from 12 time-ordered diagrams, which have both irreducible and reducible parts. We start off by evaluating the transition amplitude arising from the irreducible diagrams. We utilize the same notation introduced in Sec. II.3 and denote with $V_{\pi NN}(i, \mathbf{q}_j)$ the vertex from the πNN interaction Hamiltonian relative to nucleon i and a pion with momentum $\mathbf{q}_j$. The irreducible diagrams account for the following term in the NN potential

$$v_{\mathrm{f}}^{\mathrm{irr}}(\mathbf{k}) = -2 \int_{\mathbf{q}_1} \int_{\mathbf{q}_2} \bar{\delta}(\mathbf{q}_1 + \mathbf{q}_2 + \mathbf{k}) \times$$
$$\left[\frac{1}{\omega_1 \omega_2 (\omega_1 + \omega_2)} V_{\pi NN}(2, \mathbf{q}_2) V_{\pi NN}(2, \mathbf{q}_1) V_{\pi NN}(1, \mathbf{q}_2) V_{\pi NN}(1, \mathbf{q}_1) \right.$$
$$\left. + \frac{\omega_1^2 + \omega_2^2 + \omega_1 \omega_2}{\omega_1^2 \omega_2^2 (\omega_1 + \omega_2)} V_{\pi NN}(2, \mathbf{q}_1) V_{\pi NN}(2, \mathbf{q}_2) V_{\pi NN}(1, \mathbf{q}_2) V_{\pi NN}(1, \mathbf{q}_1) \right]. \tag{49}$$

The first term in the equation above comes from the irreducible direct diagrams (in which, with reference to Fig. 9, pion 1 is absorbed before pion 2), while the second

term is from the crossed diagrams (in which pion 1 is absorbed after pion 2). In fact, the two vertex sequences entering the previous equation are the same, but for the positions of the vertices involving nucleon 2, which are switched in the crossed term.

Reducible diagrams, evaluated within the static limit approximation, lead to contributions which are embedded into the Lippmann-Schwinger equation where a static OPEP is iterated, thus we disregard the amplitude resulting from these diagrams. However, recoil corrections to the static OPEP, due to the kinetic energies of the nucleons, need to be accounted for. Recoil corrected reducible diagrams lead to terms of order Q^2 in the transition amplitude, and must be included in the evaluation of the TPE amplitude along with irreducible contributions.
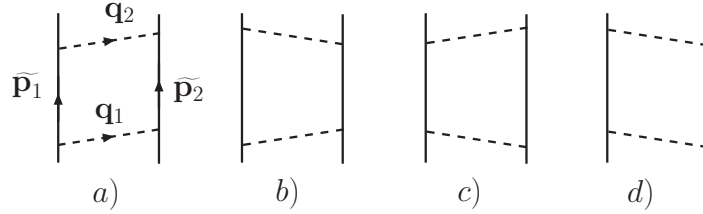
FIG. 10: Time-ordered reducible diagrams for the TPE 'box' contribution. Notation is as in Fig. 1. Only one among the possible time-ordered diagrams is shown.

The transition amplitude resulting from the reducible diagrams illustrated in Fig. 10 is given by

$$
\begin{aligned}
v_{\mathrm{f}}^{\mathrm{red}}(\mathbf{k}) &= \int_{\mathbf{q}_1} \int_{\mathbf{q}_2} \bar{\delta}(\mathbf{q}_1 + \mathbf{q}_2 + \mathbf{k}) \frac{1}{(E_i - \widetilde{E_1} - \widetilde{E_2} + i\eta)} (D_a + D_b + D_c + D_d) \\
&\times V_{\pi NN}(2, \mathbf{q}_2) V_{\pi NN}(2, \mathbf{q}_1) V_{\pi NN}(1, \mathbf{q}_2) V_{\pi NN}(1, \mathbf{q}_1) ,
\end{aligned} \tag{50}
$$

where $\widetilde{E_i}$ are the energies of the intermediate nucleons, while the D's represent the energy denominators entering the amplitudes illustrated by the diagrams of panels a)-d) of Fig. 10. The latter can be easily inferred from the figures and read

$$
\begin{aligned}
D_a &= \frac{1}{(E_i - \widetilde{E_1} - E_2 - \omega_1 + i\eta)} \frac{1}{(E_i - E_1' - \widetilde{E_2} - \omega_2 + i\eta)} , \tag{51} \\
D_b &= \frac{1}{(E_i - \widetilde{E_1} - E_2 - \omega_1 + i\eta)} \frac{1}{(E_i - \widetilde{E_1} - E_2' - \omega_2 + i\eta)} , \\
D_c &= \frac{1}{(E_i - E_1 - \widetilde{E_2} - \omega_1 + i\eta)} \frac{1}{(E_i - E_1' - \widetilde{E_2} - \omega_2 + i\eta)} , \\
D_d &= \frac{1}{(E_i - E_1 - \widetilde{E_2} - \omega_1 + i\eta)} \frac{1}{(E_i - \widetilde{E_1} - E_2' - \omega_2 + i\eta)} ,
\end{aligned}
$$

where E_1 and E_2 are the initial nucleons' energies, and E_1' and E_2' are the final nucleons' energies. Recoil corrections are obtained by expanding the energy denominators in powers of $\Delta E/\omega_i \sim Q$, where ΔE represents nucleon kinetic energy differences, and ω_i is the energy of the exchanged pion. For example, the energy denominator D_a is expanded as

$$D_a = \frac{1}{\omega_1\,\omega_2}\left[1 + \frac{E_i - \widetilde{E_1} - E_2}{\omega_1} + O(Q^2)\right]\left[1 + \frac{E_i - E_1{'} - \widetilde{E_2}}{\omega_2} + O(Q^2)\right], \quad (52)$$

and similar expressions are found for the remaining energy factors listed in Eq. (51). The sum of the energy denominators entering Eq. (50) then reads

$$D_a + D_b + D_c + D_d = \frac{2}{\omega_1\,\omega_2}\left[2 + \frac{\omega_1 + \omega_2}{\omega_1\,\omega_2}(E_i - \widetilde{E_1} - \widetilde{E_2}) + O(Q^2)\right]. \quad (53)$$

Insertion of the previous result into Eq. (50) leads to the following expression for the reducible TPE 'box' contribution

$$\begin{aligned}
v_{\mathrm{f}}^{\mathrm{red}}(\mathbf{k}) &= \int_{\mathbf{q_1}}\int_{\mathbf{q_2}} \bar{\delta}(\mathbf{q_1}+\mathbf{q_2}+\mathbf{k})\frac{1}{(E_i - \widetilde{E_1} - \widetilde{E_2} + i\eta)} \\
&\times\ V_{\pi NN}(2,\mathbf{q_2})\frac{2}{\omega_2}V_{\pi NN}(1,\mathbf{q_2})V_{\pi NN}(2,\mathbf{q_1})\frac{2}{\omega_1}V_{\pi NN}(1,\mathbf{q_1}) \\
&+\ 2\int_{\mathbf{q_1}}\int_{\mathbf{q_2}} \bar{\delta}(\mathbf{q_1}+\mathbf{q_2}+\mathbf{k})\frac{\omega_1 + \omega_2}{\omega_1^2\,\omega_2^2} \\
&\times\ V_{\pi NN}(2,\mathbf{q_2})V_{\pi NN}(2,\mathbf{q_1})V_{\pi NN}(1,\mathbf{q_2})V_{\pi NN}(1,\mathbf{q_1}). \quad (54)
\end{aligned}$$

The first term in the equation above is identified with an iteration of the static OPEP into the Lippmann-Schwinger equation, namely

$$v_{\mathrm{f}}^{\mathrm{LS}}(\mathbf{k}) = \int_{\mathbf{q_1}}\int_{\mathbf{q_2}} \bar{\delta}(\mathbf{q_1}+\mathbf{q_2}+\mathbf{k})v_\pi(\mathbf{q_2})\frac{1}{(E_i - \widetilde{E_1} - \widetilde{E_2} + i\eta)}v_\pi(\mathbf{q_1}), \quad (55)$$

where

$$v_\pi(\mathbf{q_i}) = -V_{\pi NN}(2,\mathbf{q_i})\frac{2}{\omega_i}V_{\pi NN}(1,\mathbf{q_i}) = -\frac{g_A^2}{F_\pi^2}\boldsymbol{\tau}_1\cdot\boldsymbol{\tau}_2\frac{\mathbf{q_i}\cdot\boldsymbol{\sigma}_1\,\mathbf{q_i}\cdot\boldsymbol{\sigma}_2}{\omega_i^2}. \quad (56)$$

The N²LO recoil corrected reducible contribution is given by the second term in Eq. (54), that is

$$\begin{aligned}
v_{\mathrm{f}}^{\mathrm{rec}}(\mathbf{k}) &= 2\int_{\mathbf{q_1}}\int_{\mathbf{q_2}} \bar{\delta}(\mathbf{q_1}+\mathbf{q_2}+\mathbf{k})\frac{\omega_1 + \omega_2}{\omega_1^2\,\omega_2^2} \\
&\times\ V_{\pi NN}(2,\mathbf{q_2})V_{\pi NN}(2,\mathbf{q_1})V_{\pi NN}(1,\mathbf{q_2})V_{\pi NN}(1,\mathbf{q_1}). \quad (57)
\end{aligned}$$

The TPE 'box' amplitude is obtained by combining the expression above with the N²LO irreducible contribution given in Eq.(49),

$$
\begin{aligned}
v_{\rm f}(\mathbf{k}) &= v_{\rm f}^{\rm irr}(\mathbf{k}) + v_{\rm f}^{\rm rec}(\mathbf{k}) \\
&= 2 \int_{\mathbf{q}_1} \int_{\mathbf{q}_2} \bar\delta(\mathbf{q}_1 + \mathbf{q}_2 + \mathbf{k}) \frac{\omega_1^2 + \omega_2^2 + \omega_1\,\omega_2}{\omega_1^2\,\omega_2^2(\omega_1 + \omega_2)} \\
&\times\ [V_{\pi NN}(2,\mathbf{q}_2), V_{\pi NN}(2,\mathbf{q}_1)]\, V_{\pi NN}(1,\mathbf{q}_2) V_{\pi NN}(1,\mathbf{q}_1)\ ,
\end{aligned} \tag{58}
$$

where the $[\ldots,\ldots]$ indicates a commutator. Insertion of the explicit expressions of the vertices in the previous equation gives

$$
\begin{aligned}
v_{\rm f}(\mathbf{k}) &= -\frac{2\,g_A^4}{F_\pi^4} \int_{\mathbf{q}_1} \int_{\mathbf{q}_2} \bar\delta(\mathbf{q}_1 + \mathbf{q}_2 - \mathbf{k}) \frac{\omega_1^2 + \omega_2^2 + \omega_1\,\omega_2}{\omega_1^3\,\omega_2^3(\omega_1 + \omega_2)} \\
&\times\ \left[2\,\boldsymbol{\tau}_1 \cdot \boldsymbol{\tau}_2 (\mathbf{q}_1 \cdot \mathbf{q}_2)^2 - 3\,\boldsymbol{\sigma}_1 \cdot (\mathbf{q}_1 \times \mathbf{q}_2)\boldsymbol{\sigma}_2 \cdot (\mathbf{q}_1 \times \mathbf{q}_2) \right]\ ,
\end{aligned} \tag{59}
$$

which reduces to

$$
\begin{aligned}
v_{\rm f}(\mathbf{k}) &= -\frac{g_A^4}{2\,F_\pi^4} \int_{\mathbf{p}} \frac{\omega_+^2 + \omega_+\,\omega_- + \omega_-^2}{\omega_+^3\,\omega_-^3 (\omega_+ + \omega_-)} \\
&\times\ \left[\boldsymbol{\tau}_1 \cdot \boldsymbol{\tau}_2 \, (p^2 - k^2)^2 + 6\,\boldsymbol{\sigma}_1 \cdot (\mathbf{k} \times \mathbf{p})\,\boldsymbol{\sigma}_2 \cdot (\mathbf{k} \times \mathbf{p}) \right]\ ,
\end{aligned} \tag{60}
$$

once the change of integration variables defined in Eq. (46) is made. Thus, the TPE loop diagrams of panels d)–f) of Fig. 7 generate the following contribution to the NN potential

$$
\begin{aligned}
v^{2\pi}(\mathbf{k}) &= v_{\rm d}(k) + v_{\rm e}(k) + v_{\rm f}(\mathbf{k}) \tag{61} \\
&= \frac{g_A^2}{F_\pi^4} \boldsymbol{\tau}_1 \cdot \boldsymbol{\tau}_2 \int_{\mathbf{p}} \frac{p^2 - k^2}{\omega_+\,\omega_-(\omega_+ + \omega_-)} - \frac{1}{8\,F_\pi^4} \boldsymbol{\tau}_1 \cdot \boldsymbol{\tau}_2 \int_{\mathbf{p}} \frac{(\omega_+ - \omega_-)^2}{\omega_+\,\omega_-(\omega_+ + \omega_-)} \\
&- \frac{g_A^4}{2\,F_\pi^4} \int_{\mathbf{p}} \frac{\omega_+^2 + \omega_+\,\omega_- + \omega_-^2}{\omega_+^3\,\omega_-^3(\omega_+ + \omega_-)} \left[\boldsymbol{\tau}_1 \cdot \boldsymbol{\tau}_2 \,(p^2 - k^2)^2 + 6\,\boldsymbol{\sigma}_1 \cdot (\mathbf{k} \times \mathbf{p})\,\boldsymbol{\sigma}_2 \cdot (\mathbf{k} \times \mathbf{p}) \right].
\end{aligned}
$$

The set of time-ordered diagrams, associated with the loop-corrections to the LO contact interaction illustrated in panel g) of Fig. 7, is represented in Fig. 11. We find that the irreducible diagrams—panels a) and b) in Fig. 11—account for the following contribution to the NN potential

$$
v_{\rm g}^{\rm irr} = \frac{g_A^2}{3\,F_\pi^2} \boldsymbol{\tau}_1 \cdot \boldsymbol{\tau}_2 \left[C_S\,\boldsymbol{\sigma}_1 \cdot \boldsymbol{\sigma}_2 + C_T\,(3 + 2\,\boldsymbol{\sigma}_1 \cdot \boldsymbol{\sigma}_2) \right] \int_{\mathbf{p}} \frac{p^2}{\omega_p^3}\ , \tag{62}
$$

where $\omega_p = \sqrt{p^2 + m_\pi^2}$ is the energy of the exchanged virtual pion. Recoil corrections to the reducible diagrams shown in panels c)-f) of Fig. 11 amount to

$$
v_{\rm g}^{\rm rec} = -\frac{g_A^2}{3\,F_\pi^2} \boldsymbol{\tau}_1 \cdot \boldsymbol{\tau}_2 \left[C_S\,\boldsymbol{\sigma}_1 \cdot \boldsymbol{\sigma}_2 + C_T\,(3 - 2\,\boldsymbol{\sigma}_1 \cdot \boldsymbol{\sigma}_2) \right] \int_{\mathbf{p}} \frac{p^2}{\omega_p^3}\ , \tag{63}
$$
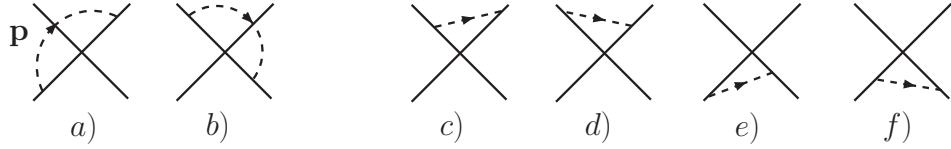
FIG. 11: Complete set of time-ordered diagrams for the loop corrections to the LO contact potential. Irreducible diagrams are shown in panels a) and b), while reducible diagrams are shown in panels c)-f). Notation is as in Fig. 1.

and the complete expression for the loop corrections to the LO contact interaction is again obtained by summing the irreducible and recoil corrected reducible contributions, given in Eq. (62) and Eq. (63), respectively,

$$v_{\text{g}} = v_{\text{g}}^{\text{irr}} + v_{\text{g}}^{\text{rec}} = \frac{4\,g_A^2}{3\,F_\pi^2}\,C_T\,\boldsymbol{\tau}_1 \cdot \boldsymbol{\tau}_2\,\boldsymbol{\sigma}_1 \cdot \boldsymbol{\sigma}_2 \int_{\mathbf{p}} \frac{p^2}{\omega_p^3}\;. \tag{64}$$

We now turn our attention to the contributions represented by the diagrams illustrated in panels h) and i) of Fig. 7. These diagrams have both reducible and irreducible parts. The former are shown in Fig. 12 and describe interactions among "dressed nucleons" involving self-energy corrections. We do not take into account recoil corrections arising from the pion emitted and reabsorbed by the same nucleon. In particular, we find the irreducible contributions illustrated in panel h) of Fig. 7 to be

$$v_{\text{h}}^{\text{irr}}(\mathbf{k}) = -\frac{g_A^4}{F_\pi^4}\,\frac{\boldsymbol{\tau}_1 \cdot \boldsymbol{\tau}_2}{\omega_k^2}\boldsymbol{\sigma}_1 \cdot \mathbf{k}\,\boldsymbol{\sigma}_2 \cdot \mathbf{k} \int_{\mathbf{p}} p^2 \left(\frac{3}{\omega_p^2\,\omega_k} + \frac{1}{3\,\omega_p^3} \right)\;, \tag{65}$$

where ω_k is the known energy of the pion exchanged by the two nucleons, and ω_p is the energy of the pion in the loop. The recoil corrections to the reducible diagram of panel a) in Fig. 12 are obtained by expanding only the energy denominator of the intermediate state with the pion exchanged by the two nucleons:

$$v_{\text{h}}^{\text{rec}}(\mathbf{k}) = \frac{g_A^4}{F_\pi^4}\,\frac{\boldsymbol{\tau}_1 \cdot \boldsymbol{\tau}_2}{\omega_k^2}\boldsymbol{\sigma}_1 \cdot \mathbf{k}\,\boldsymbol{\sigma}_2 \cdot \mathbf{k} \int_{\mathbf{p}} p^2 \frac{3}{\omega_p^2\,\omega_k}\;, \tag{66}$$

and the complete expression for the loop corrections to the OPEP is

$$v_{\text{h}}(\mathbf{k}) = v_{\text{h}}^{\text{irr}}(\mathbf{k}) + v_{\text{h}}^{\text{rec}}(\mathbf{k}) = -\frac{g_A^4}{3\,F_\pi^4}\,\frac{\boldsymbol{\tau}_1 \cdot \boldsymbol{\tau}_2}{\omega_k^2}\boldsymbol{\sigma}_1 \cdot \mathbf{k}\,\boldsymbol{\sigma}_2 \cdot \mathbf{k} \int_{\mathbf{p}} \frac{p^2}{\omega_p^3}\;. \tag{67}$$
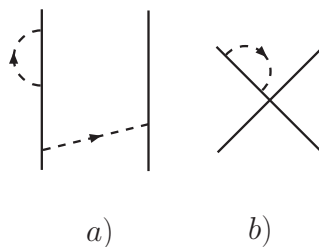
FIG. 12: Reducible diagrams involving nucleon' "self-energy" corrections. Notation is as in Fig. 1. Only one among the possible time-ordered diagrams is shown.

Lastly, for diagram i) we retain the irreducible part only of panel b) in Fig. 12, and obtain

$$v_{\rm i} \;\; \equiv \;\; v_{\rm i}^{\rm irr} = \frac{g_A^2}{F_\pi^2}\left(3\,C_S - C_T\,\boldsymbol{\sigma}_1\cdot\boldsymbol{\sigma}_2\right)\int_{\bf p}\frac{p^2}{\omega_p^3}\;. \tag{68}$$

The χEFT nuclear potential up to order Q^2 has also been derived by van Kolck *et al.* in Ref. [2] and by Epelbaum *et al.* in Ref. [3]. The former group utilized the standard TOPT formulation adopted in the present work. They explicitly considered, in addition to pion and nucleon interactions, also those involving the Δ-isobar degree of freedom. The results obtained in that work for the TPE contributions associated with the diagrams in panels d) and e) of Fig. 7 agree with those reported here. As per the amplitude related to the TPE diagram in panel f) of Fig. 7, the special treatment reserved in this work to the reducible contributions leads to a result which differs from that derived in Ref. [2]. The two expressions are in agreement if we retain only irreducible contributions.

Epelbaum and collaborators derived the nuclear potential in TOPT in combination with a unitary transformation that decouples, in the Hilbert space of nucleons and pions, the states consisting of nucleons only from those containing, in addition, pions [3]. This approach is referred to as the unitary transformation method, or projection formalism. It is interesting to note that, at least at the order we investigated so far, the unitary transformation method and TOPT with the additional prescription of accounting for recoil corrections to reducible terms are equivalent. This is true for the amplitudes implied by the diagrams illustrated in panels a)–g) of Fig. 7. Our approach leads to results which differ from those reported in Ref. [3] when applied

to the evaluation of amplitudes associated with 'self-energy' contributions, like those represented in panels h) and i) of Fig. 7. However, as it will become clear in the next section, these differences—for diagrams h) and i)—do not affect the definition of the renormalized potential, since they only lead to differences in the renormalization of the LECs C_S, C_T, and g_A.

III.2   RENORMALIZATION OF THE NN POTENTIAL

The potential defined in the previous section contains ultraviolet divergences which need to be removed by a proper renormalization procedure. In order to isolate these divergences, loop integrals (or kernels) of the N²LO contributions have been regularized with the dimensional regularization scheme [18, 20]. This scheme is commonly used within the χEFT framework since, being a momentum cutoff independent prescription, it preserves the power counting. In practice, we evaluated the three momentum loop integrals in dimension $d = 3 - \epsilon$ as shown below

$$\int_{\mathbf{p}} = \int \frac{d^3 p}{(2\pi)^3} \rightarrow \int \frac{d^{(3-\epsilon)}p}{(2\pi)^3} \mu^\epsilon \ , \tag{69}$$

where μ is a renormalization scale introduced to preserve physical dimensions. As $d \rightarrow 3$, or $\epsilon \rightarrow 0^+$, the integral becomes singular but its divergent content is easily identified with the parameter ϵ, and reabsorbed, order by order, by the LECs entering the theory. The latter are then constrained by the experimental data. The regularized kernels are obtained by studying the asymptotic behavior of the corresponding d-dimensional integrals for $\epsilon \rightarrow 0^+$. They have been derived in Appendix C where we report the relevant integration formulae and list the expressions of the regularized loop-integrals. Here we sketch the renormalization procedure of the various contributions, and give the final expression for the renormalized NN potential.

As an example, we discuss, in some detail, the regularization of the two-pion-exchange contribution of Eq. (61). In terms of the kernels $L(k)$, $I^{(2n)}(k)$ and $J^{(2n)}(k)$ defined in Appendix C, it reads as

$$
\begin{aligned}
v^{2\pi}(\mathbf{k}) = \ & -\ \frac{1}{8\,F_\pi^4}\, \boldsymbol{\tau}_1 \cdot \boldsymbol{\tau}_2 \left[L(k) - 8\,g_A^2 \Big[I^{(2)}(k) - k^2 I^{(0)}(k) \Big] + 4\,g_A^4 \Big[J^{(4)}(k) \right. \\
& \left. -\ 2\,k^2 J^{(2)}(k) + k^4 J^{(0)}(k) \Big] \right] - \frac{3\,g_A^4}{F_\pi^4}\, (\boldsymbol{\sigma}_1 \times \mathbf{k})_i (\boldsymbol{\sigma}_2 \times \mathbf{k})_j\, J^{(2)}_{ij}(\mathbf{k}). \tag{70}
\end{aligned}
$$

By inserting the explicit expressions of these kernels in the previous equation, we obtain

$$v^{2\pi}(\mathbf{k}) = \overline{v}^{2\pi}(\mathbf{k}) + \boldsymbol{\tau}_1 \cdot \boldsymbol{\tau}_2 \, P_2(k) + \left(k^2 \, \boldsymbol{\sigma}_1 \cdot \boldsymbol{\sigma}_2 - \boldsymbol{\sigma}_1 \cdot \mathbf{k} \, \boldsymbol{\sigma}_2 \cdot \mathbf{k}\right) P_0 \ , \qquad (71)$$

where the renormalized finite part of the TPE potential, denoted by $\overline{v}^{2\pi}(\mathbf{k})$, is given by

$$
\begin{aligned}
\overline{v}^{2\pi}(\mathbf{k}) \ &= \ \frac{1}{48\pi^2 \, F_\pi^4} \boldsymbol{\tau}_1 \cdot \boldsymbol{\tau}_2 \, G(k) \Bigg[4m_\pi^2 (1 + 4g_A^2 - 5g_A^4) \\
&\qquad\qquad\qquad\qquad + k^2 (1 + 10g_A^2 - 23g_A^4) - \frac{48 \, g_A^4 m_\pi^4}{4 \, m_\pi^2 + k^2} \Bigg] \\
&+ \ \frac{3 \, g_A^4}{8\pi^2 \, F_\pi^4} \, G(k) \left(k^2 \, \boldsymbol{\sigma}_1 \cdot \boldsymbol{\sigma}_2 - \boldsymbol{\sigma}_1 \cdot \mathbf{k} \, \boldsymbol{\sigma}_2 \cdot \mathbf{k}\right),
\end{aligned} \qquad (72)
$$

with the loop function $G(k)$ defined as

$$G(k) = \frac{\sqrt{4 \, m_\pi^2 + k^2}}{k} \ln \frac{\sqrt{4 \, m_\pi^2 + k^2} + k}{\sqrt{4 \, m_\pi^2 + k^2} - k} \ . \qquad (73)$$

The divergences isolated by the dimensional regularization scheme are lumped into the polynomials $P_2(k)$ (of order two) and constant P_0:

$$
\begin{aligned}
P_2(k) = &- \frac{1}{24\pi^2 \, F_\pi^4} \Bigg[m_\pi^2 \Big[4 + 22g_A^2 - 29g_A^4 - 9g_A^2(2 - 5g_A^2) \Big(-\frac{2}{\epsilon} + \gamma - \ln\pi + \ln\frac{m_\pi^2}{\mu^2} \Big) \Big] \\
&+ \frac{4}{3} k^2 \Big[1 + 7g_A^2 - 9g_A^4 - \frac{3}{8}(1 + 10g_A^2 - 23g_A^4) \Big(-\frac{2}{\epsilon} + \gamma - \ln\pi + \ln\frac{m_\pi^2}{\mu^2} \Big) \Big] \Bigg], \quad (74)
\end{aligned}
$$

$$P_0 = \frac{3 \, g_A^4}{8\pi^2 \, F_\pi^4} \left(-\frac{2}{\epsilon} + \gamma - \ln\pi + \ln\frac{m_\pi^2}{\mu^2} - \frac{4}{3} \right) \ . \qquad (75)$$

where the parameter $\epsilon \to 0^+$, γ is the Euler-Mascheroni constant, and μ is the renormalization scale brought in by dimensional regularization. The isospin structure $\boldsymbol{\tau}_1 \cdot \boldsymbol{\tau}_2$ multiplying the polynomial $P_2(k)$—Eq. (71)—can be reduced by Fierz rearrangement [22] so as to match structures occurring in the LO v^{CT0} and N²LO $v^{\mathrm{CT2}}(\mathbf{k}, \mathbf{K})$ contact contributions. A heuristic derivation exploits the antisymmetrization of the two-nucleon states. If P_{12}, P_{12}^σ, and P_{12}^τ denote respectively the space, spin, and isospin exchange operators, where

$$P_{12}^\sigma = \frac{1 + \boldsymbol{\sigma}_1 \cdot \boldsymbol{\sigma}_2}{2} \ , \qquad (76)$$

and similarly for P_{12}^τ, then $P_{12} P_{12}^\sigma P_{12}^\tau = -1$ for a two-nucleon state. Thus the isospin structure $\boldsymbol{\tau}_1 \cdot \boldsymbol{\tau}_2$ can be written as follows

$$\boldsymbol{\tau}_1 \cdot \boldsymbol{\tau}_2 = -2\, P_{12}^\sigma\, P_{12} - 1 = -2 - \boldsymbol{\sigma}_1 \cdot \boldsymbol{\sigma}_2 \ . \tag{77}$$

Similarly, the term $\boldsymbol{\tau}_1 \cdot \boldsymbol{\tau}_2\, k^2$ is reduced to

$$\boldsymbol{\tau}_1 \cdot \boldsymbol{\tau}_2\, k^2 = -2\, P_{12}^\sigma\, P_{12}\, k^2 - k^2 = -4\,(1 + \boldsymbol{\sigma}_1 \cdot \boldsymbol{\sigma}_2)\, K^2 - k^2 \ , \tag{78}$$

where we used $P_{12}\, k^2 = 4\, K^2$, which follows from the consideration that on exchanging the momenta of the nucleons $\mathbf{p}_1 \rightleftharpoons \mathbf{p}_2$, the relative momentum $\mathbf{p} \to -\mathbf{p}$.

We can now utilize the relations given in Eqs. (77) and (78) to reduce the isospin structures multiplying the polynomial $P_2(k)$. In particular, the momentum independent terms in $P_2(k)$ redefine the values of the LECs entering the contact potential at LO, *i.e.* v^{CT0} given in Eq. (38), while those which depend on k^2 contribute to the renormalization of the LECs entering the contact potential at N^{2}LO, that is $v^{\mathrm{CT2}}(\mathbf{k}, \mathbf{K})$ of Eq. (42). The renormalization constant P_0 is instead reabsorbed by the LECs entering the contact potential at N^{2}LO, since it multiplies structures which depend quadratically on the relative momentum $\mathbf{k}$—see Eq. (71). Specifically, the terms in P_0 and $P_2(k)$ renormalize the LECs C_S, C_T, C_1, C_2, C_4 and C_6. For example, the last term of Eq. (71) is absorbed by the redefinition,

$$C_6 = \overline{C}_6 + \frac{3g_A^4}{8\pi^2 F_\pi^4}\, \mu^{-\epsilon} \left(-\frac{2}{\epsilon} + \gamma - \ln\pi + \ln\frac{m_\pi^2}{\mu^2} - \frac{4}{3} \right) . \tag{79}$$

Note that the renormalized $\overline{C}_6$ remains μ-independent, as becomes obvious by taking the logarithmic derivative with respect to μ and neglecting $O(\epsilon)$ terms. For ease of notation, we will omit the overline and tacitly imply that the LECs have been properly renormalized.

The contributions in Eqs. (64), (67), and (68) lead to further renormalization of the LECs C_S and C_T, as well as the axial coupling constant g_A entering the LO OPEP:

$$v_{\mathrm{g}} + v_{\mathrm{i}} = \frac{4\, g_A^2}{3\, F_\pi^2}\, C_T\, \boldsymbol{\tau}_1 \cdot \boldsymbol{\tau}_2\, \boldsymbol{\sigma}_1 \cdot \boldsymbol{\sigma}_2\, M^{(3)} + \frac{g_A^2}{F_\pi^2}(3\, C_S - C_T\, \boldsymbol{\sigma}_1 \cdot \boldsymbol{\sigma}_2)\, M^{(3)} \ , \tag{80}$$

$$v_{\mathrm{h}}(\mathbf{k}) = -\frac{g_A^4}{3\, F_\pi^4}\, \boldsymbol{\tau}_1 \cdot \boldsymbol{\tau}_2\, \frac{\boldsymbol{\sigma}_1 \cdot \mathbf{k}\, \boldsymbol{\sigma}_2 \cdot \mathbf{k}}{\omega_k^2}\, M^{(3)} \ , \tag{81}$$

where the renormalization constants $M^{(n)}$ are listed in Appendix C. The complete renormalized NN potential up to N^{2}LO included is then given as

$$v(\mathbf{k}, \mathbf{K}) = \overline{v}^{\mathrm{CT0}} + \overline{v}^\pi(\mathbf{k}) + \overline{v}^{\mathrm{CT2}}(\mathbf{k}, \mathbf{K}) + \overline{v}^{2\pi}(\mathbf{k}) \ , \tag{82}$$

where $\overline{v}^{\text{CT0}}$, $\overline{v}^{\pi}$, $\overline{v}^{\text{CT2}}$, and $\overline{v}^{2\pi}$ are defined in Eqs. (38), (39), (42), and (72), respectively, and the overline indicates that the LECs g_A and some of the C'_i have been renormalized.

III.3   DETERMINING THE LECS: FITTING THE N²LO POTENTIAL

The *NN* potential defined in Sec. III.2 involves nine unknown LECs associated with the contact interactions entering at LO (C_S and C_T) and N²LO (C_i, $i = 1, \ldots, 7$). We determine these LECs by fitting phase-shifts obtained in the very recent (2008) analysis of *np* scattering data by Gross and Stadler [23]. To this end, we formulate the *NN* scattering- and bound-state problems in momentum space [24]. In the case of scattering, we solve for the K-matrix

$$K_{L',L}^{JTS}(p',p) = v_{L',L}^{JTS}(p',p) + \frac{4\mu_N}{\pi} \int_0^\infty \mathrm{d}k k^2 \sum_{L''} v_{L',L''}^{JTS}(p',k) \frac{\mathcal{P}}{p^2 - k^2} K_{L'',L}^{JTS}(k,p) \ , \quad (83)$$

where μ_N is the reduced mass of the two nucleon system, and $\mathcal{P}$ denotes a principal-value integration. The momentum-space matrix elements $v_{L',L}^{JTS}(p',p)$ are obtained by projecting out the N²LO potential into states with definite orbital angular momentum L, total spin S, and total angular momentum J, for each isospin channel corresponding to $T = 0, 1$ [25]. The integral equations above are discretized, and the resulting systems of linear equations are then solved by direct numerical inversion. The principal-value integration is removed by a standard subtraction technique [26]. Once the K-matrices in the various channels have been determined, the corresponding (on-shell) S-matrices are obtained from

$$S^{JTS}(p) = \left[1 + 2 i \mu_N p K^{JTS}(p,p)\right]^{-1} \left[1 - 2 i \mu_N p K^{JTS}(p,p)\right] \ , \quad (84)$$

from which phase shifts and, for coupled channels, mixing angles are determined [25]. In particular, the phase shifts δ_{JSL} in single channels ($L = J$) are related to the S-matrix via

$$S^{JTS} = e^{i \, 2\delta_{JSL}}, \quad (85)$$

while in the coupled channels ($S = 1$ and $L = J \pm 1$) the S-matrix is represented in terms of the mixing angle ϵ_J, along with the phase shifts $\delta_\pm = \delta_{J1J\pm1}$ and reads

$$S^{JTS} = \begin{pmatrix} e^{i \, 2\delta_-} \cos(2\epsilon_J) & i \, e^{i \, (\delta_- + \delta_+)} \sin(2\epsilon_J) \\ i \, e^{i \, (\delta_- + \delta_+)} \sin(2\epsilon_J) & e^{i \, 2\delta_+} \cos(2\epsilon_J) \end{pmatrix} .$$

TABLE 3: Values for the nucleon axial coupling constant g_A, pion decay constant F_π, neutral and charged pion masses m_0 and m_+, (twice) np reduced mass μ_N, and $\hbar c$, used in the fits.

g_A	F_π (MeV)	m_0 (MeV)	m_+ (MeV)	$2\,\mu_N$ (MeV)	$\hbar c$ (MeV-fm)
1.29	184.8	134.9766	139.5702	938.9181	197.32696

The bound state (with $JTS = 101$ and $L, L' = 0, 2$) is obtained from solutions of the homogeneous integral equations [24]

$$w_L(p) = \frac{1}{E_d - p^2/(2\mu_N)} \frac{2}{\pi} \int_0^\infty \mathrm{d}k\, k^2 \sum_{L'} v_{L,L'}^{101}(p, k)\, w_{L'}(k) \;, \tag{86}$$

where E_d denotes the bound state energy. From the previous equation the configuration-space S- and D-wave components follow as

$$u_L(r) = \frac{2}{\pi} \int_0^\infty \mathrm{d}p\, p^2\, j_L(pr)\, w_L(p) \;. \tag{87}$$

Before turning our attention to a discussion of the phase-shift fits, we note that the potential $v(\mathbf{k}, \mathbf{K})$ defined in Eq. (82) needs to be further regularized, since it behaves quadratically in the momenta k and/or K. The regularization is accomplished by including a high-momentum cutoff, which is conveniently chosen to be of the form

$$C_\Lambda(k, K) = \mathrm{e}^{-(k^4 + 16\,K^4)/\Lambda^4} \;, \tag{88}$$

and the matrix elements of the regularized potential entering the K-matrix and bound-state equations are obtained from

$$v^{\mathrm{R}}(\mathbf{k}, \mathbf{K}) = v(\mathbf{k}, \mathbf{K})\, C_\Lambda(k, K) \;. \tag{89}$$

The regulator defined in Eq. (88) involves momenta to the forth power. This choice does not spoil the power counting of the present potential (of order Q^2), since it generates spurious contributions of order $\sim Q^4$.

The parameters, utilized in the fitting procedure, and characterizing the OPE and TPE parts of the potential are listed in Table 3, with the nucleon axial coupling constant g_A determined from the Golberger-Treiman relation $g_A = g_{\pi NN} F_\pi/(2\, m_N)$, which relates it to the πNN coupling constant $g_{\pi NN}$. The latter is taken to have the

value $g_{\pi NN}^2/(4\pi) = 13.63 \pm 0.20$ [27, 28]. In fact, in the OPE we include the isospin-symmetry breaking induced by the mass difference between charged and neutral pions, since it leads to significant effects in the $^1S_0$ scattering length [11], and therefore the OPEP reads

$$
\begin{aligned}
\overline{v}^\pi(\mathbf{k}) &= -\frac{g_A^2}{3\,F_\pi^2}\left[\boldsymbol{\tau}_1\cdot\boldsymbol{\tau}_2\left(\frac{1}{k^2+m_0^2}+\frac{2}{k^2+m_+^2}\right)\right.\\
&\quad+\left. T_{12}\left(\frac{1}{k^2+m_0^2}-\frac{1}{k^2+m_+^2}\right)\right]\boldsymbol{\sigma}_1\cdot\mathbf{k}\,\boldsymbol{\sigma}_2\cdot\mathbf{k}\;,
\end{aligned}
\tag{90}
$$

where T_{12} is the isotensor operator defined as $T_{12} = 3\,\tau_{1,z}\tau_{2,z} - \boldsymbol{\tau}_1\cdot\boldsymbol{\tau}_2$, and m_0 and m_+ are the neutral and charged pions masses. Finally, we note that the pion mass entering in the TPE part—Eq. (72)—is taken as $m_\pi = (m_0 + 2\,m_+)/3$.

The LECs C_S, C_T, and C_i, $i = 1,\ldots,7$, are determined by fitting the deuteron binding energy and np S- and P-wave phase shifts up to 100 MeV lab energies. The fitting strategy becomes obvious once the partial wave expansion of the potential is carried out. In the case of spin-singlet ($S = 0$) channels, the contact components of the partial-wave expanded potential with JT and $S = 0$ read:

$$
v_{J,J}^{JT0}(p',p;\mathrm{CT0}/2) = \frac{1}{8\pi}\int_{-1}^{1}\mathrm{d}z\,P_J(z)\left[D_1 + D_2\,(p'^2+p^2) - 2\,D_3\,p'\,p\,z\right]C_\Lambda(p',p,z)\;,
\tag{91}
$$

where $z = \hat{\mathbf{p}}'\cdot\hat{\mathbf{p}}$, $P_J(z)$ is a Legendre polynomial, and the D_i denote linear combinations of the LECs with $D_1 = C_S - 3\,C_T$, $D_2 = C_1 - 3\,C_3 - C_6 + (C_2 - 3\,C_4 - C_7)/4$, and $D_3 = C_1 - 3\,C_3 - C_6 - (C_2 - 3\,C_4 - C_7)/4$. The cutoff function is even in z, and therefore for even (odd) J only D_1 and D_2 (D_3) contribute. In practice, D_1 and D_2 have been determined by fitting the (np) singlet scattering length (a_s) and effective range (r_s), and $^1S_0$ phase shift, while D_3 is determined by fitting the $^1P_1$ phases.

In the case of spin-triplet ($S = 1$) channels, the situation is slightly more complicated. For uncoupled channels with $J > 0$, we write

$$
\begin{aligned}
v_{J,J}^{JT1}(p',p;\mathrm{CT0}/2) &= -\frac{1}{8\pi}\int_{-1}^{1}\mathrm{d}z\left[\left[P_{J-1}(z)+P_{J+1}(z)\right](2\,D_8+D_9)\,p'\,p\right.\\
&\quad\left.-P_J(z)\left[D_4 + (D_5+D_6)\,(p'^2+p^2) - 2\,(D_7-D_8-D_9)\,p'\,p\,z\right]\right]C_\Lambda(p',p,z),
\end{aligned}
\tag{92}
$$

TABLE 4: Values of the LECs corresponding to cutoff parameters Λ in the range 500–700 MeV, obtained from fits to np phase shifts up to lab energies of 100 MeV.

	Λ (MeV)		
	500	600	700
C_S (fm^2)	-4.456420	-4.357712	-3.863625
C_T (fm^2)	0.034780	0.094149	0.234176
C_1 (fm^4)	-0.360939	-0.259186	-0.268296
C_2 (fm^4)	-1.460509	-0.934505	-0.835226
C_3 (fm^4)	-0.349780	-0.359547	-0.389047
C_4 (fm^4)	-1.968636	-1.717178	-1.724544
C_5 (fm^4)	-0.870067	-0.754021	-0.695564
C_6 (fm^4)	0.326169	0.301194	0.348152
C_7 (fm^4)	-0.727797	-1.006459	-0.955273

while for the ${}^3P_0$ channel (having $JTS = 011$)

$$v_{1,1}^{011}(p', p; \text{CT0}/2) = \frac{1}{8\pi} \int_{-1}^{1} dz \left[P_0(z) \left(2 D_8 - D_9\right) p' p \right.$$

$$\left. + P_1(z) \left[D_4 + (D_5 - D_6)(p'^2 + p^2) - (2 D_7 - D_9) p' p z \right] \right] C_\Lambda(p', p, z) . (93)$$

Here, the D_i's denote the following LEC combinations: $D_4 = C_S + C_T$, $D_5 = C_1 + C_3 + (C_2 + C_4)/4$, $D_6 = C_6 + C_7/4$, $D_7 = C_1 + C_3 - (C_2 + C_4)/4$, $D_8 = C_6 - C_7/4$, and $D_9 = C_5$. In terms of these, the contact components for coupled channels are given by

$$v_{--}^{JT1}(p', p; \text{CT0}/2) = -\frac{1}{8\pi} \int_{-1}^{1} dz \left[P_J(z) \left(\frac{2 D_8}{2J + 1} + D_9 \right) p' p \right.$$

$$\left. - P_{J-1}(z) \left[D_4 + \left(D_5 + \frac{D_6}{2J + 1} \right)(p'^2 + p^2) - (2 D_7 - D_9) p' p z \right] \right] C_\Lambda(p', p, z), (94)$$

$$v_{++}^{JT1}(p', p; \text{CT0}/2) = \frac{1}{8\pi} \int_{-1}^{1} dz \left[P_J(z) \left(\frac{2 D_8}{2J + 1} - D_9 \right) p' p \right.$$

$$\left. + P_{J+1}(z) \left[D_4 + \left(D_5 - \frac{D_6}{2J + 1} \right)(p'^2 + p^2) - (2 D_7 - D_9) p' p z \right] \right] C_\Lambda(p', p, z), (95)$$

$$v_{+-}^{JT1}(p',p;\text{CT0}/2) = -\frac{1}{4\pi}\frac{\sqrt{J(J+1)}}{2J+1}\int_{-1}^{1}dz\left[D_6\left[P_{J-1}(z)\,p'^{\,2}+P_{J+1}(z)\,p^2\right]\right.$$

$$\left.-\ 2\,D_8\,P_J(z)\,p'\,p\right]C_\Lambda(p',p,z)\ , \tag{96}$$

where $L=\pm$ is a shorthand for $L=J\pm1$, and the off-diagonal matrix element with $-+$ is obtained from $v_{+-}^{JT1}(p',p;\text{CT0}/2)$ by exchanging $p'\rightleftharpoons p$. The parameters D_4, D_5 and D_6 are then determined by fitting the deuteron binding energy (E_d), spin-triplet scattering length (a_t) and effective range (r_t), and ${}^3\text{S}_1$-${}^3\text{D}_1$ phases and mixing angle ϵ_1—the contributions of terms proportional to D_7, D_8, and D_9 vanish in this channel. On the other hand, only the latter enter into the ${}^3\text{P}_{J=0,1,2}$ channels, and the associated phases can then be used to fit D_7, D_8, and D_9.
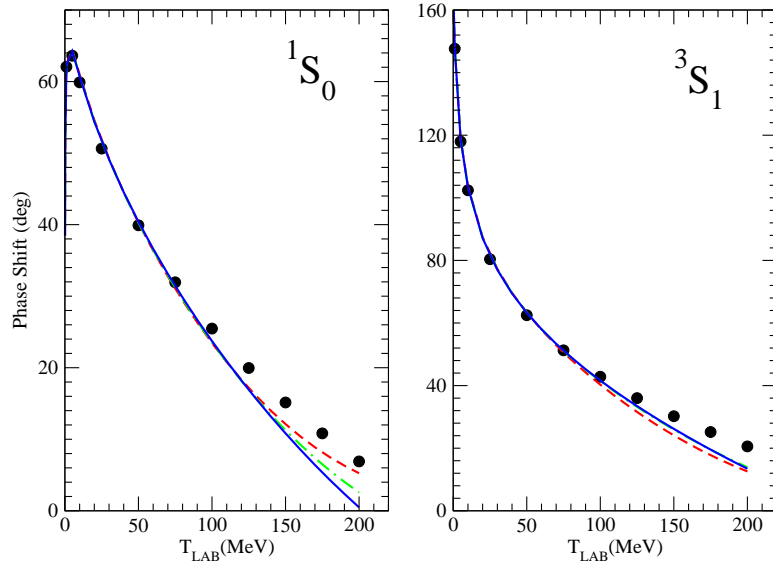
FIG. 13: The S-wave np phase shifts, obtained with cutoff parameters Λ=500, 600, and 700 MeV, are denoted by dash (red), dot-dash (green), and solid (blue) lines, respectively. The filled circles represent the phase-shift analysis of Ref. [23].

In our fits to the np-phase shifts, the cutoff parameter Λ varies in the range of 500–700 MeV. The NN potential defined in Sec. III.2 includes up to TPE contributions. Choosing the cutoff parameter Λ to vary in the range defined above corresponds to removing contributions of range $\gtrsim 2m_\pi$. The short range behavior of the potential is
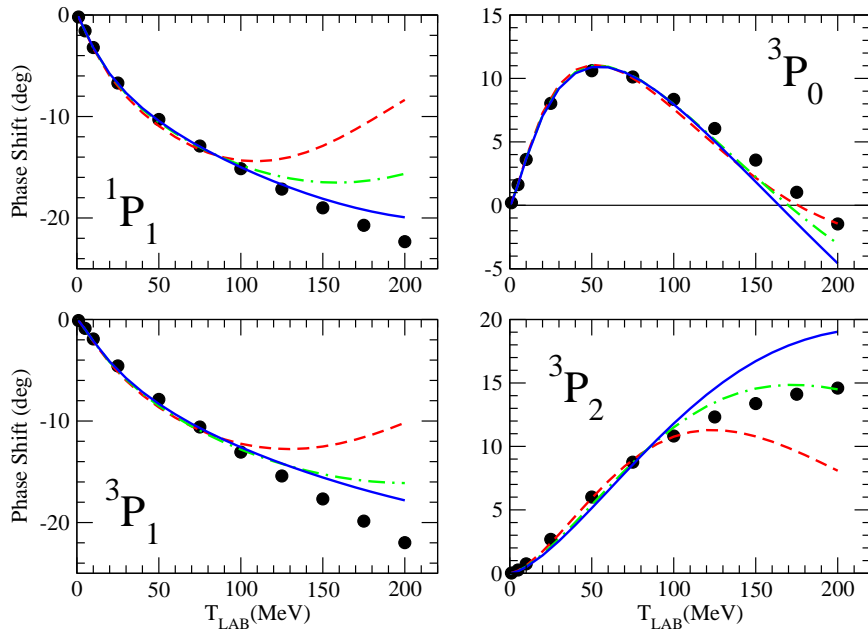
FIG. 14: Same as in Fig. 13, but for P-wave phase shifts.

represented by a set of contact terms. As already mentioned, we fit up to laboratory kinetic energies of 100 MeV, in a regime where the present χEFT formulation is expected to be valid.

In Table 4 we list the best-fit values obtained for the LECs for Λ=500, 600, and 700 MeV. The results for the S- and P-wave phases used in the fits, as well as for the D-wave and peripheral F- and G-wave phases, and mixing angles $\epsilon_{J=1,\dots,4}$ are displayed in Figs. 13–18 up to 200 MeV lab kinetic energies, while effective range expansions and deuteron properties are listed in Table 5. In Figs. 13 and 14 we show the fits to the S- and P-wave phase shifts. Of course, beyond lab energies of 100 MeV the results shown in the figures are not constrained by the fits, and hence represent predictions, although the validity of the χEFT to order Q^2 in this regime maybe questionable.

In Figs. 15–18 we show the predictions for the D-, F-, and G-wave phase shifts, and mixing angles $\epsilon_{J=1,2,3,4}$. For reference, in Figs. 15–18, following the original work
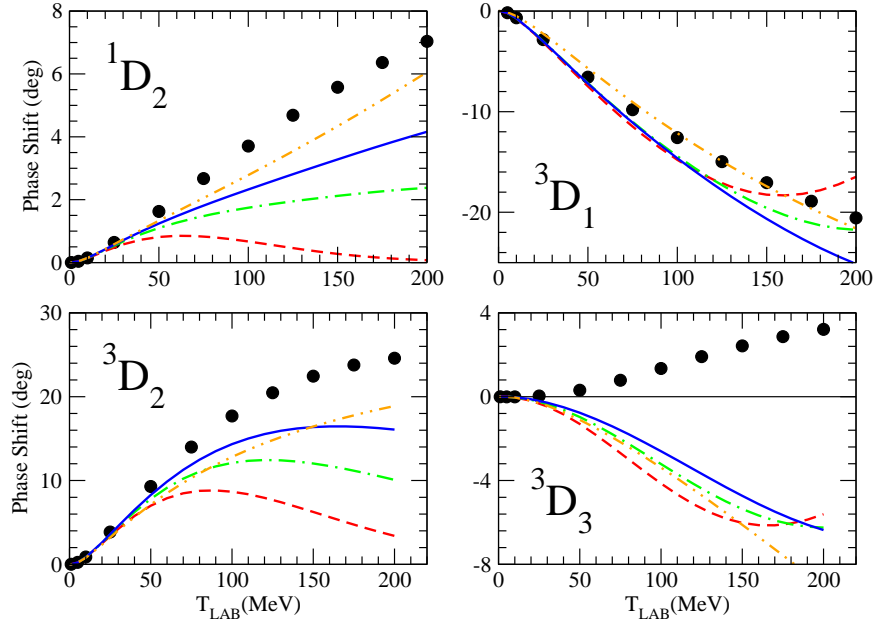
FIG. 15: Same as in Fig. 13, but for D-wave phase shifts. The dash-double-dot (orange) line is obtained in first order perturbation theory for the T-matrix by including only the one- and two-pion-exchange parts of the N^{2}LO potential.

by Kaiser *et al.* [29], the phases obtained by including only the one- and two-pion-exchange ($\overline{v}^\pi$ and $\overline{v}^{2\pi}$, respectively) terms of the potential are also shown. These have been calculated in first order perturbation theory on the T-matrix, and hence are cutoff independent. The D-, F-, and G-wave phases and the mixing angles show a significant cutoff dependence In particular, the F- and G-wave phases, while small because of the centrifugal barrier, nevertheless display a pronounced sensitivity to short-range physics. Beyond 100 MeV, the agreement between the calculated and experimental phases is generally poor, and indeed in the ^{3}D$_3$ and ^{3}F$_4$ channels they have opposite sign. Overall, the quality of the fits at N^{2}LO is comparable to that reported in Refs. [12, 25] and, more recently, in Ref. [30]. There are indications [31] that inclusion of explicit Δ-isobar degrees of freedom might reduce the sensitivity to the cutoff. There are also indications [25] that including the N^{3}LO (Q^4) corrections improves the agreement between the experimental and theoretical phase shifts. The N^{3}LO corrections include contributions arising from heavy meson exchanges and Δ-isobar excitations.
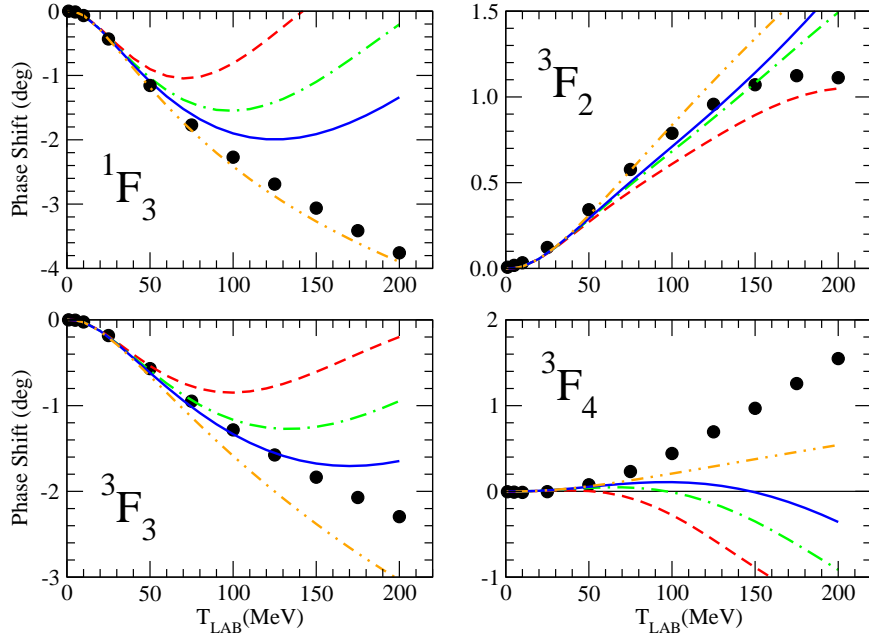
FIG. 16: Same as in Fig. 15, but for F-wave phase shifts.

The scattering lengths are well reproduced by the fits (within $\sim 1\%$ of the data, see Table 5), however, the singlet and triplet effective ranges are both significantly underpredicted, by $\sim 10\%$ and $\sim 5\%$ respectively.

The deuteron S- and D-wave radial wave functions are shown in Fig. 19 along with those calculated with the Argonne v_{18} (AV18) potential [11]. The D wave is particularly sensitive to variations in the cutoff: it is pushed in as Λ is increased from 500 to 700 MeV, but remains considerably smaller than that of the AV18 up to internucleon distances of ~ 1.5 fm, perhaps not surprisingly, since this realistic potential has a strong tensor component at short range. The static properties, *i.e.* D- to S-state ratio, mean-square-root matter radius, and magnetic moment—the binding energy is fitted—are close to the experimental values, and their variation with Λ is quite modest. The quadrupole moment is underpredicted by $\sim 4\%$, a pathology common, to the best of our knowledge, to all realistic potentials (including the AV18).
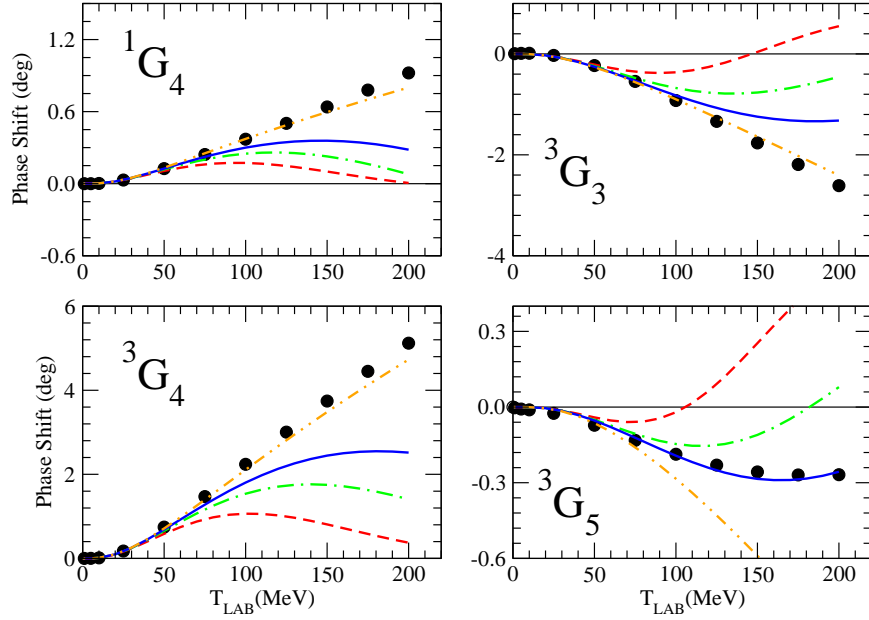
FIG. 17: Same as in Fig. 15, but for G-wave phase shifts.
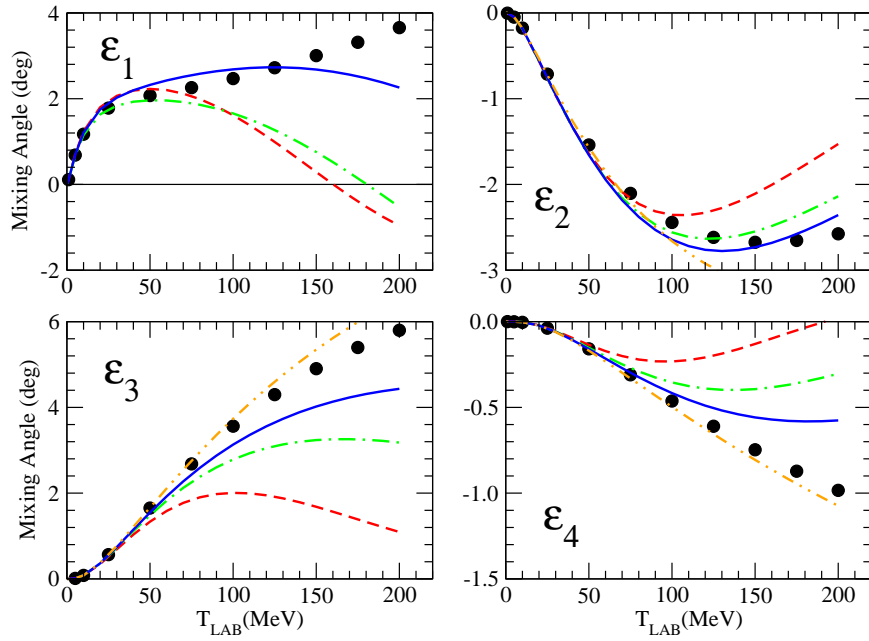
FIG. 18: Same as in Fig. 15, but for the mixing angles ϵ_J.
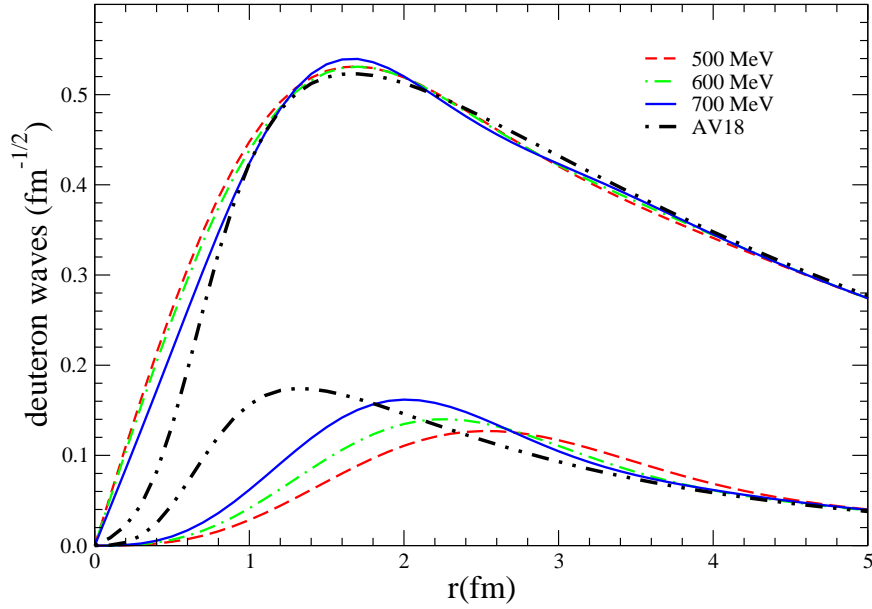
FIG. 19: The S-wave and D-wave components of the deuteron, obtained with cutoff parameters Λ=500, 600, and 700 MeV and denoted by dash (red), dot-dash (green), and solid (blue) lines, respectively, are compared with those calculated from the Argonne v_{18} potential (dash-double-dot black lines).

TABLE 5: Singlet and triplet np scattering lengths (a_s and a_t) and effective ranges (r_s and r_t), and deuteron binding energy (B_d), D- to S-state ratio (η_d), root-mean-square matter radius (r_d), magnetic moment (μ_d), quadrupole moment (Q_d), and D-state probability (P_D), obtained with Λ=500, 600, and 700 MeV, are compared to the corresponding experimental values (a_s, r_s, a_t, and r_t from Ref. [32], B_d from Ref. [33], η_d from Ref. [34], r_d and μ_d from Ref. [35], Q_d from Ref. [36]).

	Λ (MeV)			
	500	600	700	Expt
a_s (fm)	-23.729	-23.736	-23.736	-23.749(8)
r_s (fm)	2.528	2.558	2.567	2.81(5)
a_t (fm)	5.360	5.371	5.376	5.424(3)
r_t (fm)	1.665	1.680	1.687	1.760(5)
B_d (MeV)	2.2244	2.2246	2.2245	2.224575(9)
η_d	0.0267	0.0260	0.0264	0.0256(4)
r_d (fm)	1.943	1.947	1.951	1.9734(44)
μ_d (μ_N)	0.860	0.858	0.853	0.8574382329(92)
Q_d (fm^2)	0.275	0.272	0.279	0.2859(3)
P_D (%)	3.44	3.87	4.77	

III.4 CONTACT POTENTIAL IN A> 2 SYSTEMS

So far, we have derived the *NN* potential in the center-of-mass frame. In a general frame, though, in which the *NN* pair has total momentum $\mathbf{P} = \mathbf{p}_1 + \mathbf{p}_2 = \mathbf{p}'_1 + \mathbf{p}'_2 \neq 0$, the potential implied by the contact interaction Hamiltonians listed in Eqs. (239)–(247), consists of the contribution $v^{\mathrm{CT2}}(\mathbf{k}, \mathbf{K})$ of Eq. (42), plus an additional term, $v_{\mathbf{P}}^{\mathrm{CT2}}(\mathbf{k}, \mathbf{K})$, which depends on the total pair momentum $\mathbf{P}$. The N^{2}LO contact potential is easily obtained by summing up the contributions arising from the individual contact terms listed in Eqs. (287)–(295) of Appendix B.3. We express the individual nucleon momenta $\mathbf{p}_i$ and $\mathbf{p}'_i$, with $i = 1, 2$, in terms of the momenta $\mathbf{k}$, $\mathbf{K}$, and $\mathbf{P}$ as indicated below

$$
\begin{aligned}
\mathbf{p}_1 &= \frac{1}{2}(\mathbf{P} - \mathbf{k}) + \mathbf{K}, & \mathbf{p}_2 &= \frac{1}{2}(\mathbf{P} + \mathbf{k}) - \mathbf{K}, \\
\mathbf{p}'_1 &= \frac{1}{2}(\mathbf{P} + \mathbf{k}) + \mathbf{K}, & \mathbf{p}'_2 &= \frac{1}{2}(\mathbf{P} - \mathbf{k}) - \mathbf{K}.
\end{aligned}
\tag{97}
$$

Thus, contributions which depend only on the momenta $\mathbf{k}$ and $\mathbf{K}$ give rise to the potential $v^{\mathrm{CT2}}(\mathbf{k}, \mathbf{K})$ of Eq. (42), while those which depend also on the total momentum $\mathbf{P}$ lead to the following potential

$$
\begin{aligned}
v_{\mathbf{P}}^{\mathrm{CT2}}(\mathbf{k}, \mathbf{K}) &= i\, C_1^* \frac{\boldsymbol{\sigma}_1 - \boldsymbol{\sigma}_2}{2} \cdot \mathbf{P} \times \mathbf{k} + C_2^* \left(\boldsymbol{\sigma}_1 \cdot \mathbf{P}\, \boldsymbol{\sigma}_2 \cdot \mathbf{K} - \boldsymbol{\sigma}_1 \cdot \mathbf{K}\, \boldsymbol{\sigma}_2 \cdot \mathbf{P} \right) \\
&\quad + \left(C_3^* + C_4^*\, \boldsymbol{\sigma}_1 \cdot \boldsymbol{\sigma}_2 \right) P^2 + C_5^*\, \boldsymbol{\sigma}_1 \cdot \mathbf{P}\, \boldsymbol{\sigma}_2 \cdot \mathbf{P} \;,
\end{aligned}
\tag{98}
$$

where the C_i^*'s are expressed in terms of the following LECs combinations

$$
\begin{aligned}
C_1^* &= C_5'/2 + C_6'/2 \;, \\
C_2^* &= 2\, C_7' - 2\, C_8' - C_{10}' + C_{11}' \;, \\
C_3^* &= -C_1' + C_2'/2 - C_3' \;, \\
C_4^* &= -C_9' + C_{12}'/2 + C_{14}' \;, \\
C_5^* &= -C_7'/2 - C_8'/2 + C_{10}'/4 + C_{11}'/4 + C_{13}' \;.
\end{aligned}
\tag{99}
$$

We also observe that Eqs. (43) and (99) provide a one-to-one correspondence between the LECs and the coefficients of the *NN* contact potential.

In a two-body system, one can chose the frame with $\mathbf{P} = 0$, in which $v_{\mathbf{P}}^{\mathrm{CT2}}$ vanishes. However, in a nucleus with three or more nucleons, the center-of-mass of a nucleon pair will in general have motion with the respect to the center-of-mass of the whole nucleus, therefore this contribution needs to be included.

In Ref. [21], we argued that these **P**-dependent terms represent relativistic corrections to the leading order contact potential v^{CT0}. The general relation between the relativistic boost correction $\delta v(\mathbf{P})$ and the center-of-mass rest-frame interaction v has been obtained by Foldy/Krajcik [37] and by Friar [38], exploiting general principles of relativistic mechanics. In particular, by requiring that the commutation relations of the Poincaré group generators are satisfied, the boost correction up to order P^2/m_N^2, is obtained from [37, 39]

$$\delta v(\mathbf{P}) = -\frac{P^2}{8\,m_N^2}v + \frac{i}{8\,m_N^2}\left[\mathbf{P}\cdot\mathbf{r}\,\mathbf{P}\cdot\mathbf{p}\,,\,v\right] + \frac{i}{8\,m_N^2}\left[(\boldsymbol{\sigma}_1 - \boldsymbol{\sigma}_2)\times\mathbf{P}\cdot\mathbf{p}\,,\,v\right]\,, \quad (100)$$

where $\mathbf{r}$ and $\mathbf{p}$ are the relative position and momentum operators, respectively. These terms have a simple physical interpretation [39]: the first arises from the relativistic energy-momentum relation, the second from Lorentz contraction, and the third from Thomas precession of the spins.

Indeed, evaluation of the above commutators with $v = v^{\text{CT0}}$ leads in momentum space to

$$\begin{aligned}\delta v(\mathbf{P}) &= i\,\frac{C_S - C_T}{4m_N^2}\,\frac{\boldsymbol{\sigma}_1 - \boldsymbol{\sigma}_2}{2}\cdot\mathbf{P}\times\mathbf{k} + \frac{C_T}{2m_N^2}\left(\boldsymbol{\sigma}_1\cdot\mathbf{P}\,\boldsymbol{\sigma}_2\cdot\mathbf{K} - \boldsymbol{\sigma}_1\cdot\mathbf{K}\,\boldsymbol{\sigma}_2\cdot\mathbf{P}\right)\\ &\quad -\,\left(C_S + C_T\,\boldsymbol{\sigma}_1\cdot\boldsymbol{\sigma}_2\right)\frac{P^2}{4m_N^2}\,,\end{aligned} \quad (101)$$

where we kept terms up to order Q^2, and assumed $P \sim k \sim K \sim Q$.

In Ref. [40], we demonstrated that the relation given in Eq. (100) remains valid in a χEFT formulation, and established relations between C_i^* and C_S and C_T, namely

$$C_1^* = \frac{C_S - C_T}{4m_N^2}\,, \quad C_2^* = \frac{C_T}{2m_N^2}\,, \quad C_3^* = -\frac{C_S}{4m_N^2}\,, \quad C_4^* = -\frac{C_T}{4m_N^2}\,, \quad C_5^* = 0\,. \quad (102)$$

It is important to note that boost corrections to the LO potential—including those to the OPEP which can be generated via Eq. (100)—have not been studied in χEFT calculations of binding energies and scattering observables in system with $A > 2$. However, they have been evaluated for the case of realistic potentials in the $A = 3$ and 4 binding energies, where they have been found to give, respectively, about 400 keV and 1.9 MeV repulsive contributions [39], as well as in three-nucleon scattering observables [41], where, in particular, they have led to an increase of the discrepancy between theory and experiment in the nd vector analyzing power.

CHAPTER IV

ELECTROMAGNETIC CURRENTS IN χEFT

We now turn our attention to the derivation of the electromagnetic current. According to the power-counting scheme, the LO term results from the coupling of the external photon field to the individual nucleons, and is counted as $e\,Q^{-2}$, where a factor $e\,Q$ is from the γNN vertex, and a factor Q^{-3} follows from the momentum δ-function implicit in the disconnected diagrams, see panel a) of Fig. 20. Higher
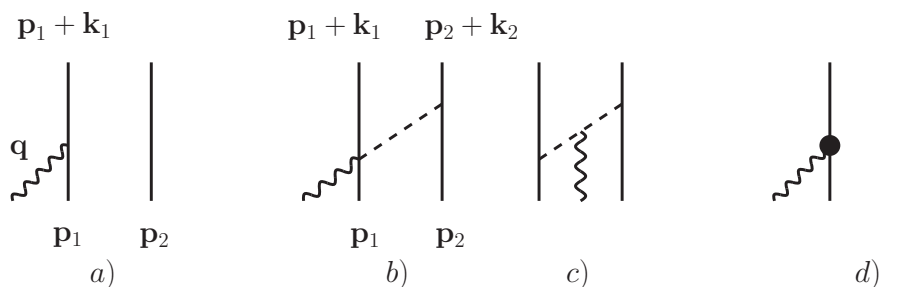
FIG. 20: Currents up to N²LO. Nucleons, pions, and photons are denoted by solid, dashed, and wavy lines, respectively. The filled circle in panel d) represents the $(Q/m_N)^2$ relativistic correction to the LO one-body current illustrated in panel a).

order terms are suppressed by additional powers of Q. In Sec. IV.1 we discuss the contributions occurring up to N²LO, while the contributions entering at N³LO are derived in Sec. IV.2. In Sec. IV.4 we explicitly verify that the present formulation, based on TOPT with the additional prescription introduced to account for recoil corrections to the reducible diagrams, leads to currents which are conserved and hence consistent with the N²LO potential derived in Sec. III.

IV.1   CURRENTS UP TO N²LO

The electromagnetic current up to N²LO is represented in Fig. 20, where we also show the kinematic of the process under study. Specifically, $\mathbf{q}$ denotes the external photon momentum, and the partial momenta are defined as

$$\mathbf{k}_i = \mathbf{p}'_i - \mathbf{p}_i \ , \qquad \mathbf{K}_i = (\mathbf{p}'_i + \mathbf{p}_i)/2 \ , \tag{103}$$

where $\mathbf{p}_i$ and $\mathbf{p}'_i$ are the initial and final momenta of nucleon $i = 1, 2$. In the remainder of this section we will refer to the panels of Fig. 20.

The LO contribution, implied by the electromagnetic interaction Hamiltonian of Eq. (269), is given by the one-body current of panel a)

$$\mathbf{j}_a^{\text{LO}} = \frac{e}{2\,m_N}\left[2\,e_{N,1}\,\mathbf{K}_1 + i\,\mu_{N,1}\,\boldsymbol{\sigma}_1 \times \mathbf{q}\right] + 1 \rightleftharpoons 2 \ , \tag{104}$$

where the photon momentum $\mathbf{q}$ is equal to the partial momentum transfered to nucleon i, $\mathbf{q} = \mathbf{k}_i$, and m_N denotes the nucleon mass. We recall the definitions of e_N and μ_N:

$$e_N = (1 + \tau_z)/2 \ , \qquad \kappa_N = (\kappa_S + \kappa_V \tau_z)/2 \ , \qquad \mu_N = e_N + \kappa_N \ , \tag{105}$$

where κ_S and κ_V are the isoscalar and isovector combinations of the anomalous magnetic moments of the proton and neutron ($\kappa_S = -0.12$ n.m. and $\kappa_V = 3.706$ n.m.).

The contributions at NLO, $e\,Q^{-1}$, are represented by the diagrams in panels b) and c). A straightforward evaluation of these diagrams in the static limit leads to the expressions

$$\mathbf{j}_b^{\text{NLO}} = -i\,e\frac{g_A^2}{F_\pi^2}\,(\boldsymbol{\tau}_1 \times \boldsymbol{\tau}_2)_z\boldsymbol{\sigma}_1\,\frac{\boldsymbol{\sigma}_2 \cdot \mathbf{k}_2}{\omega_{k_2}^2} + 1 \rightleftharpoons 2 \ , \tag{106}$$

$$\mathbf{j}_c^{\text{NLO}} = i\,e\frac{g_A^2}{F_\pi^2}\,(\boldsymbol{\tau}_1 \times \boldsymbol{\tau}_2)_z\frac{\mathbf{k}_1 - \mathbf{k}_2}{\omega_{k_1}^2\,\omega_{k_2}^2}\boldsymbol{\sigma}_1 \cdot \mathbf{k}_1\,\boldsymbol{\sigma}_2 \cdot \mathbf{k}_2 \ , \tag{107}$$

where, as usual, a δ-function representing the overall momentum conservation has been dropped. The latter follows from the momentum conservation at each of the vertex in the diagram. In particular, the momenta transferred to nucleons 1 and 2 add up to $\mathbf{q}$, $\mathbf{k}_1 + \mathbf{k}_2 = \mathbf{q}$. Note that the expressions given above are the seagull and pion-in-flight currents commonly used in the literature.

The N^{2}LO current is represented by the one-body contribution shown in panel d), and is due to $(Q/m_N)^2$ relativistic corrections to the one-body current in Eq. (104). These are easily derived from a non-relativistic expansion of Eq. (271)

$$\mathbf{j}_d^{\text{N}^2\text{LO}} = -\frac{e}{8\,m_N^3}e_{N,1}\left[2\,\left(K_1^2 + q^2/4\right)(2\,\mathbf{K}_1 + i\,\boldsymbol{\sigma}_1 \times \mathbf{q}) + \mathbf{K}_1 \cdot \mathbf{q}\,(\mathbf{q} + 2i\,\boldsymbol{\sigma}_1 \times \mathbf{K}_1)\right]$$

$$- \frac{i\,e}{8\,m_N^3}\kappa_{N,1}\left[\mathbf{K}_1 \cdot \mathbf{q}\,(4\,\boldsymbol{\sigma}_1 \times \mathbf{K}_1 - i\,\mathbf{q}) - (2\,i\,\mathbf{K}_1 - \boldsymbol{\sigma}_1 \times \mathbf{q})\,q^2/2\right.$$

$$\left. + 2\,(\mathbf{K}_1 \times \mathbf{q})\,\boldsymbol{\sigma}_1 \cdot \mathbf{K}_1\right] + 1 \rightleftharpoons 2 \ . \tag{108}$$
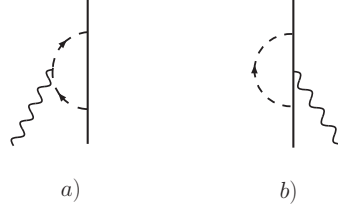
FIG. 21: NLO and N²LO corrections to the one-body current. Notation is as in Fig. 20.

At NLO, and N²LO, there are additional contributions coming from one-loop corrections to the one-body current, see Fig. 21. Diagrams of this kind give rise to contributions to the radius and anomalous magnetic moments of the nucleons. We assume them to be absorbed in the experimental values for these quantities, utilized to construct the LO one-body current operator.

IV.1.1 Recoil Corrections: Cancellations at N²LO

Recoil corrections play an important role also in the evaluation of the current operator. In particular, we observe that recoil corrected reducible contributions at N²LO (N³LO) exactly (partially) cancel irreducible terms at the same order. In the present formulation based on TOPT, there is in principle the additional N²LO current arising from the evaluation of the time-ordered diagrams represented in Fig. 22. Diagrams in panel a) and b) are irreducible and give the following contribution

$$
\mathbf{j}_{\text{irr}}^{\text{N}^2\text{LO}} = \frac{V_{\gamma NN}(1,\mathbf{q})V_{\pi NN}(2,\mathbf{k})V_{\pi NN}(1,\mathbf{k})}{\omega_k^2} + \text{h.c.} = -\mathbf{j}_{\text{a}}^{\text{LO}}\,\frac{v^\pi(\mathbf{k})}{2\,\omega_k} + \text{h.c.} \ , \qquad (109)
$$

where $V_{\gamma NN}(i,\mathbf{q})$ denotes the vertex from the one-body—or LO—electromagnetic interaction Hamiltonian relative to nucleon i, and a photon with momentum $\mathbf{q}$, $\mathbf{j}_{\text{a}}^{\text{LO}}$ is the current operator defined in Eq. (104), and $v^\pi(\mathbf{k})$ is the static OPEP of Eq (39). Evaluation of the reducible diagrams of panel c) and d) leads to the following contribution

$$
\mathbf{j}_{\text{red}}^{\text{N}^2\text{LO}} = \frac{V_{\gamma NN}(1,\mathbf{q})\,V_{\pi NN}(1,\mathbf{k})\,V_{\pi NN}(2,\mathbf{k})}{E_i-\widetilde{E_1}-E_2'-\omega_q+i\eta}\left[\frac{1}{E_i-\widetilde{E_1}-E_2-\omega_q-\omega_k+i\eta}\right.
$$
$$
\left.+\frac{1}{E_i-E_1-E_2'-\omega_q-\omega_k+i\eta}\right] , \qquad (110)
$$
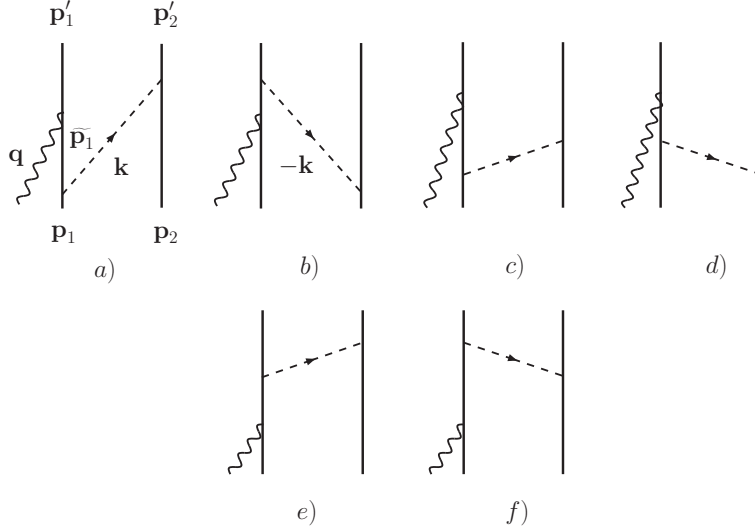
FIG. 22: Time-ordered diagrams illustrating the cancellation of the irreducible con-
tributions a) and b) by the recoil corrections to the LO diagrams c)-f). Notation is
as in Fig. 20.

and the labeling of momenta is as illustrated in the figure. The initial and final
energies of the system E_i and E_f $(E_i = E_f)$ are $E_i = E_1 + E_2 + \omega_q$ and $E_f = E_1' + E_2'$,
where ω_q is the energy of the external photon. The energy of the intermediate
nucleon is denoted with $\widetilde{E_1}$. These energies, including the photon energy in the
initial state, are all suppressed by Q/M relative to $\omega_k \sim Q$, therefore we can expand
the denominators in square brackets as we did for the energy denominators entering
reducible box diagrams—see Eq. (52)

$$\left[\cdots \right] \simeq -\frac{2}{\omega_k} - \frac{E_i - \widetilde{E_1} - E_2' - \omega_q}{\omega_k^2} \, , \tag{111}$$

so that the reducible contribution of diagrams c)+d) now reads

$$\mathbf{j}_{\mathrm{red}}^{\mathrm{N^2LO}} = V_{\gamma NN}(1, \mathbf{k}) \frac{1}{E_i - \widetilde{E_1} - E_2' - \omega_q + i\,\eta} v^\pi(\mathbf{k}) - \frac{V_{\gamma NN}(1, \mathbf{k}) V_{\pi NN}(1, \mathbf{k}) V_{\pi NN}(2, \mathbf{k})}{\omega_k^2}$$

$$= \mathbf{j}_{\mathrm{a}}^{\mathrm{LO}} \frac{1}{E_i - \widetilde{E_1} - E_2' - \omega_q + i\,\eta} v^\pi(\mathbf{k}) + \mathbf{j}_{\mathrm{a}}^{\mathrm{LO}} \frac{v^\pi(\mathbf{k})}{2\,\omega_k} \, . \tag{112}$$

The first term in the equation above is accounted for when the LO one-body current
operator is evaluated in between wave functions solutions of the Lippman-Schwinger
equation with a static OPEP (see discussion below), while the second term represents

the recoil corrected reducible contribution defined as

$$\mathbf{j}_{\mathrm{rec}}^{\mathrm{N^2LO}} = \mathbf{j}_{\mathrm{a}}^{\mathrm{LO}} \frac{v^\pi(\mathbf{k})}{2\,\omega_k} + \mathrm{h.c.} \,, \tag{113}$$

where the h.c. term represents the contribution arising from the reducible diagrams of panels e) and f) of Fig. 22. The complete current at N^{2}LO, obtained by summing the irreducible contribution of Eq. (109) to the expression above, is then seen to vanish.

To interpret the first term of Eq. (112), consider the matrix element of the current operator $\mathbf{j}$ between initial and final two-nucleon states

$$\mathrm{m.e.} = \langle \psi_f \,|\, \mathbf{j} \,|\, \psi_i \rangle \,, \tag{114}$$

where $|\,\psi\rangle$ satisfies the Lippmann-Schwinger equation,

$$\begin{aligned}
|\,\psi\rangle &= |\,\phi\rangle + \frac{1}{E - H_0 + i\,\eta}(v^\pi + \delta v^\pi)\,|\,\psi\rangle \\
&= |\,\phi\rangle + \frac{1}{E - H_0 + i\,\eta}(v^\pi + \delta v^\pi)\,|\,\phi\rangle + \dots \,, \tag{115}
\end{aligned}$$

and $|\,\phi\rangle$ is the unperturbed wave function solution of $H_0\,|\,\phi\rangle = E\,|\,\phi\rangle$. The δv^π term represents the recoil correction to the static OPEP, which can be easily obtained by expanding the energy denominators entering the OPE transition amplitude in the usual way and is given by

$$\delta v^\pi = -\frac{(E_i - H_0)}{\omega_k^2} V_{\pi NN}(2, \mathbf{k}) V_{\pi NN}(1, \mathbf{k}) + \mathrm{h.c.} = (E_i - H_0)\frac{v^\pi}{2\,\omega_k} + \mathrm{h.c.} \,. \tag{116}$$

Insertion of the perturbed wave functions into the matrix element of Eq. (114), leads to (for a single iteration)

$$\begin{aligned}
\langle \psi_f \,|\, \mathbf{j} \,|\, \psi_i \rangle &= \langle \phi_f \,|\, \mathbf{j} \,|\, \phi_i \rangle + \langle \phi_f \,|\, \mathbf{j} \frac{1}{E_i - H_0 - i\,\eta} v^\pi + \mathrm{h.c.} \,|\, \phi_i \rangle \\
&+ \langle \phi_f \,|\, \mathbf{j} \frac{v^\pi}{2\,\omega_k} + \mathrm{h.c.} \,|\, \phi_i \rangle \,, \tag{117}
\end{aligned}$$

where we keep terms linear in v^π and δv^π. Let us consider just the LO one-body current and the N^{2}LO irreducible current of Eq. (109), that is

$$\mathbf{j} = \mathbf{j}_{\mathrm{a}}^{\mathrm{LO}} + \mathbf{j}_{\mathrm{irr}}^{\mathrm{N^2LO}} \,, \tag{118}$$

then the matrix element of this current operator is

$$\begin{aligned}
\langle \psi_f \,|\, \mathbf{j} \,|\, \psi_i \rangle &= \langle \phi_f \,|\, \mathbf{j}_{\mathrm{a}}^{\mathrm{LO}} \,|\, \phi_i \rangle + \langle \phi_f \,|\, \mathbf{j}_{\mathrm{irr}}^{\mathrm{N^2LO}} \,|\, \phi_i \rangle \\
&+ \langle \phi_f \,|\, \mathbf{j}_{\mathrm{a}}^{\mathrm{LO}} \frac{1}{E_i - H_0 - i\,\eta} v^\pi + \mathrm{h.c.} \,|\, \phi_i \rangle \\
&+ \langle \phi_f \,|\, \mathbf{j}_{\mathrm{a}}^{\mathrm{LO}} \frac{v^\pi}{2\,\omega_k} + \mathrm{h.c.} \,|\, \phi_i \rangle \,, \tag{119}
\end{aligned}$$

where terms up to N²LO are shown. In the previous equation, terms linear in v^π reproduce the first term on the r.h.s. of Eq. (112) and the analogous one coming from diagrams e) and f) of Fig. 22. These contributions are already accounted for when the matrix element is evaluated between wave functions solution of the Lippman-Schwinger equation with a static OPEP. The last two terms, which come from the recoil correction to the static OPEP, exactly cancel the second term which arises from the two-body current contribution represented in Fig. 22 panels a) and d). Thus, if OPEP is taken in the static limit, as is the case for the calculations reported in Sec. VI, then the contributions of diagrams a) and d) should not be retained, since they are canceled by recoil corrections to OPEP. The discussion above shows that, when one uses the static OPEP to generate the nuclear wave functions, then the current operator derived by retaining both recoil corrected reducible and irreducible contributions at each order, provides a better approximation than the corresponding operator derived by retaining only irreducible terms.

So far, we have implicitly assumed that the intermediate states are eigenstates of the free interaction Hamiltonian H_0. In fact, the situation becomes more delicate when the intermediate states describe fully interacting, rather than free, particles. Let now $|\varphi\rangle$ denote a bound or continuum state corresponding to $H_0 + v^\pi$ with energy E, and let δv^π be the recoil correction to the static OPEP. To first order in δv^π, the perturbed state $|\psi\rangle$ is

$$|\psi\rangle = |\varphi\rangle + \frac{1}{E - H_0 - v^\pi}\delta v^\pi |\varphi\rangle , \qquad (120)$$

and the matrix element of the current operator $\mathbf{j} = \mathbf{j}_{\mathrm{a}}^{\mathrm{LO}} + \mathbf{j}_{\mathrm{irr}}^{\mathrm{N2LO}}$ between initial and final states $|\psi_i\rangle$ and $|\psi_f\rangle$ can be expressed as

$$\langle\psi_f | \mathbf{j} | \psi_i\rangle \;=\; \langle\varphi_f | \mathbf{j} | \varphi_i\rangle + \langle\varphi_f | \mathbf{j}\frac{1}{E_i - H_0 - v^\pi}\delta v^\pi + \mathrm{h.c.} | \varphi_i\rangle , \quad (121)$$

where we have dropped terms of order N³LO and higher. We showed that, when the nucleonic intermediate states are free particles, the recoil correction to the static OPE potential is given by the expression reported in Eq. (116). If we assume that the nucleonic intermediate states describe fully interacting particles, *i.e.* they are eigenstates of $H_0 + v^\pi$, then it is plausible that the correction δv^π should be expressed as

$$\delta v^\pi = (E_i - H_0 - v^\pi)\frac{v^\pi}{2\,\omega} + \mathrm{h.c.} , \qquad (122)$$

from which it follows that

$$
\begin{aligned}
\langle \psi_f \mid \mathbf{j} \mid \psi_i \rangle \;=\;& \langle \phi_f \mid \mathbf{j}_{\mathrm{a}}^{\mathrm{LO}} \mid \phi_i \rangle \; + \langle \phi_f \mid \mathbf{j}_{\mathrm{irr}}^{\mathrm{N^2LO}} \mid \phi_i \rangle \\
+\;& \langle \phi_f \mid \mathbf{j}_{\mathrm{a}}^{\mathrm{LO}} \frac{1}{E_i - H_0 - v^\pi + i\,\eta} v^\pi + \mathrm{h.c.} \mid \phi_i \rangle \\
+\;& \langle \phi_f \mid \mathbf{j}_{\mathrm{a}}^{\mathrm{LO}} \frac{v^\pi}{2\,\omega_k} + \mathrm{h.c.} \mid \phi_i \rangle \;,
\end{aligned}
\tag{123}
$$

and cancelations identical to those observed in Eq. (119) occur.

IV.2   CURRENTS AT N³LO

At N³LO ($e\,Q$), we distinguish among five classes of contributions: i) currents generated by minimal substitution in the four-nucleon contact interactions involving two gradients of the nucleons' fields, as well as by non-minimal couplings—panel a) of Fig. 23; ii) tree-level non-minimal currents—panel b) of Fig. 23; iii) TPE currents at one loop—Fig. 25; iv) one-loop corrections to tree-level currents—Figs. 28 and 29; and v) $(Q/m_N)^2$ relativistic corrections to the NLO currents resulting from the non-relativistic reduction of the vertices. The latter are neglected in the present work.

IV.2.1   Currents from Four-Nucleon Contact Interactions

Contact currents at N³LO are represented in panel a) of Fig. 23. The minimal current implied by the electromagnetic interactions of Eqs. (260)–(268) is easily obtained by summing the corresponding vertices listed in Appendix B.3. Specifically, we find

$$
\begin{aligned}
\mathbf{j}_{\mathrm{CT}\gamma}^{\mathrm{N^3LO}} \;=\;& -e\,e_1 \Big[2\,(2\,C_1' - C_2')\,\mathbf{K}_2 + 4\,C_3'\,\mathbf{K}_1 + i\,C_4'\,(\boldsymbol{\sigma}_1 + \boldsymbol{\sigma}_2) \times \mathbf{k}_2 + i\,C_5'\,\boldsymbol{\sigma}_1 \times \mathbf{k}_1 \\
-\;& i\,C_6'\,\boldsymbol{\sigma}_2 \times \mathbf{k}_1 + 2\,(2\,C_7' - C_{10}')\,(\mathbf{K}_2 \cdot \boldsymbol{\sigma}_2)\,\boldsymbol{\sigma}_1 + 2\,(2\,C_8' - C_{11}')\,(\mathbf{K}_2 \cdot \boldsymbol{\sigma}_1)\,\boldsymbol{\sigma}_2 \\
-\;& 2\,C_{13}'\,[(\mathbf{K}_1 \cdot \boldsymbol{\sigma}_1)\,\boldsymbol{\sigma}_2 + (\mathbf{K}_1 \cdot \boldsymbol{\sigma}_2)\,\boldsymbol{\sigma}_1] + 2\,(2\,C_9' - C_{12}')\,\mathbf{K}_2\,(\boldsymbol{\sigma}_1 \cdot \boldsymbol{\sigma}_2) \\
-\;& 4\,C_{14}'\,\mathbf{K}_1\,(\boldsymbol{\sigma}_1 \cdot \boldsymbol{\sigma}_2) \Big] + 1 \rightleftharpoons 2 \;,
\end{aligned}
\tag{124}
$$

where the momenta are defined as in Eq. (103).

Similarly, the non-minimal contact current implied by the Hamiltonian of Eq. (273) is obtained by the corresponding vertex—Eq. (306)—and reads

$$
\mathbf{j}_{\mathrm{CT}\gamma,\mathrm{nm}}^{\mathrm{N^3LO}} = -i\,e \Big[C_{15}'\,\boldsymbol{\sigma}_1 + C_{16}'\,(\tau_{1,z} - \tau_{2,z})\,\boldsymbol{\sigma}_1 \Big] \times \mathbf{q} + 1 \rightleftharpoons 2 \;.
\tag{125}
$$
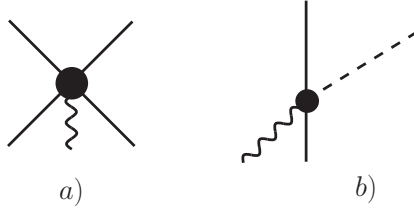
FIG. 23: Diagrams illustrating the N³LO contact currents, both of minimal and non-minimal nature, panel a), and the N³LO tree-level current involving the nuclear-electromagnetic Hamiltonian of Eq. (272) at the vertex illustrated by a full circle in panel b). Notation is as in Fig. 20. Only one of the possible time-ordered diagrams is represented in panel b) for the tree-level current.

IV.2.2 Tree-Level Non-Minimal Current at N³LO

At N³LO there is a contribution involving the standard πNN vertex on one nucleon, and a $\gamma\pi NN$ vertex of order $e\,Q^2$ on the other nucleon, derived from the interaction Hamiltonian of Eq. (272). This tree-level current is represented in panel b) of Fig. 23, and a direct evaluation of the corresponding amplitude leads to

$$\mathbf{j}_{\text{tree}}^{\text{N}^3\text{LO}} = i\,e\,\frac{g_A}{F_\pi^2}\left[(d_8'\,\tau_{2,z} + d_9'\,\boldsymbol{\tau}_1\cdot\boldsymbol{\tau}_2)\,\mathbf{k}_2 - d_{21}'(\boldsymbol{\tau}_1\times\boldsymbol{\tau}_2)_z\boldsymbol{\sigma}_1\times\mathbf{k}_2\right]\times\mathbf{q}\,\frac{\boldsymbol{\sigma}_2\cdot\mathbf{k}_2}{\omega_{k_2}^2} + 1\rightleftharpoons 2\ . \tag{126}$$

Higher order Hamiltonians derived from the χEFT Lagrangians in the pion and nu-
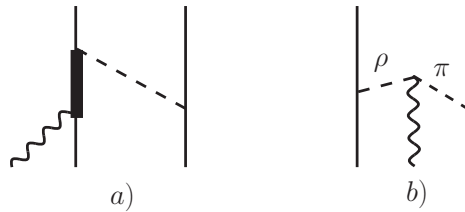
FIG. 24: Diagrams illustrating the pion exchange current involving the excitation of virtual Δ-resonance, panel a), and the $\gamma\rho\pi$ exchange current. Notation as in Fig. 20, but for the thick line representing the Δ-isobar in panel a), and for the dashed lines representing ρ and π mesons as indicated in panel b).

cleon sector, such as the $e\,Q^2$ interaction of Eq. (272), subsume interactions involving heavy-mesons or nucleon resonances integrated out from the theory. This feature,

referred to as the 'saturation mechanism', is typical of the χEFT formulation. Indeed, χEFT Lagrangians describe the dynamics of the system in terms of a given set of degrees of freedom, and contributions arising from additional and heavier degrees of freedom are implicitly incorporated in the theory. Higher order interactions, described in our case in terms of pions and nucleons, include subleading pion and nucleon interactions. For example, the isovector part of $\mathbf{j}_{\text{tree}}^{\text{N3LO}}$ has the same structure as the current involving N-Δ excitation [42] as illustrated in panel a) of Fig. 24. This current is obtained by direct evaluation of the amplitude which now involves $\pi N\Delta$ and $\gamma\pi N\Delta$ couplings implied by the corresponding χEFT Lagrangians, and in the static limit is given by [42]

$$\mathbf{j}_\Delta = i\,\frac{e\,\mu^*}{9\,m_N}\frac{g_A\,h_A}{\Delta\,F_\pi^2}\frac{\boldsymbol{\sigma}_2\cdot\mathbf{k}_2}{k_2^2+m_\pi^2}\Big[4\,\tau_{2,z}\,\mathbf{k}_2-(\boldsymbol{\tau}_1\times\boldsymbol{\tau}_2)_z\,\boldsymbol{\sigma}_1\times\mathbf{k}_2\Big]\times\mathbf{q}+1\rightleftharpoons2,\quad(127)$$

where Δ is the Δ-N mass difference, $\Delta = m_\Delta - m_N$, h_A is the $\pi N\Delta$ coupling constant, and μ^* is the $N\Delta$-transition magnetic moment. The isovector part of $\mathbf{j}_{\text{tree}}^{\text{N3LO}}$ then reduces to the $\mathbf{j}_\Delta$ given above, if the following identifications are made: $d_{21}'/d_8' = 1/4$, and $d_8' = 4\,\mu^* h_A/(9\,m_N\,\Delta)$. Similarly, the isoscalar part of $\mathbf{j}_{\text{tree}}^{\text{N3LO}}$ simulates the $\rho\pi\gamma$ current (see [10] and references therein), illustrated in panel b) of Fig. 24 and given by the following expression

$$\mathbf{j}_{\rho\pi\gamma} = i\,e\frac{g_A g_{\rho\pi\gamma} g_{\rho NN}}{F_\pi m_\rho^3}\,\boldsymbol{\tau}_1\cdot\boldsymbol{\tau}_2\,\mathbf{k}_2\times\mathbf{q}\,\frac{\boldsymbol{\sigma}_2\cdot\mathbf{k}_2}{\omega_{k_2}^2\,\omega_{k_1,\rho}^2}+1\rightleftharpoons2\;,\qquad(128)$$

where $\omega_{k_1,\rho}^2 = \sqrt{m_\rho^2 + k_1^2}$, is the ρ-meson propagator with m_ρ indicating the ρ-meson mass, $g_{\rho\pi\gamma}$ is the $\rho\pi\gamma$ transition coupling constant, and $g_{\rho NN}$ is the ρNN coupling constant (its vector coupling). If one ignores the ρ-meson propagation, then the isoscalar part of $\mathbf{j}_{\text{tree}}^{\text{N3LO}}$ reduces to the expression above, if $d_9' = g_{\rho\pi\gamma} g_{\rho NN} F_\pi/m_\rho^3$. The 'resonance saturation' argument is commonly exploited to fix LECs entering the theory. Indeed, we will utilize the constraint $d_{21}'/d_8' = 1/4$ implied by the Δ-resonance saturation mechanism. But otherwise we will determine the remaining LECs so as to reproduce nuclear electromagnetic observables—see Sec. VI.

IV.2.3   One-Loop Two-Body Currents

One-loop two-body currents are illustrated by the diagrams in Fig. 25, where we indicate the nucleons' momenta, as well as those of the exchanged pions $\mathbf{q}_i$, with i as indicated in the figure. The expressions for these currents follow from a direct

evaluation of the transition amplitudes associated with these diagrams. Recoil corrections to the reducible contributions are properly accounted for in the currents of type d), e), and g). This aspect of the calculation is discussed in more detail in the next section.

FIG. 25: Diagrams illustrating one-loop two-body currents. Only one among the possible time orderings is shown. Notation is as in Fig. 20.

In what follows, we refer to the panels of Fig. 25. We also introduce the notation

$$\int \equiv \int \frac{d\mathbf{q}_i}{(2\pi)^2} \,, \qquad \omega_i = \sqrt{q_i^2 + m_\pi^2} \,, \qquad (129)$$

where the integration is over one of the exchanged pions, while the remaining internal momenta $\mathbf{q}_j$, with $j \neq i$ are fixed by the momentum-conserving $\bar{\delta}$-functions at each vertex. Referring to Fig. 25, we find

$$\mathbf{j}_a^{\mathrm{N^3LO}} = -2\,i\frac{e\,g_A^2}{F_\pi^4} \int \frac{2\,\tau_{2,z}\,(\boldsymbol{\sigma}_1 \times \mathbf{q}_2) + (\boldsymbol{\tau}_1 \times \boldsymbol{\tau}_2)_z\,\mathbf{q}_2}{\omega_1\,\omega_2(\omega_1 + \omega_2)} + 1 \rightleftharpoons 2 \,, \qquad (130)$$

where, for example, the integral is over $\mathbf{q}_1$, and the internal momentum $\mathbf{q}_2 = \mathbf{k}_2 - \mathbf{q}_1$.

Type b) diagrams give

$$\begin{aligned}
\mathbf{j}_b^{\mathrm{N^3LO}} &= 2\,i\frac{e\,g_A^2}{F_\pi^4} \int \frac{\mathbf{q}_1 - \mathbf{q}_3}{\omega_1\,\omega_2\,\omega_3}\frac{\omega_1 + \omega_2 + \omega_3}{(\omega_1 + \omega_2)(\omega_1 + \omega_3)(\omega_2 + \omega_3)}\Big[(\boldsymbol{\tau}_1 \times \boldsymbol{\tau}_2)_z\,\mathbf{q}_1 \cdot \mathbf{q}_2 \\
&\quad - 2\,\tau_{2,z}\,\boldsymbol{\sigma}_1 \cdot (\mathbf{q}_1 \times \mathbf{q}_2)\Big] + 1 \rightleftharpoons 2 \,. \qquad (131)
\end{aligned}$$

Next, the contributions of type c)-e) diagrams are:

$$
\mathbf{j}_{\mathrm{c}}^{\mathrm{N^3LO}} = -i\frac{e}{2\,F_\pi^4}\,(\boldsymbol{\tau}_1 \times \boldsymbol{\tau}_2)_z \int \frac{\mathbf{q}_1 - \mathbf{q}_3}{\omega_1\,\omega_3}\frac{\omega_2(\omega_1 + \omega_2 + \omega_3) - 3\,\omega_1\,\omega_3}{(\omega_1 + \omega_2)(\omega_1 + \omega_3)(\omega_2 + \omega_3)} \ , \quad (132)
$$

$$
\mathbf{j}_{\mathrm{d}}^{\mathrm{N^3LO}} = -2\,i\frac{e\,g_A^4}{F_\pi^4} \int \frac{\omega_1^2 + \omega_2^2 + \omega_1\omega_2}{\omega_1^3\,\omega_2^3\,(\omega_1 + \omega_2)} \left[(\boldsymbol{\tau}_1 \times \boldsymbol{\tau}_2)_z\,\mathbf{q}_2\,(\mathbf{q}_1 \cdot \mathbf{q}_2) \right.
$$
$$
+ \ 2\,\tau_{2,z}\,\mathbf{q}_1 \cdot \mathbf{q}_2\,(\boldsymbol{\sigma}_1 \times \mathbf{q}_2) + 2\,\tau_{1,z}\,\mathbf{q}_2\,\boldsymbol{\sigma}_2 \cdot (\mathbf{q}_1 \times \mathbf{q}_2) \bigg] + 1 \rightleftharpoons 2 \ , \quad (133)
$$

$$
\mathbf{j}_{\mathrm{e}}^{\mathrm{N^3LO}} = 2\,i\frac{e\,g_A^4}{F_\pi^4} \int (\mathbf{q}_1 - \mathbf{q}_3)f(\omega_1,\omega_2,\omega_3) \left[(\boldsymbol{\tau}_1 \times \boldsymbol{\tau}_2)_z\,(\mathbf{q}_1 \cdot \mathbf{q}_2)(\mathbf{q}_2 \cdot \mathbf{q}_3) \right.
$$
$$
+ \ 2\,\tau_{2,z}\,(\mathbf{q}_2 \cdot \mathbf{q}_3)\,\boldsymbol{\sigma}_1 \cdot (\mathbf{q}_2 \times \mathbf{q}_1) + 2\,\tau_{1,z}\,(\mathbf{q}_1 \cdot \mathbf{q}_2)\,\boldsymbol{\sigma}_2 \cdot (\mathbf{q}_3 \times \mathbf{q}_2) \bigg] \ , \quad (134)
$$

where the function $f(\omega_1, \omega_2, \omega_3)$ containing the pion energy factors from field normalizations and energy denominators for diagrams of type e) is defined as

$$
f(\omega_1, \omega_2, \omega_3) = \frac{1}{\omega_1\,\omega_2\,\omega_3(\omega_1 + \omega_2)(\omega_1 + \omega_3)(\omega_2 + \omega_3)} \left[\frac{\omega_1\,\omega_2 + \omega_2\,\omega_3 + \omega_1\,\omega_3}{\omega_1\,\omega_2\,\omega_3} \right.
$$
$$
+ \ \frac{(\omega_1 + \omega_2)\,(\omega_2 + \omega_3)\,(\omega_1^2 + \omega_3^2)}{\omega_1^2\,\omega_2\,\omega_3^2} + \frac{\omega_2}{\omega_1\,\omega_3} + \frac{\omega_1 + \omega_2 + \omega_3}{\omega_2^2} \bigg] \ . \quad (135)
$$

Lastly, diagrams of type f) and h) vanish, since the integrand (in the static limit) is an odd function of the loop momentum $\mathbf{q}_1$,

$$
\mathbf{j}_{\mathrm{f}}^{\mathrm{N^3LO}} \text{ and } \mathbf{j}_{\mathrm{h}}^{\mathrm{N^3LO}} \propto \int \frac{\mathbf{q}_1}{\omega_1^3} \times (\text{spin–isospin structure}) \ . \quad (136)
$$

However, the contributions of type g) and i) diagrams read:

$$
\mathbf{j}_{\mathrm{g}}^{\mathrm{N^3LO}} = 2\,i\frac{e\,g_A^2\,C_T}{F_\pi^2}\,(\boldsymbol{\tau}_1 \times \boldsymbol{\tau}_2)_z \int \frac{\mathbf{q}_1 - \mathbf{q}_2}{\omega_1^3\,\omega_2^3}\frac{\omega_1^2 + \omega_1\,\omega_2 + \omega_2^2}{\omega_1 + \omega_2}(\boldsymbol{\sigma}_1 \cdot \mathbf{q}_2)(\boldsymbol{\sigma}_2 \cdot \mathbf{q}_1), (137)
$$

$$
\mathbf{j}_{\mathrm{i}}^{\mathrm{N^3LO}} = i\frac{e\,g_A^2}{F_\pi^2}\tau_{1,z} \int \frac{\mathbf{q}_1 - \mathbf{q}_2}{\omega_1^3\,\omega_2^3}\frac{\omega_1^2 + \omega_1\,\omega_2 + \omega_2^2}{\omega_1 + \omega_2} \left[C_S\,\boldsymbol{\sigma}_1 \cdot (\mathbf{q}_1 \times \mathbf{q}_2) \right.
$$
$$
- \ C_T\,\boldsymbol{\sigma}_2 \cdot (\mathbf{q}_1 \times \mathbf{q}_2) \bigg] + 1 \rightleftharpoons 2 \ . \quad (138)
$$

We observe that, the one-loop two-body currents have only isovector components. The TPE currents of panels a)–e), are expressed in terms of known LECs, *i.e.* the axial coupling constant g_A, and the pion decay amplitude F_π. Thus these currents are already fixed by the experimental data, while the remaining one-loop currents involve the LECs C_S and C_T from the contact interaction vertex.

In closing, we note that diagrams of the type shown in Fig. 26 are suppressed by an extra power of Q relative to those considered in this section, *i.e.* they are of order
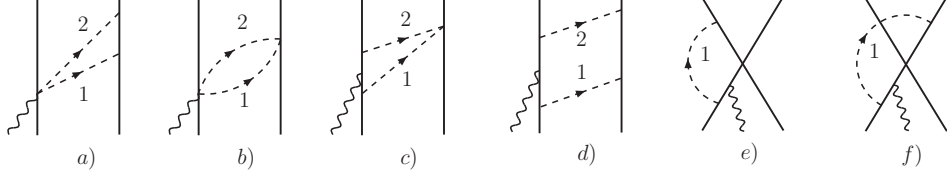
FIG. 26: Diagrams illustrating N^{4}LO contributions not included in the present work. Only one among the possible time orderings is shown. Notation is as in Fig. 20.

$e\,Q^2$. For example, the diagrams of type a) give rise to the following current operator

$$\text{type a) in Fig.}\,26 = \frac{e}{m}\frac{g_A^2}{F_\pi^4}\tau_{z,1}(2\,\mathbf{K}_1 + i\boldsymbol{\sigma}_1 \times \mathbf{k}_1)\int \frac{\mathbf{q}_1 \cdot \mathbf{q}_2}{\omega_1^2\,\omega_2^2} + 1 \rightleftharpoons 2\ , \qquad (139)$$

where the momentum $\mathbf{K}_i$ is as given in Eq. (103), while those of type b) vanish, since they are proportional $(\delta_{az}\,\tau_{1,b} + \delta_{bz}\,\tau_{1,a} - 2\,\delta_{ab}\,\tau_{1,z})\,\epsilon_{abc}\,\tau_{2,c} = (\epsilon_{zbc} + \epsilon_{bzc})\,\tau_{1,b}\,\tau_{2,c}$. Therefore, the one-loop two-body current at N^{3}LO is given by the sum of the currents of type a)–e), g), and i)

$$\mathbf{j}_{\text{loop}}^{\text{N}^3\text{LO}} = \mathbf{j}_{\text{a}}^{\text{N}^3\text{LO}} + \mathbf{j}_{\text{b}}^{\text{N}^3\text{LO}} + \mathbf{j}_{\text{c}}^{\text{N}^3\text{LO}} + \mathbf{j}_{\text{d}}^{\text{N}^3\text{LO}} + \mathbf{j}_{\text{e}}^{\text{N}^3\text{LO}} + \mathbf{j}_{\text{g}}^{\text{N}^3\text{LO}} + \mathbf{j}_{\text{i}}^{\text{N}^3\text{LO}}\ , \qquad (140)$$

where the individual currents are given in Eq. (130)–(134), (137), and (138).

Recoil Corrections: Cancellations at N^{3}LO

The evaluation of the current operators resulting from the diagrams of Fig. 25, panels d)-e) and g), is carried out by including the recoil corrections of order Q to the reducible diagrams shown in Fig. 27 panels a)-c). Again, we do not consider recoil corrections arising from pions emitted and reabsorbed by the same nucleon, therefore the current $\mathbf{j}_{\text{i}}^{\text{N}^3\text{LO}}$, illustrated in panel i) of Fig. 25, is obtained by retaining irreducible terms only. Cancellations between reducible and recoil corrected reducible contributions are also observed at N^{3}LO. As an example, we consider the irreducible and reducible diagrams represented in Fig. 25 d) and Fig. 27 a), respectively. We follow the procedure adopted in Sec. IV.1.1, and expand, in the reducible diagrams, the energies of the intermediate nucleonic states, which are suppressed by a factor Q/M with respect to the pionic energies $\omega_i \sim Q$. Up to order $e\,Q$, the current operator
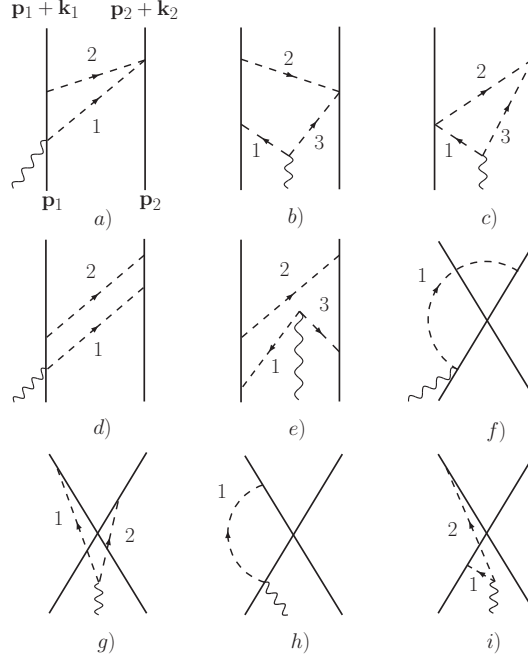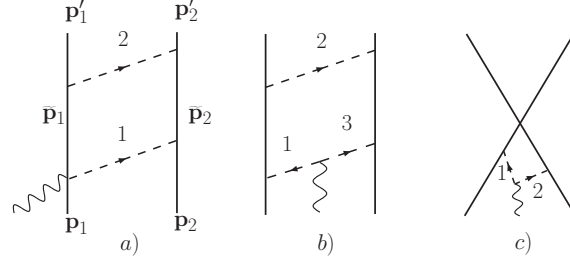
FIG. 27: Diagrams illustrating the reducible one-loop two-body currents. Only one among the possible time orderings is shown. Notation is as in Fig. 20.

$\mathbf{j}_{d,\,red}^{N^3LO}$ associated with the reducible 'box' diagrams then reads

$$\mathbf{j}_{d,\,red}^{N^3LO} = \int v^\pi(\mathbf{q}_2) \frac{1}{E_i - \widetilde{E}_1 - \widetilde{E}_2 + i\eta} \mathbf{j}_b^{NLO}(\mathbf{q}_1)$$
$$- \int 2\frac{\omega_1 + \omega_2}{\omega_1\,\omega_2} V_{\pi NN}(2, \mathbf{q}_2)\, V_{\pi NN}(2, \mathbf{q}_1)\, V_{\pi NN}(1, \mathbf{q}_2)\, V_{\gamma\pi NN}(1, \mathbf{q}_1)\ ,(141)$$

where $v^\pi(\mathbf{q}_2)$ and $\mathbf{j}_b^{NLO}(\mathbf{q}_1)$ are the OPEP and pion-seagull current operators in the static limit defined in Eqs. (39) and (106), respectively. As usual, the $V(i, \mathbf{q}_j)$ denotes the vertex from the interaction Hamiltonian relative to nucleon i and a pion with momentum $\mathbf{q}_j$, and E_i is the initial energy of the system, while $\widetilde{E}_1$ and $\widetilde{E}_2$ are the energies of the intermediate nucleons. Also we ignore the first term of Eq. (141), but retain the second term due to recoil corrections, and add it to the irreducible contribution, $\mathbf{j}_{d,irr}^{N^3LO}$, which is given by

$$\mathbf{j}_{d,irr}^{N^3LO} = \int \frac{2}{\omega_1\,\omega_2(\omega_1 + \omega_2)}\, V_{\pi NN}(2, \mathbf{q}_2)\, V_{\pi NN}(2, \mathbf{q}_1)\, V_{\pi NN}(1, \mathbf{q}_1)\, V_{\gamma\pi NN}(1, \mathbf{q}_1)$$
$$+ \int 2\frac{\omega_1^2 + \omega_2^2 + \omega_1\,\omega_2}{\omega_1\,\omega_2(\omega_1 + \omega_2)}\, V_{\pi NN}(2, \mathbf{q}_1)\, V_{\pi NN}(2, \mathbf{q}_2)\, V_{\pi NN}(1, \mathbf{q}_2)\, V_{\gamma\pi NN}(1, \mathbf{q}_1).(142)$$

The first term above comes from the irreducible direct diagrams (in which, with reference to Fig. 25 d), pion 1 is absorbed before pion 2), while the second term is from the crossed diagrams (in which pion 1 is absorbed after pion 2). Equation (142) can be further simplified expressing the product $V_{\pi NN}(2, \mathbf{q}_1)\, V_{\pi NN}(2, \mathbf{q}_2)$ as

$$V_{\pi NN}(2, \mathbf{q}_1)\, V_{\pi NN}(2, \mathbf{q}_2) = [V_{\pi NN}(2, \mathbf{q}_1), V_{\pi NN}(2, \mathbf{q}_2)] + V_{\pi NN}(2, \mathbf{q}_2)\, V_{\pi NN}(2, \mathbf{q}_1)\ ,$$
$$(143)$$

to obtain

$$
\mathbf{j}_{\text{d,irr}}^{\text{N}^3\text{LO}} = \int 2\frac{\omega_1 + \omega_2}{\omega_1\,\omega_2} V_{\pi NN}(2, \mathbf{q}_2)\, V_{\pi NN}(2, \mathbf{q}_1)\, V_{\pi NN}(1, \mathbf{q}_2)\, V_{\gamma\pi NN}(1, \mathbf{q}_1)
$$
$$
+ \int 2\frac{\omega_1^2 + \omega_2^2 + \omega_1\,\omega_2}{\omega_1\,\omega_2(\omega_1 + \omega_2)}
$$
$$
\times\ [V_{\pi NN}(2, \mathbf{q}_1), V_{\pi NN}(2, \mathbf{q}_2)]\, V_{\pi NN}(1, \mathbf{q}_2) V_{\gamma\pi NN}(1, \mathbf{q}_1)\ . \tag{144}
$$

The complete current of type d) is then

$$
\mathbf{j}_{\text{d}}^{\text{N}^3\text{LO}} = \int 2\frac{\omega_1^2 + \omega_2^2 + \omega_1\,\omega_2}{\omega_1\,\omega_2(\omega_1 + \omega_2)}
$$
$$
\times\ [V_{\pi NN}(2, \mathbf{q}_1)\,, V_{\pi NN}(2, \mathbf{q}_2)]\, V_{\pi NN}(1, \mathbf{q}_2) V_{\gamma\pi NN}(1, \mathbf{q}_1)\ -\text{h.c.}\ ,\ \ (145)
$$

where the h.c. term corresponds to including the diagrams in which the photon hooks up to the pion with momentum $\mathbf{q}_2$. Note that the recoil corrections exactly cancel the first term of Eq. (144), leaving the term proportional to the energy factor associated with the crossed diagrams only. We find it interesting that these cancellations are also obtained for the current of type e). The latter is again expressed in terms of a commutator between the vertices involving nucleon 2 multiplied by the energy factor $f(\omega_1, \omega_2, \omega_3)$, defined in Eq. (135), coming from the crossed diagrams

$$
\mathbf{j}_{\text{e}}^{\text{N}^3\text{LO}} = \int 4\, f(\omega_1, \omega_2, \omega_3)\, [V_{\pi NN}(2, \mathbf{q}_3), V_{\pi NN}(2, \mathbf{q}_2)]
$$
$$
\times\ V_{\pi NN}(1, \mathbf{q}_2) V_{\pi NN}(1, \mathbf{q}_1) V_{\gamma\pi\pi}(\mathbf{q}_1, \mathbf{q}_3)\ -\text{h.c.}\ ,\ \ (146)
$$

and it is therefore tempting to conjecture that they persist at higher orders. However, this statement has not been proven.

Renormalization of One-Loop Currents

The kernels entering the one-loop currents derived in Sec. IV.2.3 need to be regularized because of their divergent behavior at high values of the momentum. We follow the dimensional regularization scheme adopted to renormalize the *NN* potential. We consider the currents (involving one and two pions) illustrated in panels a), d), g), and i) of Fig. 25. Those in panels b), c), and e) (involving three pions) are discussed in Sec. V.1. For them we only derive the corresponding magnetic dipole operators. In the expressions for the currents of type a) and d), given in Eqs. (130) and (133), respectively, a $\bar{\delta}(\mathbf{q}_1 + \mathbf{q}_2 - \mathbf{k}_2)$ and an integration over the momenta $\mathbf{q}_1$ and $\mathbf{q}_2$ are implicit. After integrating over one of the momentum, we can rewrite the expressions

of these currents in terms of the kernels defined in Appendix C. In particular we obtain

$$\mathbf{j}_{\mathrm{a}}^{\mathrm{N^3LO}} = -i\,e\,\frac{g_A^2}{F_\pi^4}\,I^{(0)}(k_2)\Big[2\,\tau_{2,z}\,\boldsymbol{\sigma}_1\times\mathbf{k}_2 + (\boldsymbol{\tau}_1\times\boldsymbol{\tau}_2)_z\,\mathbf{k}_2\Big] + 1 \rightleftharpoons 2 \;, \qquad (147)$$

$$\mathbf{j}_{\mathrm{d}}^{\mathrm{N^3LO}} = -i\,e\,\frac{g_A^4}{F_\pi^4}\Bigg[\;\big[k_2^2\,J^{(0)}(k_2) - J^{(2)}(k_2)\big]\,\Big[2\,\tau_{2,z}\,\boldsymbol{\sigma}_1\times\mathbf{k}_2 + (\boldsymbol{\tau}_1\times\boldsymbol{\tau}_2)_z\,\mathbf{k}_2\Big]$$

$$+ \;\; 4\,\tau_{1,z}\,J_{ij}^{(2)}(\mathbf{k}_2)\,(\boldsymbol{\sigma}_2\times\mathbf{k}_2)_j\;\Bigg] + 1 \rightleftharpoons 2 \;. \qquad (148)$$

The Eqs. (137) and (138) relative to currents of type g) and i) contain a $\bar{\delta}(\mathbf{q}_1+\mathbf{q}_2-\mathbf{q})$ and they are rewritten in terms of the kernels as

$$\mathbf{j}_{\mathrm{g}}^{\mathrm{N^3LO}} = -2\,i\,e\frac{g_A^2}{F_\pi^2}\,C_T\,(\boldsymbol{\tau}_1\times\boldsymbol{\tau}_2)_z\,J_{ij}^{(2)}(\mathbf{q})\,\sigma_{1,j}\,\boldsymbol{\sigma}_2\cdot\mathbf{q} + 1 \rightleftharpoons 2 \;, \qquad (149)$$

$$\mathbf{j}_{\mathrm{i}}^{\mathrm{N^3LO}} = -2\,i\,e\frac{g_A^2}{F_\pi^2}\tau_{1,z}\,J_{ij}^{(2)}(\mathbf{q})\,\Big[C_S\,(\boldsymbol{\sigma}_1\times\mathbf{q})_j - C_T\,(\boldsymbol{\sigma}_2\times\mathbf{q})_j\Big] + 1 \rightleftharpoons 2 \;. \quad (150)$$

Insertion of the finite parts of the various kernels in the expressions above gives then

$$\bar{\mathbf{j}}_{\mathrm{a}}^{\mathrm{N^3LO}} = i\,e\,\frac{g_A^2}{8\pi^2 F_\pi^4}\,G(k_2)\Big[2\,\tau_{2,z}\,\boldsymbol{\sigma}_1\times\mathbf{k}_2 + (\boldsymbol{\tau}_1\times\boldsymbol{\tau}_2)_z\,\mathbf{k}_2\Big] + 1 \rightleftharpoons 2 \;, \qquad (151)$$

$$\bar{\mathbf{j}}_{\mathrm{d}}^{\mathrm{N^3LO}} = -i\,e\,\frac{g_A^4}{8\,\pi^2\,F_\pi^4}G(k_2)\Bigg[\left(3 - \frac{4\,m_\pi^2}{4\,m_\pi^2 + k_2^2}\right)\Big[2\,\tau_{2,z}\,\boldsymbol{\sigma}_1\times\mathbf{k}_2 + (\boldsymbol{\tau}_1\times\boldsymbol{\tau}_2)_z\,\mathbf{k}_2\Big]$$

$$- \;\; 4\,\tau_{1,z}\,\boldsymbol{\sigma}_2\times\mathbf{k}_2\Bigg] + 1 \rightleftharpoons 2 \;, \qquad (152)$$

$$\bar{\mathbf{j}}_{\mathrm{g}}^{\mathrm{N^3LO}} = i\,e\frac{g_A^2\,C_T}{4\,\pi^2\,F_\pi^2}(\boldsymbol{\tau}_1\times\boldsymbol{\tau}_2)_z\,G(q)\,\boldsymbol{\sigma}_1\,\boldsymbol{\sigma}_2\cdot\mathbf{q} + 1 \rightleftharpoons 2 \;, \qquad (153)$$

$$\bar{\mathbf{j}}_{\mathrm{i}}^{\mathrm{N^3LO}} = i\,e\,\frac{g_A^2}{4\pi^2\,F_\pi^2}\tau_{1,z}\,G(q)\,(C_S\,\boldsymbol{\sigma}_1\times\mathbf{q} - C_T\,\boldsymbol{\sigma}_2\times\mathbf{q}) + 1 \rightleftharpoons 2 \;, \qquad (154)$$

and the loop function G is defined in Eq. (73). The divergent parts of the kernels lead to renormalization of some of the LECs C_i' entering the N^{3}LO contact current, both of minimal and non-minimal nature, defined in Eqs. (124) and (273). Specifically,

these renormalization constant are given by

$$\mathbf{j}_{\infty,a}^{\text{N}^3\text{LO}} = i\,e\,\frac{g_A^2}{8\pi^2 F_\pi^4}\left(\frac{2}{\epsilon}+\dots\right)\left[-2\,\tau_{2,z}\,\boldsymbol{\sigma}_1\times\mathbf{k}_2-(\boldsymbol{\tau}_1\times\boldsymbol{\tau}_2)_z\,\mathbf{k}_2\right]+1\rightleftharpoons 2\,,\quad(155)$$

$$\mathbf{j}_{\infty,b}^{\text{N}^3\text{LO}} = i\,e\,\frac{g_A^2}{8\pi^2 F_\pi^4}\left(\frac{2}{\epsilon}+\dots\right)\left[2\,\tau_{2,z}\boldsymbol{\sigma}_1\times(\mathbf{k}_2-\mathbf{q})-\frac{2}{3}(\boldsymbol{\tau}_1\times\boldsymbol{\tau}_2)_z\mathbf{k}_2\right]+1\rightleftharpoons 2,(156)$$

$$\mathbf{j}_{\infty,c}^{\text{N}^3\text{LO}} = i\,e\,\frac{1}{48\pi^2 F_\pi^4}\left(\frac{2}{\epsilon}+\dots\right)(\boldsymbol{\tau}_1\times\boldsymbol{\tau}_2)_z\,(\mathbf{k}_1-\mathbf{k}_2)\,,\quad(157)$$

$$\mathbf{j}_{\infty,d}^{\text{N}^3\text{LO}} = i\,e\,\frac{g_A^4}{8\pi^2 F_\pi^4}\left(\frac{2}{\epsilon}+\dots\right)\left[\tau_{2,z}\boldsymbol{\sigma}_1\times(6\mathbf{k}_2-4\mathbf{k}_1)+3(\boldsymbol{\tau}_1\times\boldsymbol{\tau}_2)_z\mathbf{k}_2\right]+1\rightleftharpoons 2,(158)$$

$$\mathbf{j}_{\infty,e}^{\text{N}^3\text{LO}} = i\,e\,\frac{g_A^4}{8\pi^2 F_\pi^4}\left(\frac{2}{\epsilon}+\dots\right)\left[10\,\tau_{2,z}\,\boldsymbol{\sigma}_1\times\mathbf{k}_1+\frac{5}{6}(\boldsymbol{\tau}_1\times\boldsymbol{\tau}_2)_z\,\mathbf{k}_2\right]+1\rightleftharpoons 2\,,\quad(159)$$

$$\mathbf{j}_{\infty,g}^{\text{N}^3\text{LO}} = i\,e\,\frac{g_A^2}{4\pi^2 F_\pi^2}\left(\frac{2}{\epsilon}+\dots\right)(\boldsymbol{\tau}_1\times\boldsymbol{\tau}_2)_z\,C_T\left[\boldsymbol{\sigma}_2\,\boldsymbol{\sigma}_1\cdot\mathbf{q}-\boldsymbol{\sigma}_1\,\boldsymbol{\sigma}_2\cdot\mathbf{q}\right]\,,\quad(160)$$

$$\mathbf{j}_{\infty,i}^{\text{N}^3\text{LO}} = i\,e\,\frac{g_A^2}{4\pi^2 F_\pi^2}\left(\frac{2}{\epsilon}+\dots\right)\tau_{1,z}\left[C_T\,\boldsymbol{\sigma}_2\times\mathbf{q}-C_S\,\boldsymbol{\sigma}_1\times\mathbf{q}\right]+1\rightleftharpoons 2\,,\quad(161)$$

where the dots denote finite contributions depending on the renormalization point. Although we did not derive the finite expressions for the currents of type b), c), and e)—referring to Fig. 25—we remark here that the renormalization procedure is carried out by considering the divergent parts of all the one-loop TPE currents illustrated in Fig. 25. When combined together, all these divergences can be absorbed by the renormalization of the C_i', which is not the case for the individual contributions. We can exploit Fierz identities (or the antisymmetry properties of nucleons' states) to reduce the spin-isospin structure multiplying the renormalization constants above so as to match those entering the contact current at N^3LO. In particular, terms proportional to $(\boldsymbol{\tau}_1\times\boldsymbol{\tau}_2)_z$, can be reduced exploiting the following relation

$$(\boldsymbol{\tau}_1\times\boldsymbol{\tau}_2)_z\,(\mathbf{k}_2-\mathbf{k}_1) = -2\,i\,e_1\,(1+\boldsymbol{\sigma}_1\cdot\boldsymbol{\sigma}_2)(\mathbf{K}_1-\mathbf{K}_2)+1\rightleftharpoons 2\,,\quad(162)$$

and lead to renormalization of the LECs C_3', C_{14}', $(2\,C_1'-C_2')$ and $(2\,C_9'-C_{12}')$, entering Eq. (124). The relations below

$$\begin{aligned}(\tau_{2,z}\,\boldsymbol{\sigma}_1+\tau_{1,z}\,\boldsymbol{\sigma}_2)\times\mathbf{q} &= -(\tau_{1,z}\,\boldsymbol{\sigma}_1+\tau_{2,z}\,\boldsymbol{\sigma}_2)\times\mathbf{q}\\&= \frac{1}{2}(\boldsymbol{\tau}_1\times\boldsymbol{\tau}_2)_z\left[\boldsymbol{\sigma}_1\,\boldsymbol{\sigma}_2\cdot\mathbf{q}-\boldsymbol{\sigma}_2\,\boldsymbol{\sigma}_1\cdot\mathbf{q}\right]\\&= -\frac{1}{2}(\tau_{1,z}-\tau_{2,z})\,(\boldsymbol{\sigma}_1-\boldsymbol{\sigma}_2)\times\mathbf{q}\,,\quad(163)\end{aligned}$$

allow one to reduce the $\mathbf{q}$-dependent structures multiplying the renormalization constants, leading to renormalization of C_{16}', entering Eq. (273).

IV.2.4 One-Loop Corrections to Tree-Level Currents

Contributions in this class are illustrated by the diagrams in Figs. 28 and 29. Before listing the formal expressions obtained for these diagrams, we note that diagrams of panels a)–d) and m)–r) involve three– and four–pion couplings. The Hamiltonians describing these interactions are obtained from the chiral Lagrangians of Ref. [1] by including corrections $\pi^2(\mathbf{x})/F_\pi^2$ in the expansion of D^{-1} factors, where $D \equiv 1 + \pi^2(\mathbf{x})/F_\pi^2$, entering these chiral Lagrangians. The explicit expressions for the $H_{3\pi NN}$ and $H_{4\pi}$ Hamiltonians are given in Appendix A, along with the corresponding minimal Hamiltonians $H_{\gamma 3\pi NN}$ and $H_{\gamma 4\pi}$. The scaling of the vertices implied by these interactions is summarized in Table 6.

	Q-scaling		Q-scaling
$H_{3\pi NN}$	Q	$H_{\gamma 3\pi NN}$	$e\,Q^0$
$H_{4\pi}$	Q^2	$H_{\gamma 4\pi}$	$e\,Q$

TABLE 6: Powers of Q, the small momentum scale, associated with the vertices from the strong- and electromagnetic-interaction Hamiltonians of Eqs. (277), (278), (282), and (283).

We express the amplitudes corresponding to diagrams in Figs. 28 and 29 in terms of the kernels $I_{ij}^{(2)}(\mathbf{q})$ and $J_{ij}^{(2)}(\mathbf{q})$, and renormalization constants $M^{(n)}$, given in Appendix C. In particular, referring to Fig. 28 we find

$$\text{type a)} \;=\; \mathbf{j}_{\mathrm{b}}^{\mathrm{NLO}}\left[-\frac{3}{2\,F_\pi^2}\,M^{(1)}\right] \,, \tag{164}$$

$$\text{type b)} \;=\; -i\,e\frac{g_A^2}{F_\pi^2}\,(\boldsymbol{\tau}_1 \times \boldsymbol{\tau}_2)_z\,\boldsymbol{\sigma}_1\,\frac{\boldsymbol{\sigma}_2\cdot\mathbf{k}_2}{\omega_{k_2}^2}\left[-\frac{1}{\omega_{k_2}^2}\frac{m_\pi^2}{F_\pi^2}\,M^{(1)}\right] + 1 \rightleftharpoons 2 \,, \tag{165}$$

$$\text{type c)} \;=\; \mathbf{j}_{\mathrm{b}}^{\mathrm{NLO}}\left[-\frac{5}{2\,F_\pi^2}\,M^{(1)}\right] \,, \tag{166}$$

$$\text{type d)} \;=\; -i\,e\frac{g_A^2}{2\,F_\pi^4}(\boldsymbol{\tau}_1 \times \boldsymbol{\tau}_2)_z\,I_{ij}^{(2)}(\mathbf{q})\,\sigma_{1,j}\,\frac{\boldsymbol{\sigma}_2\cdot\mathbf{k}_2}{\omega_{k_2}^2} + 1 \rightleftharpoons 2 \,, \tag{167}$$

$$\text{type e)} \;=\; \mathbf{j}_{\mathrm{b}}^{\mathrm{NLO}}\left[\frac{1}{F_\pi^2}\,M^{(1)}\right] \,, \tag{168}$$

$$\text{type f)} \;=\; i\,e\frac{g_A^2}{2\,F_\pi^4}(\boldsymbol{\tau}_1 \times \boldsymbol{\tau}_2)_z\,I_{ij}^{(2)}(\mathbf{q})\,\sigma_{1,j}\,\frac{\boldsymbol{\sigma}_2\cdot\mathbf{k}_2}{\omega_{k_2}^2} + 1 \rightleftharpoons 2 \,, \tag{169}$$

$$\text{type j)} \;=\; i\,e\frac{2\,g_A^4}{F_\pi^4}\,\tau_{2,z}\,J_{ij}^{(2)}(\mathbf{q})\,(\mathbf{k}_2 \times \mathbf{q})_j\,\frac{\boldsymbol{\sigma}_2\cdot\mathbf{k}_2}{\omega_{k_2}^2} + 1 \rightleftharpoons 2 \,, \tag{170}$$

$$\text{type k)} \;=\; \text{type l)} = \mathbf{j}_{\mathrm{b}}^{\mathrm{NLO}}\left[\frac{g_A^2}{6\,F_\pi^2}\,M^{(3)}\right] \,, \tag{171}$$
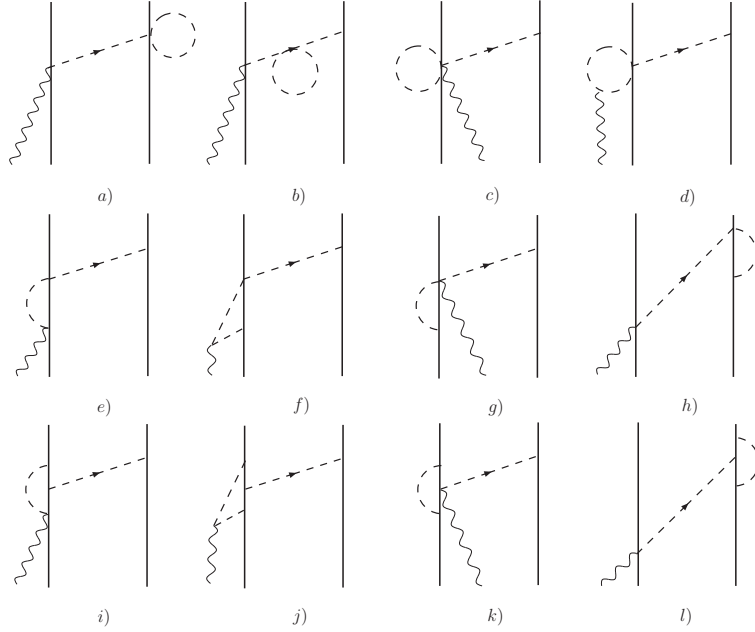
FIG. 28: Diagrams illustrating loop corrections to tree-level two-body currents, notation as in Fig. 20. Only one among the possible time orderings is shown for each contribution.

while diagrams in Fig. 29 give the following amplitudes:

$$\text{type m) + type n)} = \mathbf{j}_c^{\text{NLO}} \left[-\frac{3}{F_\pi^2} M^{(1)} \right] , \tag{172}$$

$$\text{type o) + type p)} = \mathbf{j}_c^{\text{NLO}} \left(-\frac{1}{\omega_{k_1}^2} - \frac{1}{\omega_{k_2}^2} \right) \frac{m_\pi^2}{F_\pi^2} M^{(1)} , \tag{173}$$

$$\text{type q)} = \mathbf{j}_c^{\text{NLO}} \left[-\frac{5}{F_\pi^2} M^{(1)} \right] , \tag{174}$$

$$\text{type r)} = i\, e \frac{g_A^2}{F_\pi^4} (\boldsymbol{\tau}_1 \times \boldsymbol{\tau}_2)_z \, I_{ij}^{(2)}(\mathbf{q}) \, (\mathbf{k}_1 - \mathbf{k}_2)_j \frac{\boldsymbol{\sigma}_1 \cdot \mathbf{k}_1}{\omega_{k_1}^2} \frac{\boldsymbol{\sigma}_2 \cdot \mathbf{k}_2}{\omega_{k_2}^2} , \tag{175}$$

$$\text{type u) + type v)} = \mathbf{j}_c^{\text{NLO}} \left[\frac{g_A^2}{3\,F_\pi^2} M^{(3)} \right] , \tag{176}$$

where $\mathbf{j}_b^{\text{NLO}}$ and $\mathbf{j}_c^{\text{NLO}}$ are the seagull and pion-in-flight currents of Eqs. (106) and (107). The contributions associated with diagrams of type h), i), s), and t) vanish, since the integrand is an odd function of the loop momentum $\mathbf{p}$. Contributions of diagrams d) and f) exactly cancel out. Lastly, diagrams of type g), along with those represented in Fig. 30, are of order $e\,Q^2$, and therefore beyond the order
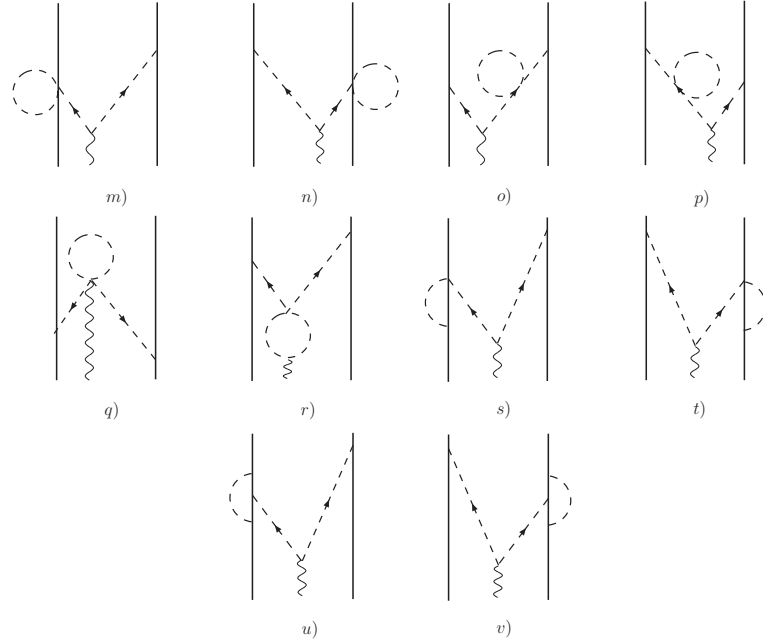
FIG. 29: Same as in Fig. 28.

under consideration in the present study.

The evaluation of the diagrams in the last row of Figs. 28 and 29 is carried out by including recoil corrections to the reducible diagrams of corresponding topology. Cancellations occur between the irreducible and these recoil-corrected reducible contributions. This aspect of the calculation is discussed in more detail in Appendix D, along with the derivation of the current of type j), for which only a subset of irreducible diagrams is retained in the evaluation of the corresponding amplitude.

Loop corrections to the LO tree-level current contribute to renormalize the axial coupling constant, g_A, and the pion mass, m_π, entering the LO current operator. Specifically, from the expressions listed in Eqs. (164)-(176), it is easily seen that the contributions of type a), c), e), k)-l), m)-n), q), and u)-v) lead to further renormalization of g_A, while those of type b) and o)-p) renormalize the pion mass, namely $\overline{m}_\pi^2 = m_\pi^2(1 + M^{(1)}/F_\pi^2)$. Thus, both types are accounted for in the renormalized seagull, $\mathbf{j}_b^{\mathrm{NLO}}$, and pion-in-flight, $\mathbf{j}_c^{\mathrm{NLO}}$, currents.

Diagrams j) and r) generate form-factor corrections to the nucleon and pion electromagnetic couplings. The latter follow from the finite parts of the $I_{ij}^{(2)}$ and $J_{ij}^{(2)}$

kernels entering Eqs. (170) and (175). These corrections to the electromagnetic coupling of the nucleons are accounted for implicitly, since we use the experimental values of the anomalous magnetic moments of the nucleons, and give there form factor corrections.
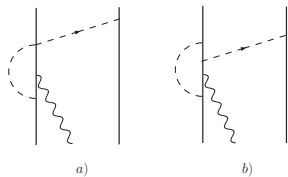
FIG. 30: Diagrams illustrating N^4LO ($e\,Q^2$) loop corrections to tree-level currents not included in the present study, notation as in Fig. 20.

IV.3   THREE-BODY CURRENTS AT N^3LO

So far we explored the two-nucleon system, and derived the NN interaction as well as the two-body electromagnetic current up to N^2LO and N^3LO, respectively. A natural question to ask is whether there are three-body components entering the nuclear potential and/or electromagnetic current at the order we are investigating. To answer this question, we need to classify the diagrams involving three nucleons entering the potential (and current) contributions.

Consider first the diagrams in panel a) and b) of Fig. 31. These disconnected diagrams arise from considering two nucleons interacting via the LO two-body potential derived in Sec. III, while the third nucleon acts as a spectator. Following the power counting rules established earlier, we find that these diagrams scale as Q^{-3}. Similarly, disconnected diagrams involving nucleons interacting via the two-body potential at N^2LO scale as Q^{-1}, as can be inferred from panels c) and d) of Fig. 31 (the dots indicate disconnected diagrams where two nucleons are interacting via the remaining TPE contributions to the NN potential). These disconnected three-body contributions at Q^{-3} and Q^{-1} are accounted for when the two-body potential is used to generate the nuclear wave functions of a three-body system. According to the power counting scheme, genuine three-body forces occur at Q^{-1} and they are represented by the diagrams in Fig. 32. We find that the amplitude implied by the diagram in panel a) vanishes. Specifically, referring to Fig. 33, where we illustrate
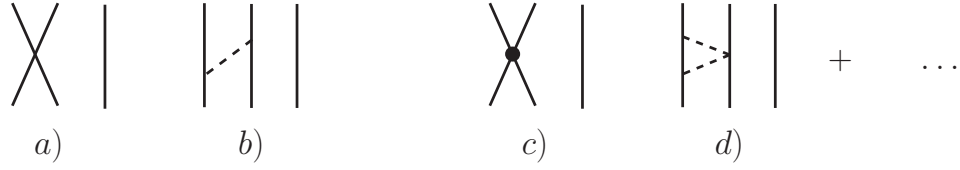
FIG. 31: Diagrams illustrating disconnected three-body contributions to the $NN \rightarrow NN$ transition amplitude at order Q^{-3}, panels a) and b), and at order Q^{-1}, panels c) and d). Notation as in Fig. 20.
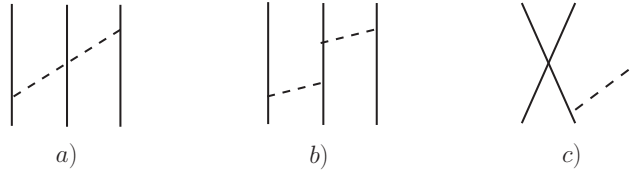
FIG. 32: Diagrams illustrating the three-body contributions to the $NN \rightarrow NN$ transition amplitude at order Q^{-1}. Notation as in Fig. 20. Only one of the possible time-ordered diagrams is shown.

the complete set of time-ordered diagrams associated with this amplitude, we find that contributions arising from diagrams in panels a), b) and c) are exactly canceled by those arising from diagrams in panels d), e) and f), respectively. For example, the amplitude implied by the diagram in panel a) is equal to that one associated with the diagram in panel d) but for an overall sign. This sign difference follows from the Weinberg-Tomozawa interaction associated with nucleon 2 and the exchanged pions with momenta $\mathbf{q}_1$ and $\mathbf{q}_2$, and isospin components a and b. The vertex entering the diagram in panel a), implied by the Weinberg-Tomozawa Hamiltonian given in Eq. (236), has the same structure as that entering the diagram in panel d), but for the aforementioned sign

$$V_{\mathrm{W-T}}(2, \mathbf{q}_1, \mathbf{q}_2)\big|_{\mathrm{panel\,a)}} = \frac{i}{F_\pi^2} \frac{\omega_1 + \omega_2}{\sqrt{4\,\omega_1\omega_2}}\, \epsilon_{abc}\, \tau_{2,c} = -\, V_{\mathrm{W-T}}(2, \mathbf{q}_1, \mathbf{q}_2)\big|_{\mathrm{panel\,d)}} \ . \qquad (177)$$

A similar argument applies to diagrams in panels b)-e) and c)-f) of the same figure.

Diagrams illustrated in panels b) and c) of Fig. 32 have both reducible and irreducible topologies, as shown in Fig. 34, and recoil corrected reducible contributions
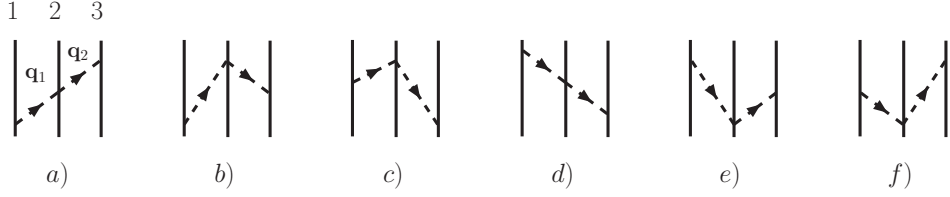
FIG. 33: Complete set of time-ordered diagrams for the three-body force illustrated in panel a) of Fig. 32. Notation as in Fig. 20.

exactly cancel out the corresponding irreducible terms, leading to vanishing amplitudes (these cancellations had also be found in [2]). Therefore, at the order we are interested in, there are no 'genuine' three-body forces.
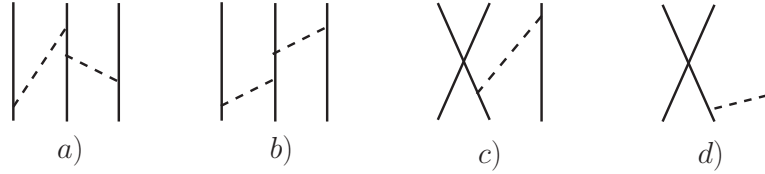
FIG. 34: Irreducible, panels a) and c), and reducible, panels b) and d), contributions, to the three-body forces illustrated in panels b) and c) of Fig. 32. Notation as in Fig. 20. Only one of the possible time-ordered diagrams is shown.

Having proved that three-body forces do not occur at N^2LO, we expect that three-body currents at N^3LO either vanish or they must be transverse to the photon field in order to satisfy the continuity equation (see Sec. IV.4). Genuine three-body currents occur at $e\,Q^{-2}$ and are represented by the diagrams illustrated in Fig. 35. Indeed, the three-body currents implied by the amplitudes associated with these diagrams vanish, and cancellations occur as discussed for the case of the three-body forces. Therefore at N^3LO the current operator is completely determined by the one– and two–body contributions derived in the present work.

IV.4 CURRENT CONSERVATION

In the present formulation, the *NN* potential and the electromagnetic current operators have been derived in TOPT with the additional prescription of retaining recoil
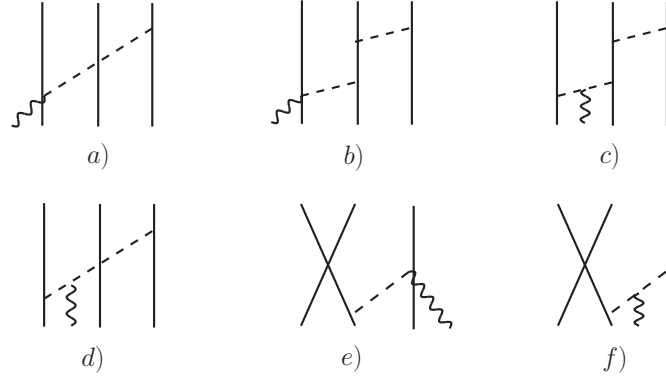
FIG. 35: Diagrams illustrating the three-body contributions to the $\gamma NN \to NN$ transition amplitude at order $e\,Q^{-2}$. Notation as in Fig. 20. Only one of the possible time-ordered diagrams is shown.

corrected reducible contributions in the evaluation of the corresponding transition amplitudes. It is important to verify whether this formalism leads to currents which are conserved, $i.e.$, we want to verify that the current operator satisfies the continuity equation

$$\mathbf{q} \cdot \mathbf{j} = \left[\frac{p_1^2}{2\,m_N} + \frac{p_2^2}{2\,m_N} + v_{12} , \, \rho^{\text{LO}} \right] , \qquad (178)$$

where $\mathbf{q}$ is momentum transfer by the external photon, and ρ^{LO} is the charge operator given by

$$\rho^{\text{LO}} = \rho_1^{\text{LO}} + \rho_2^{\text{LO}} = e\,(e_{N,1} + e_{N,2}) = e \left[\frac{1 + \tau_{1,z}}{2} + \frac{1 + \tau_{2,z}}{2} \right] . \qquad (179)$$

Note that the vertex implied by the charge operator scales as e, therefore the one-body (disconnected contribution) charge operator scales as $e\,Q^{-3}$, and occurs at LO. In the χEFT formulation, the current is conserved order by order in the power expansion. For example, it is easily verified that the LO current operator satisfies the continuity equation with the kinetic energy term of the nuclear Hamiltonian. The OPE currents at NLO satisfy the continuity equation with the LO OPE contribution to the potential. The N^{2}LO currents arising from relativistic corrections to the LO one-body term require the inclusion of these corrections also in the charge operator, in order for the continuity equation to be satisfied. We will not discuss them further here.
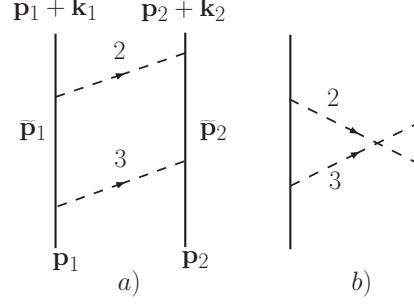
FIG. 36: Diagrams illustrating the reducible, panel a), and irreducible, panel b), two-body 'box' potential. Only one among the possible time orderings is shown. Notation is as in Fig. 20.

We have explicitly verified that the N³LO current operators obtained in Secs. IV.2.1–IV.2.3—here denoted as $\mathbf{j}^{\mathrm{N^3LO}}$—satisfy the continuity equation with the N²LO potential $v^{\mathrm{N^2LO}}$ derived in Sec. III.1, $i.e.$

$$\mathbf{q} \cdot \mathbf{j}^{\mathrm{N^3LO}} = \left[v^{\mathrm{N^2LO}}, \rho^{\mathrm{LO}} \right] . \tag{180}$$

Due to the structure of the LO charge operator, isospin independent terms of the NN potential generate a vanishing commutator, thus to these terms correspond vanishing currents or currents which are orthogonal to the external photon momentum. For example, the loop potential of type i) defined in Eq. (68) is isospin independent and the corresponding current—Eq. (154)—is transverse. Currents of non-minimal nature are by construction transverse, since they are not generated by gauging derivative couplings in the strong interaction Hamiltonians, but enter via coupling to the electromagnetic tensor $F_{\mu\nu}$.

The calculation of the commutator in Eq. (180) is straightforward for the contact potential at N²LO, and leads to the conservation of the minimal contact current at N³LO. Therefore, we discuss in more detail its evaluation for loop contributions which involve reducible diagrams. We illustrate the calculation carried out for the currents of type d) and e) of Fig. 25. The potential generated by the 'box' diagrams is given in Eq. (59) and reads

$$v_{\mathrm{f}}(\mathbf{k}) = -\frac{2\,g_A^4}{F_\pi^4} \int \frac{\omega_2^2 + \omega_3^2 + \omega_2\,\omega_3}{\omega_2^3\,\omega_3^3\,(\omega_2 + \omega_3)} \left[2\,\boldsymbol{\tau}_1 \cdot \boldsymbol{\tau}_2\,(\mathbf{q}_2 \cdot \mathbf{q}_3)^2 + 3\,\boldsymbol{\sigma}_1 \cdot (\mathbf{q}_2 \times \mathbf{q}_3)\,\boldsymbol{\sigma}_2 \cdot (\mathbf{q}_2 \times \mathbf{q}_3) \right] , \tag{181}$$

where the integration is carried out on one of the internal momenta. The latter are labelled as indicated in Fig. 36, therefore $\mathbf{q}_2 + \mathbf{q}_3 = \mathbf{k}_2 = -\mathbf{k}_1$. Evaluation of the

commutator of $v_{\mathrm{f}}(\mathbf{k})$ with the charge operator gives

$$
\begin{aligned}
\left[\, v_{\mathrm{f}}(\mathbf{k})\,,\,\rho^{\mathrm{LO}}\,\right] &= v_{\mathrm{f}}(\mathbf{k}-\mathbf{q}/2)\,\rho_1^{\mathrm{LO}} - \rho_1^{\mathrm{LO}}\,v_{\mathrm{f}}(\mathbf{k}-\mathbf{q}/2) + 1 \rightleftharpoons 2 \\
&= -i\,e\frac{2\,g_A^4}{F_\pi^4}(\boldsymbol{\tau}_1\times\boldsymbol{\tau}_2)_z\int\frac{\omega_2^2+\omega_3^2+\omega_2\,\omega_3}{\omega_2^3\omega_3^3(\omega_2+\omega_3)}(\mathbf{q}_2\cdot\mathbf{q}_3)^2 + 1 \rightleftharpoons 2, \quad (182)
\end{aligned}
$$

where now $\mathbf{k}_1+\mathbf{k}_2=\mathbf{q}$ and $\mathbf{q}_2+\mathbf{q}_3=\mathbf{k}_2$, and the isospin structure comes from the evaluation of the commutator

$$
[\boldsymbol{\tau}_1\cdot\boldsymbol{\tau}_2\,,\,\tau_{1,z}] = 2\,i\,(\boldsymbol{\tau}_1\times\boldsymbol{\tau}_2)_z\ . \tag{183}
$$

Currents of type d) and e) in Fig. 25, combined together, satisfy the continuity equation with the 'box' potential. In particular, the l.h.s. of Eq. (178) for the currents of type d) given in Eq. (133) and illustrated in Fig. 25 reads

$$
\begin{aligned}
\mathbf{q}\cdot\mathbf{j}_{\mathrm{d}}^{\mathrm{N^3LO}} = {} & -i\,e\frac{2\,g_A^4}{F_\pi^4}\int\frac{\omega_2^2+\omega_3^2+\omega_2\omega_3}{\omega_2^3\,\omega_3^3\,(\omega_2+\omega_3)}\bigg[(\boldsymbol{\tau}_1\times\boldsymbol{\tau}_2)_z\,\mathbf{q}_2\,(\mathbf{q}_2\cdot\mathbf{q}_3) \\
& + 2\,\tau_{2,z}\,(\mathbf{q}_2\cdot\mathbf{q}_3)\,(\boldsymbol{\sigma}_1\times\mathbf{q}_2) + 2\,\tau_{1,z}\,\mathbf{q}_2\,\boldsymbol{\sigma}_2\cdot(\mathbf{q}_3\times\mathbf{q}_2)\bigg]\cdot\mathbf{q} + 1 \rightleftharpoons 2\,,(184)
\end{aligned}
$$

where again momentum conservation requires that $\mathbf{k}_1+\mathbf{k}_2=\mathbf{q}$ and $\mathbf{q}_2+\mathbf{q}_3=\mathbf{k}_2$. The l.h.s. of Eq. (180) for the currents of type e) given in Eq. (134) and represented in Fig. 25 reads

$$
\begin{aligned}
\mathbf{q}\cdot\mathbf{j}_{\mathrm{e}}^{\mathrm{N^3LO}} = {} & i\,e\frac{2\,g_A^4}{F_\pi^4}\int\left[\frac{\omega_2^2+\omega_3^2+\omega_2\,\omega_3}{\omega_2^3\omega_3^3(\omega_2+\omega_3)} - \frac{\omega_1^2+\omega_2^2+\omega_1\,\omega_2}{\omega_1^3\omega_2^3(\omega_1+\omega_2)}\right] \\
& \times\bigg[(\boldsymbol{\tau}_1\times\boldsymbol{\tau}_2)_z\,(\mathbf{q}_1\cdot\mathbf{q}_2)(\mathbf{q}_2\cdot\mathbf{q}_3) + 2\,\tau_{2,z}\,(\mathbf{q}_2\cdot\mathbf{q}_3)\,\boldsymbol{\sigma}_1\cdot(\mathbf{q}_2\times\mathbf{q}_1) \\
& + 2\,\tau_{1,z}\,(\mathbf{q}_1\cdot\mathbf{q}_2)\,\boldsymbol{\sigma}_2\cdot(\mathbf{q}_3\times\mathbf{q}_2)\bigg]\,, \tag{185}
\end{aligned}
$$

where $\mathbf{q}_1=\mathbf{q}_2+\mathbf{k}_1$. The factor in the square brackets of the last equation comes from the product $\mathbf{q}\cdot(\mathbf{q}_1-\mathbf{q}_3)\,f(\omega_1,\omega_2,\omega_3)$,

$$
\mathbf{q}\cdot(\mathbf{q}_1-\mathbf{q}_3)\,f(\omega_1,\omega_2,\omega_3) = \left(q_1^2-q_3^2\right)f(\omega_1,\omega_2,\omega_3) = \left(\omega_1^2-\omega_3^2\right)f(\omega_1,\omega_2,\omega_3)\,, \tag{186}
$$

where $f(\omega_1,\omega_2,\omega_3)$ defined as in Eq. (135). Combining Eqs. (184)–(185), we obtain

$$
\begin{aligned}
\mathbf{q}\cdot(\mathbf{j}_{\mathrm{d}}+\mathbf{j}_{\mathrm{e}}) = {} & -i\,e\frac{2\,g_A^4}{F_\pi^4}\int\frac{\omega_2^2+\omega_3^2+\omega_2\omega_3}{\omega_2^3\,\omega_3^3\,(\omega_2+\omega_3)}\bigg[(\boldsymbol{\tau}_1\times\boldsymbol{\tau}_2)_z\,(\mathbf{q}_2\cdot\mathbf{q}_3)^2 \\
& + 2\,\tau_{2,z}\,(\mathbf{q}_2\cdot\mathbf{q}_3)\,\boldsymbol{\sigma}_1\cdot(\mathbf{q}_2\times\mathbf{q}_3) + 2\,\tau_{1,z}\,(\mathbf{q}_2\cdot\mathbf{q}_3)\,\boldsymbol{\sigma}_2\cdot(\mathbf{q}_3\times\mathbf{q}_2)\bigg] + 1 \rightleftharpoons 2.(187)
\end{aligned}
$$

Finally, we note that the last two terms of the previous equation vanish. This is easily seen by changing $\mathbf{q}_2 \to \mathbf{k}_2/2 + \mathbf{q}_2$ (implying $\mathbf{q}_3 = \mathbf{k}_2/2 - \mathbf{q}_2$), and observing that the integrands are odd under $\mathbf{q}_2 \to -\mathbf{q}_2$. Hence we are left with the first term which is equal to Eq. (182), showing that the continuity equation is indeed satisfied.

This proves that the prescription of including recoil corrected reducible contributions to the evaluation of the transition amplitudes leads to conserved currents. We note in closing that, if irreducible contributions only are retained in both the potential and currents, then the continuity equation is not satisfied.

IV.5   CURRENTS IN CONFIGURATION SPACE

Before we turn our attention to the derivation of the magnetic moment associated with the currents derived in the present work, we briefly discuss the regularization of the current matrix elements. The calculations of electromagnetic observables reported in Sec. VI are carried out in configuration space, and hence configuration-space representations of the current operators are needed. Those of the one-body operators, that is the current at LO, Eq. (104), and the relativistic correction to the LO current, Eq. (108), generically denoted as $\mathbf{j}^{(1)}$, follow from

$$\mathbf{j}^{(1)}(\mathbf{q}) = \int_{\mathbf{k}_1} \int_{\mathbf{K}_1} e^{i\mathbf{k}_1 \cdot (\mathbf{r}_1' + \mathbf{r}_1)/2} \, e^{i\mathbf{K}_1 \cdot (\mathbf{r}_1' - \mathbf{r}_1)} \, \overline{\delta}(\mathbf{k}_1 - \mathbf{q}) \, \mathbf{j}^{(1)}(\mathbf{k}_1, \mathbf{K}_1) \, , \qquad (188)$$

while those for the two-body current operators $\mathbf{j}^{(2)}$ are derived from

$$\begin{aligned}
\mathbf{j}^{(2)}(\mathbf{q}) &= \int_{\mathbf{k}_1} \int_{\mathbf{k}_2} \int_{\mathbf{K}_1} \int_{\mathbf{K}_2} e^{i\mathbf{k}_1 \cdot (\mathbf{r}_1' + \mathbf{r}_1)/2} \, e^{i\mathbf{K}_1 \cdot (\mathbf{r}_1' - \mathbf{r}_1)} \, e^{i\mathbf{k}_2 \cdot (\mathbf{r}_2' + \mathbf{r}_2)/2} \, e^{i\mathbf{K}_2 \cdot (\mathbf{r}_2' - \mathbf{r}_2)} \\
&\qquad \times \overline{\delta}(\mathbf{k}_1 + \mathbf{k}_2 - \mathbf{q}) \, \mathbf{j}^{(2)}(\mathbf{k}_1, \mathbf{k}_2, \mathbf{K}_1, \mathbf{K}_2) \, , \qquad (189)
\end{aligned}$$

where the momenta $\mathbf{k}_i$ and $\mathbf{K}_i$ are defined as in Eq. (103). In particular, $\mathbf{K}_i \to -i\nabla_i' \delta(\mathbf{r}_i' - \mathbf{r}_i)$, $i.e.$ the configuration-space representation of the momentum operator. The equation above for current operators which do not depend explicitly on the momenta $\mathbf{K}_i$ reduces to

$$\begin{aligned}
\mathbf{j}^{(2)}(\mathbf{q}) &= \int_{\mathbf{k}_1} \int_{\mathbf{k}_2} e^{i\mathbf{k}_1 \cdot \mathbf{r}_1} \, e^{i\mathbf{k}_2 \cdot \mathbf{r}_2} \, \overline{\delta}(\mathbf{k}_1 + \mathbf{k}_2 - \mathbf{q}) \, \mathbf{j}^{(2)}(\mathbf{k}_1, \mathbf{k}_2) \\
&= e^{i\mathbf{q} \cdot \mathbf{R}} \int_{\mathbf{k}} e^{i\mathbf{k} \cdot \mathbf{r}} \, \mathbf{j}^{(2)}(\mathbf{q}, \mathbf{k}) \, , \qquad (190)
\end{aligned}$$

where

$$\mathbf{R} = (\mathbf{r}_1 + \mathbf{r}_2)/2 \, , \qquad\qquad \mathbf{r} = \mathbf{r}_1 - \mathbf{r}_2 \, , \qquad (191)$$

are the center-of-mass and relative positions of the two nucleons.

The current operator needs to be further regularized in order to avoid singularities in the current matrix elements. The regularization is accomplished by the insertion of a momentum cutoff which we choose to be of the form

$$C_\Lambda(k) = \mathrm{e}^{-(k/\Lambda)^4} \ , \tag{192}$$

to preserve the power counting of the currents. In Sec. VI we will study the sensitivity of the calculated electromagnetic observables to variations of the cutoff parameter Λ.

CHAPTER V

MAGNETIC MOMENT AT N^{3}LO

The static magnetic moment operator related to a two-body current density $\mathbf{J}(\mathbf{x})$ is defined as

$$\boldsymbol{\mu}(\mathbf{R}, \mathbf{r}) = \frac{1}{2} \int d\mathbf{x} \, [\mathbf{x} \times \mathbf{J}(\mathbf{x})] \ , \tag{193}$$

where $\mathbf{R}$ and $\mathbf{r}$ are respectively the center-of-mass and relative positions of the two nucleons, defined as in Eq. (191). The operator above can be separated into a term dependent on the center-of-mass position of the two particles and one independent of it [43, 44], as

$$\boldsymbol{\mu}(\mathbf{R}, \mathbf{r}) = \frac{1}{2} \left[\mathbf{R} \times \int d\mathbf{x} \, \mathbf{J}(\mathbf{x}) + \int d\mathbf{x} \, (\mathbf{x} - \mathbf{R}) \times \mathbf{J}(\mathbf{x}) \right] , \tag{194}$$

where, because of translational invariance, $\mathbf{J}(\mathbf{x})$ is actually a function of $\mathbf{J}(\mathbf{x} - \mathbf{R}, \mathbf{r})$. The first term in the square brackets is referred to as the Sachs moment, $\boldsymbol{\mu}_{\text{Sachs}}$, and using integration by parts

$$\int d\mathbf{x} \, \mathbf{J}_i(\mathbf{x}) = \int d\mathbf{x} \, \nabla \cdot [\mathbf{x}_i \, \mathbf{J}(\mathbf{x})] - \int d\mathbf{x} \, \mathbf{x}_i \, \nabla \cdot \mathbf{J}(\mathbf{x}) \ , \tag{195}$$

it can be rewritten as

$$\boldsymbol{\mu}_{\text{Sachs}}(\mathbf{R}, \mathbf{r}) = -\frac{\mathbf{R}}{2} \times \int d\mathbf{x} \, \mathbf{x} \, \nabla \cdot \mathbf{J}(\mathbf{x}) \ . \tag{196}$$

The Sachs magnetic moment associated with a two-body current distribution is related to the nuclear potential v_{12}, via the continuity equation, which reads in r-space

$$\nabla \cdot \mathbf{J} = i \, [\rho, \, H] \ , \tag{197}$$

where H is the two-body nuclear Hamiltonian, ρ is the one-body charge density operator introduced in Eq. (179)—there it is expressed in momentum space—and we dropped the superscript LO for simplicity. The configuration representation of the charge operator reads

$$\rho(\mathbf{x}) = e \frac{1 + \tau_{1,z}}{2} \delta(\mathbf{x} - \mathbf{r}_1) + e \frac{1 + \tau_{2,z}}{2} \delta(\mathbf{x} - \mathbf{r}_2) \ . \tag{198}$$

Insertion of Eq. (197) into Eq. (196) leads to

$$\boldsymbol{\mu}_{\text{Sachs}}(\mathbf{R}, \mathbf{r}) = -i \frac{\mathbf{R}}{2} \times \int d\mathbf{x} \, \mathbf{x} \, [\rho(\mathbf{x}), \, v_{12}] \ , \tag{199}$$

where we dropped kinetic terms in the Hamiltonian, since they lead to one-body components of the magnetic moment operator. This relation is general and independent on the nature and form of the nuclear potential v_{12}. It indicates that the Sachs magnetic moment is uniquely determined by the interaction between the two nucleons. In particular, non vanishing terms of the commutator between the charge operator and the nuclear interaction are due to components of the potential which depend on the momenta of the nucleons and/or on isospin structures which do not commute with $\tau_{i,z}$, with $i = 1, 2$.

The expression given in Eq. (193) can be written equivalently as

$$\boldsymbol{\mu}(\mathbf{R}, \mathbf{r}) = -\frac{i}{2} \nabla_q \times \mathbf{j}(\mathbf{q}) \bigg|_{\mathbf{q}=0} , \qquad (200)$$

where $\mathbf{j}(\mathbf{q})$ is defined as in Eq. (190), *i.e.*

$$\begin{aligned}
\mathbf{j}(\mathbf{q}) &= \int_{\mathbf{k}_1} \int_{\mathbf{k}_2} e^{i\mathbf{k}_1 \cdot \mathbf{r}_1} e^{i\mathbf{k}_2 \cdot \mathbf{r}_2} \, \overline{\delta}(\mathbf{k}_1 + \mathbf{k}_2 - \mathbf{q}) \, \mathbf{j}(\mathbf{k}_1, \mathbf{k}_2) \\
&= e^{i\,\mathbf{q}\cdot\mathbf{R}} \int_{\mathbf{k}} e^{i\,\mathbf{k}\cdot\mathbf{r}} \mathbf{j}(\mathbf{q}, \mathbf{k}) .
\end{aligned} \qquad (201)$$

Insertion of the equation above into Eq. (200) leads to

$$\boldsymbol{\mu}(\mathbf{R}, \mathbf{r}) = \frac{1}{2} \left[\mathbf{R} \times \int_{\mathbf{k}} e^{i\,\mathbf{k}\cdot\mathbf{r}} \, \mathbf{j}(0, \mathbf{k}) - i \int_{\mathbf{k}} e^{i\,\mathbf{k}\cdot\mathbf{r}} \nabla_q \times \mathbf{j}(\mathbf{q}, \mathbf{k}) \bigg|_{\mathbf{q}=0} \right] . \qquad (202)$$

Comparing Eq. (202) with Eqs. (194) and (199), we find that the Sachs and the translational invariant magnetic moments can be expressed as

$$\begin{aligned}
\boldsymbol{\mu}_{\text{Sachs}}(\mathbf{R}, \mathbf{r}) &= -i \frac{\mathbf{R}}{2} \times \int d\mathbf{x}\, \mathbf{x} \left[\rho(\mathbf{x}), v_{12} \right] = \frac{\mathbf{R}}{2} \times \int_{\mathbf{k}} e^{i\,\mathbf{k}\cdot\mathbf{r}} \, \mathbf{j}(0, \mathbf{k}) , \quad (203) \\
\boldsymbol{\mu}_{\text{T}}(\mathbf{R}, \mathbf{r}) &= \int d\mathbf{x}\, (\mathbf{x} - \mathbf{R}) \times \mathbf{J}(\mathbf{x}) = -\frac{i}{2} \int_{\mathbf{k}} e^{i\,\mathbf{k}\cdot\mathbf{r}} \nabla_q \times \mathbf{j}(\mathbf{q}, \mathbf{k}) \bigg|_{\mathbf{q}=0} , \quad (204)
\end{aligned}$$

from which their momentum space representations follow as

$$\boldsymbol{\mu}_{\text{Sachs}}(\mathbf{R}, \mathbf{k}) = \frac{\mathbf{R}}{2} \times \mathbf{j}(0, \mathbf{k}) , \qquad (205)$$

$$\boldsymbol{\mu}_{\text{T}}(\mathbf{k}) = -\frac{i}{2} \nabla_q \times \mathbf{j}(\mathbf{q}, \mathbf{k})\big|_{\mathbf{q}=0} . \qquad (206)$$

The following sections are dedicated to the derivation of the magnetic moment associated with the currents at N³LO discussed in Sec. IV.2.

V.1   MAGNETIC MOMENTS FROM LOOP CURRENTS

The one-loop two-body current $\mathbf{j}_{\text{loop}}^{\text{N}^3\text{LO}}$ illustrated in Fig. 25 generates a magnetic moment which consists of Sachs and translationally invariant components:

$$\boldsymbol{\mu}_{\text{loop}}^{\text{N}^3\text{LO}} \;=\; \boldsymbol{\mu}_{\text{Sachs}}^{\text{loop}} + \boldsymbol{\mu}_{\text{T}}^{\text{loop}} \; . \tag{207}$$

The Sachs magnetic moment follows from the evaluation of Eq. (199) with the two-body potential $v^{2\pi}$ of Eq. (72). The latter can be separate into an isospin independent term, $v_0^{2\pi}$, and a term which depends on it, $v_{\text{I}}^{2\pi}$

$$v^{2\pi}(\mathbf{r}) = v_0^{2\pi}(\mathbf{r}) + \boldsymbol{\tau}_1 \cdot \boldsymbol{\tau}_2 \, v_{\text{I}}^{2\pi}(\mathbf{r}) \; . \tag{208}$$

Insertion of the equation above into Eq. (199) leads to

$$\begin{aligned}
\boldsymbol{\mu}_{\text{Sachs}}^{\text{loop}}(\mathbf{R}, \mathbf{r}) &= -i\frac{\mathbf{R}}{2} \times \int d\mathbf{x} \, \mathbf{x} \left[e\,\frac{1 + \tau_{1,z}}{2}\, \delta(\mathbf{x} - \mathbf{r}_1)\,,\, \boldsymbol{\tau}_1 \cdot \boldsymbol{\tau}_2 \, v_{\text{I}}^{2\pi}(\mathbf{r}) \right] + 1 \rightleftharpoons 2 \\
&= -\frac{1}{2}\, e\,(\boldsymbol{\tau}_1 \times \boldsymbol{\tau}_2)_z \, v_{\text{I}}^{2\pi}(\mathbf{r})\, \mathbf{R} \times \mathbf{r} \; , \tag{209}
\end{aligned}$$

from which the momentum space representation follows as

$$\boldsymbol{\mu}_{\text{Sachs}}^{\text{loop}}(\mathbf{R}, \mathbf{k}) = -\frac{i}{2} e\,(\boldsymbol{\tau}_1 \times \boldsymbol{\tau}_2)_z \, \mathbf{R} \times \nabla_k \, \overline{v}_{\text{I}}^{2\pi}(\mathbf{k}) \; , \tag{210}$$

where $\overline{v}_{\text{I}}^{2\pi}(\mathbf{k})$ denotes the Fourier transform of $v_{\text{I}}^{2\pi}(\mathbf{r})$, *i.e.*

$$\overline{v}_{\text{I}}^{2\pi}(k) = \frac{1}{48\pi^2\, F_\pi^4} G(k) \left[4m_\pi^2(1 + 4g_A^2 - 5g_A^4) + k^2(1 + 10g_A^2 - 23g_A^4) - \frac{48\,g_A^4 m_\pi^4}{4\,m_\pi^2 + k^2} \right] . \tag{211}$$

In the equation above the loop function G is defined as in Eq. (73), and the renormalization of the Sachs magnetic moment follows that of the potential. From Eq. (205), it is easily seen that the relation in Eq. (210) can be verified by direct evaluation of $(\mathbf{R}/2) \times \mathbf{j}_{\text{loop}}^{\text{N}^3\text{LO}}(\mathbf{q} = 0, \mathbf{k})$. Note that the current of type g) and i)—see Eqs. (153) and (154)—do not contribute to the Sachs magnetic moment, since they vanish at $\mathbf{q} = 0$.

The translationally invariant magnetic moment associated with the loop current at N^{3}LO is obtained from

$$\boldsymbol{\mu}_{\text{T}}^{\text{loop}}(\mathbf{k}) = -\frac{i}{2} \nabla_q \times \mathbf{j}_{\text{loop}}^{\text{N}^3\text{LO}}(\mathbf{q}, \mathbf{k}) \Big|_{\mathbf{q}=0} \; , \tag{212}$$

where $\mathbf{j}_{\text{loop}}^{\text{N}^3\text{LO}}$ is the current given in Eq. (140). The details of the calculation are given in Appendix E, where we find that the translationally invariant magnetic moment due to the one-loop two-body currents is conveniently written as

$$
\begin{aligned}
\boldsymbol{\mu}_{\text{T}}^{\text{loop}}(\mathbf{k}) &= \frac{e\,g_A^2}{8\,\pi^2 F_\pi^4}\,\tau_{2,z}\left[F_0(k)\,\boldsymbol{\sigma}_1 - F_2(k)\,\frac{\mathbf{k}\,\boldsymbol{\sigma}_1\cdot\mathbf{k}}{k^2}\right] \\
&+ \frac{e\,g_A^2}{2\,\pi^2 F_\pi^2}\,\tau_{2,z}\,(C_S\,\boldsymbol{\sigma}_2 - C_T\,\boldsymbol{\sigma}_1) + 1 \rightleftharpoons 2 \;,
\end{aligned}
\tag{213}
$$

where the functions $F_i(k)$ are

$$
\begin{aligned}
F_0(k) &= 1 - 2\,g_A^2 + \frac{8\,g_A^2\,m_\pi^2}{k^2 + 4\,m_\pi^2} \\
&+ G(k)\left[2 - 2\,g_A^2 - \frac{4\,(1 + g_A^2)\,m_\pi^2}{k^2 + 4\,m_\pi^2} + \frac{16\,g_A^2\,m_\pi^4}{(k^2 + 4\,m_\pi^2)^2}\right] \;,
\end{aligned}
\tag{214}
$$

$$
\begin{aligned}
F_2(k) &= 2 - 6\,g_A^2 + \frac{8\,g_A^2\,m_\pi^2}{k^2 + 4\,m_\pi^2} \\
&+ G(k)\left[4\,g_A^2 - \frac{4\,(1 + 3\,g_A^2)\,m_\pi^2}{k^2 + 4\,m_\pi^2} + \frac{16\,g_A^2\,m_\pi^4}{(k^2 + 4\,m_\pi^2)^2}\right] \;.
\end{aligned}
\tag{215}
$$

The magnetic moment $\boldsymbol{\mu}_{\text{T}}^{\text{loop}}$ is expressed in Eq. (213) in terms of two simple operatorial structures. It is interesting to note that the constant $2 - 6\,g_A^2$ in $F_2(k)$ would lead to a long-range contribution of the type $[\tau_{2,z}\,(\boldsymbol{\sigma}_1\cdot\boldsymbol{\nabla})\boldsymbol{\nabla} + 1 \rightleftharpoons 2]\,1/r$ in the magnetic moment, which is, however, fictitious in the present context of an effective field theory valid at low momenta—in performing the Fourier transform, the high momentum components are suppressed by the cutoff $C_\Lambda(k)$.

The total magnetic moment due to $\mathbf{j}_{\text{loop}}^{\text{N}^3\text{LO}}$ is finally given by the expressions in Eqs. (210) and (213). The LECs entering this operator, namely g_A, F_π, C_S, and C_T are known. In particular, C_S, and C_T have been fixed by fitting the N²LO potential as discussed in Sec. III.3.

Currents in χEFT at N³LO have also been derived, using different formalisms, by Park *et al.* in Ref. [4] and, more recently, by Kölling *et al.* in Ref. [45]. The derivation in Ref. [4] is based on covariant perturbation theory and concerns contributions from the one-loop corrections. We find two main differences in the structures of the TPE magnetic moments. The first one is related to the treatment of the 'box' diagrams, panels d) and e) in Fig. 25. In particular, Eqs. (352) and (358) in Appendix E result from combining recoil-corrected reducible and irreducible diagrams, leading to a magnetic moment which involves $\tau_{i,z}$ isospin structures. The operator derived in

Ref. [4] has also a term proportional to $(\boldsymbol{\tau}_1 \times \boldsymbol{\tau}_2)_z$. The latter would have been present also in our operator, had we retained only irreducible diagrams in the evaluation of the currents in panel d) and e) of Fig. 25.

The second difference is that the Sachs term is ignored in Ref. [46]. Of course, it vanishes in two-body systems because of its dependence on $\mathbf{R}$. However, in $A > 2$ systems the center-of-mass position of a nucleon pair will not generally coincide with that of the nucleus, and therefore this term will contribute.

The derivation in Ref. [45] is carried out within the projection formalism of Ref. [3]. The resulting expressions for the TPE currents, the only ones considered by the authors of Ref. [45], are in agreement with those we obtained in this work.

V.2   MAGNETIC MOMENT FROM CONTACT AND TREE-LEVEL CURRENTS

We start off by considering the magnetic moments due to the contact current of minimal nature $\mathbf{j}_{\mathrm{CT},\gamma}^{\mathrm{N^3LO}}$ given in Eq. (124). Again, we can separate the magnetic moment operator into Sachs $\boldsymbol{\mu}_{\mathrm{Sachs}}^{\mathrm{CT}}$ and translationally invariant $\boldsymbol{\mu}_{\mathrm{T}}^{\mathrm{CT,m}}$ terms

$$\boldsymbol{\mu}^{\mathrm{CT,m}} = \boldsymbol{\mu}_{\mathrm{Sachs}}^{\mathrm{CT}} + \boldsymbol{\mu}_{\mathrm{T}}^{\mathrm{CT,m}} . \tag{216}$$

The Sachs moment is given by

$$\boldsymbol{\mu}_{\mathrm{Sachs}}^{\mathrm{CT}}(\mathbf{R}, \mathbf{r}) = -i \frac{\mathbf{R}}{2} \times \int d\mathbf{x}\, \mathbf{x}\, \left[\rho(\mathbf{x}),\, v^{\mathrm{CT2}} + v_{\mathbf{P}}^{\mathrm{CT2}} \right] \tag{217}$$

where the momentum space expressions of the contact potentials v^{CT2} and $v_{\mathbf{P}}^{\mathrm{CT2}}$ are given in Eqs. (42) and (98), respectively. Non vanishing terms of the commutator entering the definition of Sachs moment arise from contributions to the contact potential which depend on the momenta of the two nucleons. Specifically, insertion of the explicit expression of the charge operator ρ into Eq. (217) leads to

$$\begin{aligned} \boldsymbol{\mu}_{\mathrm{Sachs}}^{\mathrm{CT}}(\mathbf{R}, \mathbf{r}) &= -i\, e\, e_{N,1} \frac{\mathbf{R}}{2} \times \left[\mathbf{r}_1,\, v^{\mathrm{CT2}} + v_{\mathbf{P}}^{\mathrm{CT2}} \right] + 1 \rightleftharpoons 2 \\ &= -\frac{i\, e}{2} \left(1 + \frac{\tau_{1,z} + \tau_{2,z}}{2} \right) \mathbf{R} \times \left[\mathbf{R},\, v_{\mathbf{P}}^{\mathrm{CT2}} \right] \\ &\quad - \frac{i\, e}{4} \frac{\tau_{1,z} - \tau_{2,z}}{2} \mathbf{R} \times \left[\mathbf{r},\, v^{\mathrm{CT2}} + v_{\mathbf{P}}^{\mathrm{CT2}} \right] . \end{aligned} \tag{218}$$

The equation above can be verified by evaluating $(\mathbf{R}/2) \times \mathbf{j}_{\mathrm{CT}\gamma}^{\mathrm{N^3LO}}(\mathbf{q} = 0)$, as indicated in Eqs. (203) and (205). The $\mathbf{P}$-dependent contact potential $v_{\mathbf{P}}^{\mathrm{CT2}}$ is expressed in

terms the five LECs C_i^* listed in Eq. (99). This contact contribution to the potential has been identified with boosts corrections to the LO contact potential and, as shown in Eq. (218), is responsible for part of the Sachs magnetic moment. In the first set of calculations presented later in this work, we have neglected contributions due to $v_{\mathbf{P}}^{\mathrm{CT2}}$ ($C_i^* = 0$) and taken $\boldsymbol{\mu}_{\mathrm{Sachs}}^{\mathrm{CT}}$ to be given in momentum space by

$$
\begin{aligned}
\boldsymbol{\mu}_{\mathrm{Sachs}}^{\mathrm{CT}}(\mathbf{R}, \mathbf{k}, \mathbf{K}) \;=\; & \frac{e}{4} \frac{\tau_{1,z} - \tau_{2,z}}{2} \mathbf{R} \times \left[2\left(C_2 + C_4\, \boldsymbol{\sigma}_1 \cdot \boldsymbol{\sigma}_2 \right) \mathbf{K} - i\, C_5\, \frac{\boldsymbol{\sigma}_1 + \boldsymbol{\sigma}_2}{2} \times \mathbf{k} \right. \\
& \left. + \; C_7 \left(\boldsymbol{\sigma}_1\, \boldsymbol{\sigma}_2 \cdot \mathbf{K} + \boldsymbol{\sigma}_1 \cdot \mathbf{K}\, \boldsymbol{\sigma}_2 \right) \right] .
\end{aligned}
\tag{219}
$$

It is determined by C_2, C_4, C_5, and C_7, i.e. by the LECs of the momentum-dependent terms in v^{CT2} which do not commute with the charge operator. These LECs are known from the phase-shifts analysis reported in Sec. III.3.

The translationally invariant component of the magnetic moment is obtained by direct evaluation of Eq. (206) with the contact current given in Eq. (124). Note that only the terms proportional to C_4', C_5', and C_6' of the current $\mathbf{j}_{\mathrm{CT}\gamma}^{\mathrm{N^3LO}}$ contribute to the translationally invariant magnetic moment. Specifically, we find

$$
\boldsymbol{\mu}_{\mathrm{T}}^{\mathrm{CT,m}} = -\frac{e}{2}(C_4' + C_5')\,(\boldsymbol{\sigma}_1 + \boldsymbol{\sigma}_2) ,
\tag{220}
$$

where we have used the relation $C_6' = -C_5'$ implied by $C_1^* = 0$, and have dropped a term proportional to $(\tau_{1,z} + \tau_{2,z})\,(\boldsymbol{\sigma}_1 + \boldsymbol{\sigma}_2)$, since it vanishes when acting on antisymmetric two-nucleons states.

Finally, there is a contribution to the magnetic moment due to the contact current of non-minimal nature, that is $\mathbf{j}_{\mathrm{CT}\gamma,\mathrm{mn}}$ given in Eq. (273). This current is transverse to the photon momentum, therefore the corresponding magnetic moment consists of the translationally invariant contribution only, and is obtained by direct evaluation of Eq. (206),

$$
\boldsymbol{\mu}_{\mathrm{T}}^{\mathrm{CT,nm}} = -e\, C_{15}'\,(\boldsymbol{\sigma}_1 + \boldsymbol{\sigma}_2) - e\, C_{16}'\,(\tau_{1,z} - \tau_{2,z})\,(\boldsymbol{\sigma}_1 - \boldsymbol{\sigma}_2) .
\tag{221}
$$

The translationally invariant term due to minimal and non minimal contact currents is determined by two independent LECs, one of which multiplies an isoscalar structure, while the other multiplies an isovector structure

$$
\boldsymbol{\mu}_{\mathrm{T}}^{\mathrm{CT}} \;=\; \boldsymbol{\mu}_{\mathrm{T}}^{\mathrm{CT,m}} + \boldsymbol{\mu}_{\mathrm{T}}^{\mathrm{CT,nm}} = -e\, D_1^{\mathrm{S}}\,(\boldsymbol{\sigma}_1 + \boldsymbol{\sigma}_2) - e\, D_1^{\mathrm{V}}\,(\tau_{1,z} - \tau_{2,z})\,(\boldsymbol{\sigma}_1 - \boldsymbol{\sigma}_2),
\tag{222}
$$

where $D_1^{\mathrm{S}} = C_{15}' + (C_4' + C_5')/2$, and $D_1^{\mathrm{V}} = C_{16}'$.

The complete expression of the magnetic moment due to the contact currents at N^3LO is given by the Sachs contribution of Eq. (219), plus the translationally invariant terms above. The Sachs term is completely determined by the LECs entering the contact potential at N^2LO, while the translationally invariant term involves two additional unknown LECs.

At N^3LO, there is an additional contribution to the magnetic operator due to the tree-level current $\mathbf{j}^{N^3LO}_{\text{tree}}$ given in Eq. (126). This current generates a translationally invariant moment which reads

$$\boldsymbol{\mu}^{\text{tree}}_{\text{T}} = e\frac{g_A}{F^2_\pi}\left[(d'_8\,\tau_{2,z} + d'_9\,\boldsymbol{\tau}_1\cdot\boldsymbol{\tau}_2)\,\mathbf{k} - d'_{21}\,(\boldsymbol{\tau}_1\times\boldsymbol{\tau}_2)_z\,\boldsymbol{\sigma}_1\times\mathbf{k}\right] \frac{\boldsymbol{\sigma}_2\cdot\mathbf{k}}{k^2 + m^2_\pi} + 1 \rightleftharpoons 2 \ , \ (223)$$

and the determination of the LECs entering the equation above is discussed in Sec. VI.

CHAPTER VI

RESULTS

In this work we derived a nuclear chiral potential up to order Q^2 and consistent electromagnetic currents up to $e\,Q$. The contributions entering the nuclear potential are summarized in Fig. 7. It depends on nine LECs—namely C_S, C_T, and C_i with $i = 1, \ldots, 7$—associated with four-nucleon contact interactions. These LECs have been fixed by fitting np S- and P-wave phase shifts up to 100 MeV energies in the lab frame. The values obtained from the fits are reported in Table 4 for cutoffs Λ in the range 500–700 MeV.

LO

NLO

N²LO(RC)

N³LO

FIG. 37: Diagrams illustrating the electromagnetic currents up to N³LO. Only one among the possible time orderings is shown. Notation as in Fig. 20.

The contributions to the electromagnetic current operator are summarized in Fig. 37. The LO $(e\,Q^{-2})$ term, Eq. (104), results from the coupling of the external photon field to the individual nucleons. It consists of the standard convection and spin-magnetization currents of the nucleon. The NLO term involves seagull, Eq. (106), and in-flight, Eq. (107), contributions associated with OPE. The N²LO term, Eq. (108), represents the $(Q/m_N)^2$ relativistic correction to the LO one-body current. In what follows, we denote this last contribution with N²LO(RC) as indicated in the figure. The LO and N²LO currents have both isoscalar and isovector components, while the OPE currents are purely isovector.

The contributions at N³LO are also shown in Fig. 37, where the last diagram represents contact currents of 'minimal', Eq. (124), and 'non-minimal' nature, Eq. (125), derived in Sec. IV.2.1. The former involve LECs which are related to those entering the nuclear potential, while the latter are expressed in terms of additional LECs

unconstrained by the strong interaction.

The next to last diagram of Fig. 37 represents the tree-level OPE current involving the electromagnetic Hamiltonian $H^{(2)}_{\gamma\pi NN}$ of order $e\,Q^2$ at the vertex indicated by a full circle. The explicit expression for this current is given in Eq. (126), and it involves LECs multiplying both isoscalar and isovector structures. The remaining diagrams represent TPE currents at one loop, discussed in Sec. IV.2.3. These have only isovector components, as can be inferred from their expressions given in Eqs. (130)–(134) and Eqs. (137)–(138).

In what follows, we present calculations of reactions induced by the magnetic moment operator $\boldsymbol{\mu}$ associated with these currents. The LO and N²LO(RC) one-body magnetic moment operators are completely determined by the experimental values of the proton and neutron magnetic moments, respectively +2.793 and –1.913 in units of nuclear magnetons (n.m.). The NLO contribution involves the axial coupling constant g_A, and the pion decay amplitude F_π, for which we adopt the values listed in Table 3.

The two-body magnetic moment operator associated with the N³LO currents has been derived in Chapter V. It has been separated into the Sachs' contribution, which is uniquely determined by the χEFT potential at order Q^2, and a translationally invariant contribution. In particular, the Sachs magnetic moment due to the TPE current, Eq. (210), as well as contact currents of 'minimal' nature, Eq. (219), reads

$$
\begin{aligned}
\boldsymbol{\mu}^{\text{N}^3\text{LO}}_{\text{Sachs}} &= \boldsymbol{\mu}^{\text{loop}}_{\text{Sachs}} + \boldsymbol{\mu}^{\text{CT}}_{\text{Sachs}} \\
&= -\frac{i}{2}\,e\,(\boldsymbol{\tau}_1 \times \boldsymbol{\tau}_2)_z\,\mathbf{R} \times \nabla_k\,\bar{v}^{2\pi}_{\text{I}}(k) + \frac{e}{4}\frac{\tau_{1,z} - \tau_{2,z}}{2}\mathbf{R} \\
&\quad \times\ \left[2\,(C_2 + C_4\,\boldsymbol{\sigma}_1 \cdot \boldsymbol{\sigma}_2)\,\mathbf{K} - i\,C_5\,\frac{\boldsymbol{\sigma}_1 + \boldsymbol{\sigma}_2}{2} \times \mathbf{k} \right. \\
&\quad +\ \left. C_7\,(\boldsymbol{\sigma}_1\,\boldsymbol{\sigma}_2 \cdot \mathbf{K} + \boldsymbol{\sigma}_1 \cdot \mathbf{K}\,\boldsymbol{\sigma}_2)\right]
\end{aligned} \tag{224}
$$

where $\bar{v}^{2\pi}_{\text{I}}(k)$ is the isospin-dependent part of the TPE chiral potential at order Q^2 given in Eq. (211), and C_2, C_4, C_5, and C_7 are LECs entering the contact potential at order Q^2.

Currents at N³LO with pion loops generate a translationally invariant magnetic moment which involves only known LECs, namely g_A, F_π, C_S, and C_T. We report

here its expression

$$
\begin{aligned}
\boldsymbol{\mu}_{\mathrm{T}}^{\mathrm{loop}} &= \frac{e\, g_A^2}{8\,\pi^2 F_\pi^4}\, \tau_{2,z}\Big[F_0(k)\,\boldsymbol{\sigma}_1 - F_2(k)\frac{\mathbf{k}\,\boldsymbol{\sigma}_1\cdot\mathbf{k}}{k^2}\Big] \\
&+ \frac{e\, g_A^2}{2\,\pi^2 F_\pi^2}\, \tau_{2,z}\,(C_S\,\boldsymbol{\sigma}_2 - C_T\,\boldsymbol{\sigma}_1) + 1 \rightleftharpoons 2 \ ,
\end{aligned}
\tag{225}
$$

where the loop function G is defined as in Eq. (73), and F_0 and F_2 are given in Eqs. (214) and (215), respectively. In the remainder of this chapter we denote with N^{3}LO(S-L) the contributions to the magnetic moment operator due to the Sachs term of Eq. (224) and to the transitionally invariant component generated by the one-loop TPE currents of Eq. (225). Note that the N^{3}LO(S-L) operator has only isovector components and involves known LECs.

Unknown LECs enter the translationally invariant component due to the contact currents of 'minimal' and 'non-minimal' nature and to the tree-level current at N^{3}LO. The explicit expressions of the resulting magnetic moment operators due to these currents are given in Eqs. (222) and (223), respectively, and read

$$
\boldsymbol{\mu}_{\mathrm{T}}^{\mathrm{CT}} = -e\, D_1^{\mathrm{S}}\,\boldsymbol{\sigma}_1 - e\, D_1^{\mathrm{V}}(\tau_{1,z} - \tau_{2,z})\,\boldsymbol{\sigma}_1 + 1 \rightleftharpoons 2 \ ,
\tag{226}
$$

$$
\begin{aligned}
\boldsymbol{\mu}_{\mathrm{T}}^{\mathrm{tree}} &= e\frac{g_A}{F_\pi^2}\Big[(d_8'\,\tau_{2,z} + d_9'\,\boldsymbol{\tau}_1\cdot\boldsymbol{\tau}_2)\,\mathbf{k} \\
&- d_{21}'\,(\boldsymbol{\tau}_1\times\boldsymbol{\tau}_2)_z\boldsymbol{\sigma}_1\times\mathbf{k}\Big]\frac{\boldsymbol{\sigma}_2\cdot\mathbf{k}}{k^2 + m_\pi^2} + 1 \rightleftharpoons 2 \ ,
\end{aligned}
\tag{227}
$$

where D_1^S, D_1^V, d_8', d_9', and d_{21}' are the remaining unknown LECs to be determined below. In the following we will refer to the terms in Eqs. (226) and (227) collectively as N^{3}LO(LECs). We also recall that there are no three-body contributions to the magnetic moment operator occurring at N^{3}LO.

In what follows, we present calculations of the magnetic moments of $A = 2$ and 3 nuclei and cross sections for radiative capture reactions in $A = 2$–4 systems. The latter involve matrix elements induced by the magnetic moment operator. We will not derive here the explicit expressions for the cross sections, we will instead extensively refer to the derivations and calculational techniques adopted in Refs. [7, 8, 24].

In the next section, we complete the derivation of the the magnetic moment operator by fixing the LECs entering the N^{3}LO(LECs) contribution. Predictions obtained with the resulting operator are discussed in Sec. VI.2.

VI.1   M1 OBSERVABLES IN $A=2$–4 SYSTEMS: FIXING THE LECS

The calculations presented here are carried out in the hybrid approach, that is by evaluating the matrix elements of the χEFT magnetic moment (M1) operator between nuclear wave functions obtained from realistic potentials. Nuclear wave functions generated from the χEFT potential derived in Chapter III are not available at the moment. It would be certainly interesting to perform fully consistent calculations where both the nuclear interaction and electromagnetic currents are obtained within the same χEFT theoretical framework. Nevertheless, the hybrid approach has been widely exploited to study electroweak reactions in light nuclei [4, 46, 47]. It is unclear at this stage whether the inconsistency between the short-range behavior of the realistic potential and that of the χEFT currents, intrinsic to hybrid calculations, is only a conceptual issue of little numerical importance.

In order to have a realistic estimate of the model dependence of the results, we use wave functions corresponding to two different nuclear Hamiltonians. The wave functions for $A=2$ are derived from solutions of the Schrödinger equation with the Argonne v_{18} (AV18) [11] or chiral N3LO (N3LO) [12] two-nucleon potentials. Both these nuclear models describe the long-range component of the NN interaction via OPE. At intermediate and short distances, the AV18 model parametrizes the radial dependence of the NN interaction in terms of functions of two-pion-range and shorter-range, whose strengths are adjusted to fit the NN data. It fits the np and pp phase-shifts up to ~ 350 MeV with a χ^2 per datum close to 1. The N3LO potential is derived within a χEFT formulation with pions and nucleons up to order Q^4. It involves 24 free parameters (LECs), which are fixed so as to reproduce np and pp scattering phase-shifts up to ~ 290 MeV with a χ^2 per datum also close to 1.

Wave functions for $A=3$ and 4 nuclei are obtained from a Hamiltonian including, in addition to the AV18 or N3LO two-nucleon, also a three-nucleon potential, the Urbana-IX (UIX) [13] or the N2LO (N2LO) [14] model. The former describes the three-nucleon potential in terms of a TPE three-nucleon term involving the excitation of an intermediate Δ-resonance and a short-range term. Their strengths are adjusted to reproduce the triton binding energy and the saturation density of nuclear matter. The N2LO three-nucleon interaction is derived in a χEFT framework and it is expressed in terms of two LECs which are constrained by reproducing the binding energies of $A = 3$ nuclei and triton β decay. The AV18/UIX and N3LO/N2LO Hamiltonians provide an excellent description of three- and four-nucleon bound and

scattering state properties, including binding energies, radii, and effective range expansions [48].

The operators in Eqs. (224)–(227), as well as those at NLO, need to be regularized. We accomplish this by including a cutoff $C_\Lambda(k) = \exp(-k^4/\Lambda^4)$, as discussed in Sec. IV.5, and we study the sensitivity of the results with respect to variations of Λ in the range between 500 MeV and 700 MeV. Thus, $C_\Lambda(k)$ removes momenta k larger than $(3\text{--}4)\, m_\pi$ in a theory retaining up to TPE mechanisms, and whose regime of validity extends, therefore, up to $\sim 2\, m_\pi$.

	μ_d (n.m.)		$\mu_S(^3\mathrm{He}/^3\mathrm{H})$ (n.m.)	
	AV18	N3LO	AV18/UIX	N3LO/N2LO
LO	0.8471	0.8542	0.4104	0.4190
N²LO(RC)	0.8400	0.8471	0.4038	0.4124
EXP	0.8574		0.4257	

TABLE 7: Cumulative LO and N²LO(RC) contributions to the deuteron magnetic moment (isoscalar combination of the trinucleons magnetic moments) obtained with the AV18 (AV18/UIX) and N3LO (N3LO/N2LO) potential models.

We now turn our attention to the determination of the LECs D_1^S, D_1^V, d_8', d_9', and d_{21}' entering the N³LO(LECs) M1 operator. As already discussed in Sec. IV.1, the d_i' could be fitted to pion photoproduction data on a single nucleon or related to hadronic coupling constants by resonance saturation arguments (although $g_{\omega NN}$ and $g_{\rho NN}$ are rather poorly known). This latter procedure is used in a series of hybrid calculations, based on the M1 operators derived in Ref. [4], of the np, nd, and $n\,^3$He radiative captures, and magnetic moments of $A=2$ and 3 nuclei [4, 46]. Here, however, we assume $d_{21}'/d_8' = 1/4$ as suggested by the Δ-resonance saturation mechanism, and rely on nuclear data to constrain the remaining LECs.

With the additional constraint provided by the resonance saturation argument, the number of unknown LECs is reduced to four. Two of these LECs, namely D_1^S and $D_2^S = d_9'$, multiply isoscalar structures, while the remaining two, that is D_1^V and $D_2^V = d_{21}' = d_8'/4$, are related to the isovector component of the N³LO(LECs) M1 operator. We fix these LECs by reproducing the experimental values of two isoscalar observables, *i.e.* the deuteron and the isoscalar combination of the trinucleon M1's, and two isovector observables, *i.e.* the isovector combination of the trinucleon M1's and the np cross section at thermal neutron energies.

Λ	d_1^S	$d_2^S \times 10^2$
500	−3.18 (−2.38)	−8.85 (−0.225)
600	−7.10 (−5.30)	−2.90 (9.20)
700	−13.2 (−9.83)	6.64 (20.4)

TABLE 8: Adimensional values of the isoscalar LECs corresponding to cutoff parameters Λ in the range 500–700 MeV obtained for the AV18/UIX (N3LO/N2LO) Hamiltonian. See text for explanation.

	$\mu_V(^3\text{He}/^3\text{H})$ (n.m.)					
	AV18/UIX			N3LO/N2LO		
Λ (MeV)	500	600	700	500	600	700
LO	−2.159	−2.159	−2.159	−2.194	−2.194	−2.194
NLO	−2.382	−2.413	−2.430	−2.419	−2.436	−2.434
N^{2}LO(RC)	−2.353	−2.384	−2.401	−2.394	−2.408	−2.410
N^{3}LO(S-L)	−2.284	−2.332	−2.377	−2.337	−2.359	−2.375
EXP	−2.553					

TABLE 9: Cumulative LO, NLO, N^{2}LO(RC), N^{3}LO(S-L) contributions to the isovector combination of the trinucleons magnetic moments obtained with the AV18/UIX and N3LO/N2LO potential models.

The deuteron has total isospin $T = 0$, while ^{3}He and ^{3}H are (almost) pure $T = 1/2$ states, with isospin projection $T_z = +1/2$ and $−1/2$, respectively. The isoscalar combination of the trinucleon magnetic moments is defined as

$$\mu^S(^3\text{He}/^3\text{H}) = \frac{1}{2}\left[\mu(^3\text{He}) + \mu(^3\text{H})\right] \ , \tag{228}$$

where $\mu(^3\text{He})$ and $\mu(^3\text{H})$ are the helium and triton M1's. As already mentioned, only the one-body LO and N^{2}LO(RC) M1 operators contribute to isoscalar observables. In Table 7 we list the experimental value of μ_d [$\mu^S(^3\text{He}/^3\text{H})$], along with the cumulative LO and N^{2}LO(RC) contributions obtained with the AV18 and N3LO (AV18/UIX and N3LO/N2LO) nuclear models. In both cases, the N^{2}LO(RC) correction has opposite sign with respect to the LO contribution, so that its inclusion increases the differences between the measured and calculated values. This $(Q/m_N)^2$ corrections

are (in magnitude) about 1% of the LO contributions. These isoscalar observables present a rather weak dependence on the Hamiltonian utilized to generate the nuclear wave functions.

The LECs D_1^S, and D_2^S entering the N³LO(LECs) isoscalar M1 operator are obtained by fitting the experimental values of μ_d, and $\mu^S({}^3\text{He}/{}^3\text{H})$ listed in Table 7. In Table 8 we report the values of these LECs given in units of powers of Λ, *i.e.* we have defined $D_1^S = d_1^S/\Lambda^4$, $d_2^S = D_2^S/\Lambda^2$.

	σ_{np}^γ (mb)					
	AV18			N3LO		
Λ (MeV)	500	600	700	500	600	700
LO	304.6	304.6	304.6	305.8	305.8	305.8
NLO	319.3	320.9	321.8	320.6	321.1	321.2
N²LO(RC)	317.7	319.2	320.1	319.1	319.8	319.8
N³LO(S-L)	314.3	316.6	318.8	316.1	317.2	318.0
EXP	332.6(7)					

TABLE 10: Cumulative LO, NLO, N²LO(RC), N³LO(S-L) contributions to the cross section for the radiative capture of thermal neutron on proton obtained with the AV18/UIX and N3LO/N2LO potential models. The experimental value from Ref. [49].

Next, we consider the isovector observables. The isovector combination of the trinucleon magnetic moments is given by

$$\mu^V({}^3\text{He}/{}^3\text{H}) = \frac{1}{2}\left[\mu({}^3\text{He}) - \mu({}^3\text{H})\right] \ . \tag{229}$$

The cumulative contributions up to N³LO(S-L) correction included are reported in Table 9. We note that also in this case the RC correction at N²LO has opposite sign with respect to the LO contribution. The NLO correction has the same sign as the LO term, while the N³LO(S-L) has opposite sign.

The last isovector observable considered to determine the LECs is the cross section for the radiative capture of thermal neutrons on protons (σ_{np}^γ). At these low energies, the $np \to d\gamma$ reaction occurs entirely through the ${}^1S_0$ scattering state, to allow the colliding proton and neutron to come close enough to be able to fuse. Since the initial scattering state is characterized by isospin $T = 1$ this process occurs via the isovector component of the M1 operator. The Sachs component of the N³LO(S-L)

Λ	d_1^V	d_2^V
500	−11.3 (−11.4)	5.18 (5.82)
600	−12.9 (−23.3)	6.55 (6.85)
700	−1.70 (−46.2)	8.24 (8.27)

TABLE 11: Adimensional values of the isovector LECs corresponding to cutoff parameters Λ in the range 500–700 MeV obtained for the AV18/UIX (N3LO/N2LO) Hamiltonian. See text for explanation.

M1 operator does not contribute to the np cross section, since it vanishes in $A = 2$ systems.

The cross section associated to this process is given by [24]

$$\sigma_{np}^\gamma = (4\pi)^2\,\sigma_0\,\mid M_1(^1S_0)\mid^2\;, \tag{230}$$

where σ_0 is defined as

$$\sigma_0 = \frac{\alpha}{2\,\pi\,v}\frac{q}{1+q/m_d}\;. \tag{231}$$

Here α is the fine-structure constant, m_d is the deuteron mass and v is the np relative velocity. In Table 10 we list the cumulative contributions to the np cross section. The largest contribution to the cross section is given by the LO term. The OPE M1 contribution at NLO has the same sign as the LO one, while both the N^2LO(RC) and N^3LO(S-L) have opposite sign.

The LECs D_1^V and D_2^V are obtained by reproducing the experimental σ_{np}^γ and $\mu^V(^3\text{He}/^3\text{H})$ given in Tables 9 and 10. The values obtained from this fit are listed in Table 11, where again we have defined $D_1^V = d_1^V/\Lambda^4$ and $D_2^V = d_2^V/\Lambda^2$.

The analysis reported in this section is summarized in Fig. 38 where we show results obtained by including cumulatively the contributions at LO, NLO, N^2LO(RC), and N^3LO(S-L) for μ_d and $\mu^S(^3\text{He}/^3\text{H})$ (left panels), and for σ_{np}^γ and $\mu^V(^3\text{He}/^3\text{H})$ (right panels). The band represents the spread in the calculated values corresponding to the two Hamiltonian models considered here (AV18/UIX and N3LO/N2LO). The sensitivity to short-range mechanisms (effective at internucleon separations less than $\sim (2\,m_\pi)^{-1}$) as encoded in the cutoff $C_\Lambda(k)$ and in the rather different short-range behaviors of the adopted potentials, remains quite weak for all observables. Of course, taking into account the N^3LO(LECs) contribution with the LEC values listed
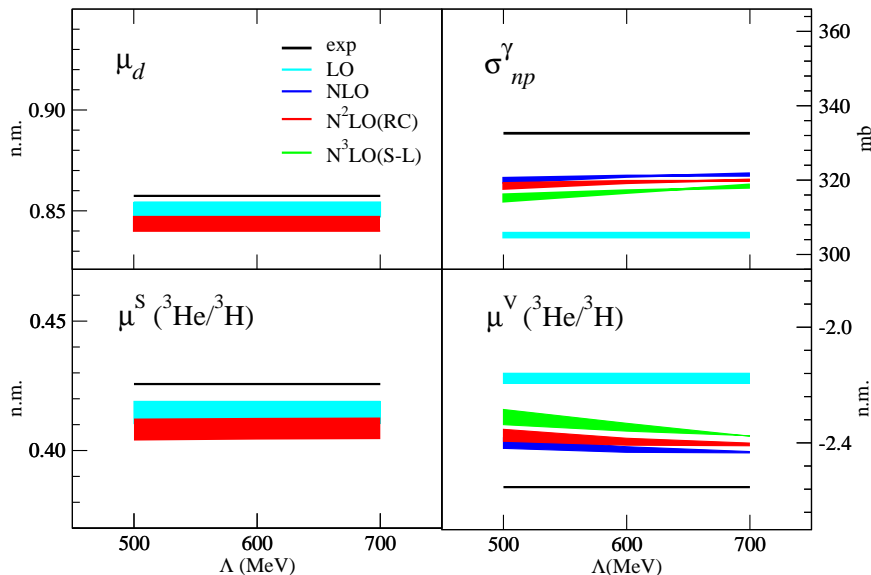
FIG. 38: Results for the deuteron and trinucleon isoscalar and isovector magnetic moments, and np radiative capture, obtained by including cumulatively the LO, NLO, N^{2}LO, and N^{3}LO(S-L) contributions. See text for discussion.

in Tables 8 and 11 reproduces the experimental data represented by the black band (to accommodate errors, although these are negligible in the present case). We observed that, the dominant contribution to the calculated M1's and np cross section is provided by the LO M1 term.

VI.2 RADIATIVE CAPTURES ON DEUTERON AND ^{3}HE

Neutron and proton radiative captures on ^{2}H, ^{3}H and ^{3}He are particularly challenging from the standpoint of nuclear few-body theory. This can be appreciated by comparing the measured values for the cross sections of thermal neutron radiative capture on ^{1}H, ^{2}H, ^{3}He. Their respective values in mb are: (332.6 ± 0.7) [49], (0.508 ± 0.015) [50], and (0.055 ± 0.003) [51]. Thus, in going from A=2 to 4 the cross section has dropped by almost four orders of magnitude. As discussed in the previous section, these processes are induced by $M1$ transitions between the initial two-cluster state in relative S-wave and the final bound state. The ^{3}H and ^{4}He wave functions, respectively Ψ_3 and Ψ_4, are approximately eigenfunctions of the LO one-body $M1$ operator $\boldsymbol{\mu}^{\rm LO}$,

namely $\mu_z^{\mathrm{LO}} \Psi_3 \simeq \mu_p \Psi_3$ and $\mu_z^{\mathrm{LO}} \Psi_4 \simeq 0$, where μ_p=2.793 n.m. is the proton magnetic moment—the experimental value of the ^{3}H magnetic moment is 2.979 n.m, while ^{4}He has no magnetic moment. These relations would be exact, if the ^{3}H and ^{4}He wave functions were to consist of the symmetric S-wave term only. In fact, tensor components in the nuclear potentials generate significant D-state admixtures, that partially spoil this eigenstate property. To the extent that it is approximately satisfied, though, the matrix elements $\langle \Psi_3 | \mu_z^{\mathrm{LO}} | \Psi_{1+2} \rangle$ and $\langle \Psi_4 | \mu_z^{\mathrm{LO}} | \Psi_{1+3} \rangle$ vanish due to orthogonality between the initial and final states. This orthogonality argument fails in the case of the deuteron, since then $\mu_z^{\mathrm{LO}} \Psi_2 \simeq (\mu_p - \mu_n) \, \phi_2(S) \, \chi_0^0 \, \eta_0^1$, where $\chi_{M_S}^S$ and $\eta_{M_T}^T$ are two-nucleon spin and isospin states, respectively. The $M1$ operator can therefore connect the large S-wave component $\phi_2(\mathrm{S})$ of the deuteron to the T=1 ^{1}S$_0$ n-p scattering state—the orthogonality between the latter and the deuteron follows from the orthogonality between their respective spin-isospin states.

This suppression at LO has two main consequences. The first is that the n-d, p-d, n-^{3}He, and p-^{3}H radiative (as well as p-^{3}He weak) captures are very sensitive to small components in the wave functions, particularly the D-state admixtures generated by tensor forces. The second consequence is that these observables are sensitive to many-body terms in the electromagnetic (and weak) current operator.

There have been in the past several calculations of these processes in the conventional framework—referred to as the standard nuclear physics approach (SNPA)—see [10] and references therein. In the recent study of Ref. [9], the electromagnetic current operator includes, in addition to the standard convection and spin-magnetization terms of individual protons and neutrons, also two- and three-body terms, constructed from, respectively, the two- and three-nucleon potentials so as to satisfy exactly current conservation with them. The method by which this is achieved has been improved over the years [52], and its latest implementation is discussed at length in Ref. [9]. It is not unique, since the continuity equation relation puts no constraints on the transverse component of the current. Nevertheless, it does generate two- and three-body terms, whose behavior, particularly at short range, is consistent with that of the corresponding potentials. This behavior in the latter is ultimately "determined" by reproducing a set of experimental two- and three-nucleon scattering data and binding energies.

The SNPA currents have been shown to provide a very satisfactory description of a wide variety of electronuclear properties [7, 8, 9, 53, 54]. Indeed, we show below

a set of up-to-date predictions for the observables of interest here.

Having fully constrained the χEFT $M1$ operator derived in the present work up to N^{3}LO, we are now in a position to present predictions for the nd and $n\,^3$He radiative capture cross sections, denoted as σ_{nd}^{γ} and $\sigma_{n\,^3\mathrm{He}}^{\gamma}$, and the photon circular polarization parameter R_c resulting from the capture of polarized neutrons on deuterons.

	σ_{nd}^{γ} (mb)			R_c		
	AV18/UIX					
Λ (MeV)	500	600	700	500	600	700
LO	0.225	0.225	0.225	−0.087	−0.087	−0.087
NLO	0.343	0.369	0.385	−0.372	−0.398	−0.410
N^{2}LO(RC)	0.314	0.339	0.353	−0.334	−0.365	−0.381
N^{3}LO(S-L)	0.265	0.298	0.334	−0.241	−0.309	−0.360
N^{3}LO(LECs)	0.505	0.507	0.508	−0.468	−0.467	−0.467
EXP	0.508±0.015			-0.42± 0.03		

TABLE 12: Cumulative contributions to the cross section σ_{nd}^{γ} and photon polarization parameter R_c of the reaction ^{2}H$(n,\gamma)^3$H at thermal energies, obtained with the AV18/UIX Hamiltonian model and cutoff values in the range 500-700 MeV. The experimental values for σ_{nd}^{γ} and R_c are from Ref. [50] and Ref. [55], respectively.

The ^{2}H$(n,\gamma)^3$H reaction at thermal energies proceeds through S-wave capture predominantly via M1 transitions from the initial doublet $^2S_{1/2}$ and quartet $^4S_{3/2}$ n-d scattering states to the final $J^\pi = (1/2)^+$ state. In addition, there is a small contribution due to an electric quadrupole transition from the initial quartet state. We adopt here the notation and conventions of Ref. [8] and define

$$m_{22} = \widetilde{M}_1^{0\ 1/2\ 1/2} \ , \qquad m_{44} = \widetilde{M}_1^{0\ 3/2\ 3/2} \ , \qquad e_{44} = \widetilde{E}_2^{0\ 3/2\ 3/2} \ , \qquad (232)$$

where $\widetilde{M}_\ell^{LSJ}$ and $\widetilde{E}_\ell^{LSJ}$ are the reduced matrix elements (RME's) of the magnetic and electric multipole operators of order ℓ, normalized as in Eq. (6.3) of Ref. [8]. In terms of these RME's, the capture total cross section is given by

$$\sigma_{nd}^{\gamma} = \frac{2}{9} \frac{\alpha}{v_{\mathrm{rel}}} \frac{q^3}{4\,m_N^2} \left(|m_{22}|^2 + |m_{44}|^2 + |e_{44}|^2 \right) \ , \qquad (233)$$

where $\alpha = e^2/(4\pi)$ is the fine structure constant, v_{rel} is the d-n relative velocity, q is the energy of the emitted γ ray, and m_N is the nucleon mass. Similarly, the circular polarization P_Γ resulting from S-wave capture of a neutron polarized along

the direction $\mathbf{P}_n$ is proportional to the parameter R_c [8], *i.e.* $P_\Gamma = R_c\,\mathbf{P}_n \cdot \hat{\mathbf{q}}$, where

$$R_c = -\frac{1}{3}\left[1 \quad - \quad \frac{(7/2)|m_{44}|^2 + \sqrt{8}\,\mathrm{Re}(m_{22}m_{44}^*)}{|m_{22}|^2 + |m_{44}|^2 + |e_{44}|^2}\right.$$
$$\left. + \quad \frac{(5/2)|e_{44}|^2 + \sqrt{24}\,\mathrm{Im}(m_{22}e_{44}^*) - \sqrt{3}\,\mathrm{Im}(m_{44}e_{44}^*)}{|m_{22}|^2 + |m_{44}|^2 + |e_{44}|^2}\right]. \quad (234)$$

In Table 12 we list the cumulative contributions to the nd cross section and the R_c parameter obtained with the AV18/UIX nuclear model only. As we have already mentioned, this reaction is dominated by many-body components in the current operator. This trend is confirmed here, in fact the LO contribution to the total cross section is only about $\sim 44\%$ of the measured value. The NLO correction adds up to the LO contribution, while the $N^2LO(RC)$ and $N^3LO(S\text{-}L)$ corrections have opposite sign. We also note that the $N^3LO(LECs)$ correction is of the same order as the correction occurring at NLO. The calculated cross section is in excellent agreement with the experimental data and shows a negligible cutoff dependence. The R_c parameter is 10% larger (in magnitude) than the experimental value.

	$\sigma^\gamma_{n^3\mathrm{He}}$ (μb)					
	AV18/UIX			N3LO/N2LO		
Λ (MeV)	500	600	700	500	600	700
LO	15.2	15.2	15.2	10.6	10.6	10.6
NLO	3.13	9.43	14.5	5.95	10.2	11.5
$N^2LO(RC)$	0.65	2.03	4.38	0.91	2.87	3.56
$N^3LO(S\text{-}L)$	7.56	1.11	1.95	1.36	0.04	0.38
$N^3LO(LECs)$	44.4	46.0	47.6	48.3	52.9	56.6
EXP	55 ± 3					

TABLE 13: Cumulative contributions to the cross section $\sigma^\gamma_{n^3\mathrm{He}}$ of the reaction $^3\mathrm{He}(n,\gamma)^4\mathrm{H}$ at thermal energies, obtained with the AV18/UIX and N3LO/N2LO Hamiltonian models and cutoff values in the range 500-700 MeV. The experimental values for $\sigma^\gamma_{n^3\mathrm{He}}$ is from [51].

The $n\,^3\mathrm{He}\rightarrow{}^4\mathrm{He}\ \gamma$ process involves a transition from an initial n-$^3\mathrm{He}$ $^3S_1$ scattering state to the final $J^\pi = 0^+$ $^4\mathrm{He}$ ground state, and therefore is purely M1. In Table 13 we show the cumulative contributions to the cross section obtained with the AV18/UIX and N3LO/N2LO models. The LO contribution provides only $\sim 18\%$ of the calculated cross section. We note that the matrix element at NLO is of opposite sign and twice as large (in magnitude) compared to that at LO, hence $\sigma^\gamma_{n\,^3\mathrm{He}}(LO)$

and $\sigma^\gamma_{n\,^3\mathrm{He}}(\mathrm{LO} + \mathrm{NLO})$ are about the same. The N²LO and N³LO(S-L) corrections exhibit the same pattern discussed for the nd cross section. Due to the significant suppression at LO, the contributions at LO, NLO and N³LO(LECs) are of the same order.

The discussion above is summarized in Fig. 39 where we show the predictions obtained with the χEFT M1 operator derived in the present work. The experimental data (black bands) are from Ref. [50] for nd and Ref. [51] for $n\,^3\mathrm{He}$. In the right panel, the band represents the spread in the calculated values corresponding to the AV18/UIX and N3LO/N2LO models. Results obtained with the complete N³LO operator are shown by the orange band labeled N³LO(LECs), and are in very satisfactory agreement with data. Their sensitivity to the cutoff is negligible ($\sim 10\%$) for the nd ($n\,^3\mathrm{He}$) capture. These processes are strongly suppressed at LO: the calculated $\sigma^\gamma_{nd}(\mathrm{LO})$ and $\sigma^\gamma_{n\,^3\mathrm{He}}(\mathrm{LO})$ are less than half and a factor of five smaller than the measured values. For both nd and $n\,^3\mathrm{He}$, the N²LO and N³LO(S-L) corrections exhibit the same pattern discussed in connection with Fig. 38. The N³LO(LECs) contributions are large and crucially important for bringing theory into agreement with experiment.

In Fig. 39 we also show results obtained in the conventional SNPA with the AV18/UIX Hamiltonian model. In the left panel of Fig. 39 we indicate with the green squared labeled SNPA the calculated $^2\mathrm{H}(n,\gamma)^3\mathrm{H}$ cross section obtained in Ref. [9]. The pink square labeled SNPA(RC) denotes the result obtained by including the RC to the LO one-body current operator (*i.e.*, the χEFT N²LO operator). This contribution had been neglected in all previous SNPA studies of electronuclear properties. The SNPA(RC) result is in agreement with the experimental data (and the χEFT predictions). In the right panel of Fig. 39 the green square indicates the calculated $^3\mathrm{He}(n,\gamma)^4\mathrm{He}$ cross section obtained with the latest generation of nuclear wave functions and the currents of Refs. [7, 8, 9]. With these new set of wave functions, the SNPA formulation overpredicts the experimental cross section by $\sim 14\%$ (as opposed to $\sim 60\%$ as found in [7]). The addition of the RC correction leads to the result labeled SNPA(RC), which is 25% smaller relative to the experimental data.

Song *et al.* (2009) [46] and Lazauskas *et al.* [46] have reported values for the nd and $n\,^3\mathrm{He}$ capture cross sections about 6% and 15% smaller than measured, with a significantly larger sensitivity (estimated at $\simeq 15\%$ for both processes) to the cutoff. These calculations are based on the M1 operator derived in [4], which differs from

the N^{3}LO M1 operator constructed here (see discussion in Sec. V.1). Furthermore, these authors rely on the resonance saturation to constrain the LECs entering the $\boldsymbol{\mu}_{\text{tree}}^{\text{N}^3\text{LO}}$.
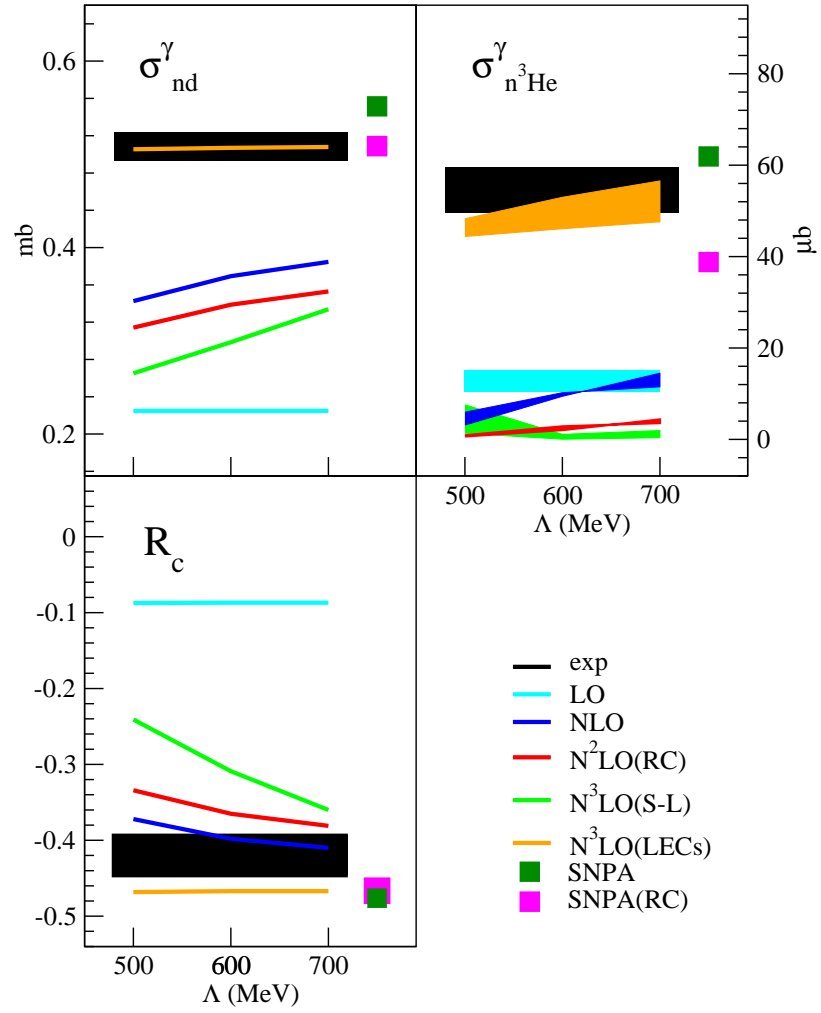
FIG. 39: Results for σ_{nd}^{γ} (left top panel), $\sigma_{n\,^3\mathrm{He}}^{\gamma}$ (right top panel), and R_c (left bottom panel), obtained by including cumulatively the LO, NLO, N²LO, N³LO(S-L), and N³LO(LECs) contributions. Also shown are predictions obtained in the standard nuclear physics approach (squares labeled SNPA and SNPA(RC)). See text for discussion.

CHAPTER VII

SUMMARY AND CONCLUSIONS

In this thesis we have derived a two-body nuclear potential and consistent two-body electromagnetic currents in a χEFT framework, in which pions and nucleons are retained as explicit degrees of freedom. The potential includes up to order Q^2 (N^{2}LO) terms in the chiral expansion. At LO, it consists of OPEP plus a contact term which depends on two LECs, and at N^{2}LO, it is described in terms of TPE and contact interactions. The latter involve seven additional LECs. The LECs at LO and N^{2}LO have been fixed by fitting the np S- and P-wave phase shifts up to 100 MeV energies in the lab frame. The Hamiltonians involving two gradients acting on the nucleons' field generate contributions which depend on the center-of-mass momentum of the two nucleons. These terms represent boost corrections to the LO contact potential [40]. They vanish in two-body systems, however, they must be taken into account in χEFT calculations of nuclei with mass number $A > 2$.

The current operator has been derived up to order $e\,Q$ (N^{3}LO). The LO contribution is given by the one-body operator originating from the convection and spin magnetization terms of the individual nucleons. The first correction to this picture, in which the external photon interacts individually with the nucleus' constituents, is represented by the OPE currents. The N^{2}LO contribution consists of a relativistic correction to the (one-body) LO current. Some of the N^{3}LO contributions are generated by TPE and loop corrections to the (tree-level) OPE currents. The remaining ones arise from a tree-level current involving a 'non-minimal' electromagnetic interaction Hamiltonian of order $e\,Q^2$, and contact currents of 'minimal' and 'non-minimal' nature. The N^{3}LO electromagnetic current operator involve LECs which have been constrained by fits to the phase shifts, and additional LECs have been determined by reproducing electromagnetic observables as specified below.

The derivation of the potential and currents has been carried out in TOPT with the additional prescription of including recoil-corrected reducible contributions along with the irreducible ones. This method leads to N^{3}LO currents which satisfy the continuity with the N^{2}LO chiral potential. We have also shown that there are no three-nucleon potentials entering at N^{2}LO, as well as no three-body electromagnetic currents at N^{3}LO. Several aspects of the derivation have been discussed in detail,

including a comparison with previous derivations using different formalisms. In particular, we have found that the formalism defined in the present work and the unitary transformation method utilized by Epelbaum *et al.* [3] and Koelling *et al.* [45] lead to results which are in agreement with each other. The TPE currents have also been derived in covariant perturbation theory by Park and collaborators in Ref. [4]. The authors retained only irreducible contributions in the evaluation of the transition amplitude, and their results are different from those obtained in this work.

The N^3LO electromagnetic current operator has been utilized to study low-energy electromagnetic transitions induced by the magnetic dipole (M1) operator. The matrix elements of the M1 operator have been evaluated by using accurate wave functions obtained from the AV18/UIX [11, 13] or N3LO/N2LO [12, 14] realistic Hamiltonian models. The M1 operators have been regularized via a momentum cutoff Λ and the sensitivity of the calculated observables with respect to variations of Λ in the range of 500–700 MeV has been analyzed. We have considered the M1's of $A = 2$ and 3 nuclei, and the cross sections for the radiative capture of thermal neutrons on p, d, and ^{3}He. The experimental values for the M1's and cross section of the ^{1}H$(n,\gamma)^2$H reaction have been utilized to completely constraint the M1 operator at N^3LO. The latter involves LECs which, as mentioned before, are not determined by the fits of the chiral potential to the *NN* scattering data. Predictions obtained with this (fully constrained) M1 operator for the ^{2}H$(n,\gamma)^3$H cross section are in excellent agreement with the experimental data, and show a negligible cutoff dependence. The ^{3}He$(n,\gamma)^4$He cross section exhibits a $\sim 5\%$ ($\sim 15\%$) variation with the AV18/UIX (N3LO/N2LO) model, as the cutoff is varied from 500 to 700 MeV, but it is still in good agreement with the experimental datum. These processes are highly suppressed at LO, in particular, the calculated ^{2}H$(n,\gamma)^3$H and ^{3}He$(n,\gamma)^4$He cross sections provide only about $\sim 44\%$ and $\sim 18\%$ of the measured values. The contributions at N^3LO are found to be large, and indeed the contact currents are crucial for reproducing the experimental data.

We have compared the results obtained with the chiral M1 operator with those obtained with the SNPA currents used in Refs. [7, 8, 9]. The SNPA current operator includes, in addition to the one-body term also present in the chiral current at LO, also two- and three-body current constructed so as to satisfy the continuity equation with the AV18 two- and UIX three-nucleon potentials, respectively. The ^{2}H$(n,\gamma)^3$H cross section obtained with the SNPA currents overpredicts the experimental data

by $\sim 10\%$, and the inclusion of the relativistic correction to the one-body current operator (*i.e.* the N^{2}LO current), brings the SNPA prediction in agreement with the experimental data. The cross section of the ^{3}He$(n,\gamma)^4$He reaction calculated with the SNPA currents (SNAP currents plus N^{2}LO relativistic correction) overpredicts (underpredicts) the experimental data by $\sim 10\%$ ($\sim 25\%$). This relativistic correction had been neglected in previous SNPA studies of radiative captures. Due to the suppression of the leading one-body contribution, it plays an important role in these observables.

The work presented in this thesis is the first stage of a research program aimed at studying the electromagnetic properties of light nuclei within a χEFT framework. The chiral current operator provides a very good description of the electromagnetic observables we have considered so far. Charge radii, and magnetic and charge form factors of nuclei at low values of the momentum transfer can also be studied within the formalism developed here. To this end, we are currently in the process of completing the derivation of the chiral charge operator.

Another interesting line of research would involve the explicit inclusion of Δ-isobars degree of freedom in the theory. We have already made some progress on this project: formal expressions of the chiral currents at N^{3}LO with explicit Δ-isobars have been derived in Ref. [42]. However, completion of this program requires one to also construct the two- and three-body potential in the same framework, as well as three-body currents, which would now enter at N^{3}LO.

Finally, in order to investigate weak transitions in nuclei, such as β-decays and electron-capture rates, weak current operators need to be derived. The weak (axial) current has been constructed in Ref. [5] in covariant perturbation theory, neglecting recoil corrections. However, in view of the differences discussed in connection to the electromagnetic current operator, it would be interesting to perform the calculation in the TOPT framework developed here.

BIBLIOGRAPHY

[1] S. Weinberg, Phys. Lett. **B251**, 288 (1990); Nucl. Phys. **B363**, 3 (1991); Phys. Lett. **B295**, 114 (1992).

[2] U. van Kolck, Phys. Rev. C **49**, 2932 (1994); C. Ordónez, L. Ray, and U. van Kolck, Phys. Rev. C **53**, 2086 (1996).

[3] E. Epelbaum, W. Glöckle, and U.-G. Meissner, Nucl. Phys. **A637**, 107 (1998); Nucl. Phys. **A671**, 295 (2000); Nucl. Phys. **A747**, 362 (2005).

[4] T.-S. Park, D.-P. Min, and M. Rho, Nucl. Phys. **A596**, 515 (1996).

[5] T.-S. Park, D.-P. Min, and M. Rho, Phys. Rept. **233**, 341 (1993).

[6] N. Fettes, U.-G. Meissner, and S. Steininger, Nucl. Phys. **A640**, 199 (1998).

[7] R. Schiavilla, R.B. Wiringa, J. Carlson, and V.R. Pandharipande, Phys. Rev. C **45**, 2628 (1992).

[8] M. Viviani, R. Schiavilla, and A. Kievsky, Phys. Rev. C **54**, 534 (1996).

[9] L.E. Marcucci *et al.*, Phys. Rev. C **72**, 014001 (2005).

[10] J. Carlson and R. Schiavilla, Rev. Mod. Phys. **70**, 743 (1998).

[11] R.B. Wiringa, V.G.J. Stoks, and R. Schiavilla, Phys. Rev. C **51**, 38 (1995).

[12] D.R. Entem and R. Machleidt, Phys. Rev. C **66**, 014002 (2002); Phys. Rev. C **68**, 041001 (2003).

[13] B.S. Pudliner *et al.*, Phys. Rev. C **56** 1720 (1997).

[14] D. Gazit, S. Quaglioni, and P. Navratil, Phys. Rev. Lett. **103**, 102502 (2009).

[15] M. Viviani *et al.*, in preparation

[16] S. S. Schweber, *An Introduction to Relativistic Quantum Field Theory* (Dover Publications, 1961).

[17] S. Weinberg, *The Quantum Theory of Fields*, vol. I (Cambridge University Press, 1995).

[18] M. E. Peskin, D. V. Schroeder, *An introduction to Quantum Field Theory* (Westview Press, 1995).

[19] F. Gross, *Relativistic Quantum Mechanics and Field Theory* (John Wiley & Sons, Inc., 1993).

[20] M. Veltman, *Diagrammatica* (Cambridge University Press, Cambridge, 1994).

[21] S. Pastore, L. Girlanda, R. Schiavilla, M. Viviani, and R.B. Wiringa, Phys. Rev. C **80**, 034004 (2009).

[22] M. Fierz, Z. Phys. **104**, 553 (1937).

[23] F. Gross and A. Stadler, Phys. Rev. C **78**, 014005 (2008).

[24] R. Schiavilla, J. Carlson, and M. Paris, Phys. Rev. C **70**, 044007 (2004).

[25] E. Epelbaum, W. Glöckle, and U.-G. Meissner, Nucl. Phys. **A671**, 295 (2000); Eur. Phys. J. **A19**, 125 (2004); Eur. Phys. J. **A19**, 401 (2004).

[26] W. Glöckle, *The Quantum Mechanical Few-Body Problem* (Springer-Verlag, Berlin, 1983).

[27] V.G.J. Stoks, R.G.E. Timmermans, J.J. de Swart, Phys. Rev. C **47**, 512 (1993).

[28] R.A. Arndt, R.L. Workman, and M.M. Pavan, Phys. Rev. C **49**, 2729 (1994).

[29] N. Kaiser, R. Brockmann, and W. Weise, Nucl. Phys. **A625**, 758 (1997).

[30] C.-J. Yang, Ch. Elster, and D.R. Phillips, arXiv:0901.2663; arXiv:0905.4943.

[31] N. Kaiser, S. Gerstendoerfer, W. Weise, Nucl. Phys. **A637**, 395 (1998).

[32] L. Koester and W. Nistler, Z. Phys. A **272**, 189 (1975).

[33] C. van der Leun and C. Alderliesten, Nucl. Phys. **A380**, 261 (1982).

[34] N.L. Rodning and L.D. Knutson, Phys. Rev. C **41**, 898 (1990).

[35] P.J. Mohr and B.N. Taylor, Rev. Mod. Phys. **77**, 1 (2005).

[36] D.M. Bishop and L.M. Cheung, Phys. Rev. A **20**, 381 (1979).

[37] R.A. Krajcik and L.L. Foldy, Phys. Rev. D **10**, 1777 (1974).

[38] J.L. Friar, Phys. Rev. C **12**, 695 (1975).

[39] J. Carlson, V.R. Pandharipande, and R. Schiavilla, Phys. Rev. C **47**, 484 (1993); J.L. Forest, V.R. Pandharipande, and J.L. Friar, Phys. Rev. C **52**, 568 (1995); J.L. Forest, V.R. Pandharipande, J. Carlson, and R. Schiavilla, Phys. Rev. C **52**, 576 (1995).

[40] L. Girlanda, S. Pastore, R. Schiavilla, and M. Viviani, Phys. Rev. C **81**, 034005 (2010).

[41] H. Witala, J. Golak, R. Skibiński, W. Glöckle, W.N. Polyzou, and H. Kamada, Phys. Rev. C **77**, 034004 (2008).

[42] S. Pastore, R. Schiavilla, and J.L. Goity, Phys. Rev. C **78**, 064002 (2008).

[43] R.H. Dalitz, Phys. Rev. **95**, 799 (1954).

[44] R.G. Sachs, Phys. Rev. **74**, 433 (1948).

[45] S. Kölling, E. Epelbaum, H. Krebs, U.-G. Meissner, Phys. Rev. **C80**, 045502 (2009).

[46] T.-S. Park, K. Kubodera, D.-P. Min, and M. Rho, Phys. Lett. **B472**, 232 (2000); Y.-H. Song, R. Lazauskas, T.-S. Park, and D.-P. Min, Phys. Lett. **B656**,174 (2007); Y.-H. Song, R. Lazauskas, and T.-S. Park, Phys. Rev. **C79**, 064002 (2009); R. Lazauskas, Y.-H. Song, and T.-S. Park, arXiv:0905.3119.

[47] T.-S. Park *et al.*, Phys. Rev. **C67**, 055206 (2003).

[48] A. Kievsky *et al.*, J. Phys. **G35**, 063101 (2008).

[49] S.F. Mughabghab, M. Divadeenam, and N.E. Holden, *Neutron Cross Sections from Neutron Resonance Parameters and Thermal Cross Sections* (Academic Press, London, 1981).

[50] E.T. Jurney, P.J. Bendt, and J.C. Browne, Phys. Rev. **C25**, 2810 (1982).

[51] F.L.H. Wolfs, S.J. Freedman, J.E. Nelson, M.S. Dewey, and G.L. Greene, Phys. Rev. Lett. **63**, 2721 (1989); R. Wervelman, K. Abrahams, H. Postma, J.G.L. Booten, and A.G.M. Van Hees, Nucl. Phys. **A526**, 265 (1991).

[52] D.O. Riska, Phys. Scr. **31**, 471(1985); R. Schiavilla, V.R. Pandharipande, and D.O. Riska, Phys. Rev. C **40**, 2294 (1989); J. Carlson, D.O. Riska, R. Schiavilla, and R.B. Wiringa, Phys. Rev. C **42**, 830 (1990).

[53] R. Schiavilla, Phys. Rev. C **72**, 034001 (2005).

[54] L.E. Marcucci, M. Pervin, S.C. Pieper, R. Schiavilla, and R.B. Wiringa, submitted to Phys. Rev. C, arXiv:0810.0547.

[55] M.W. Konijnenberg *et al.*, Phys. Lett. **B205**, 215 (1988).

[56] J.D. Bjorken and S.D. Drell, *Relativistic Quantum Mechanics* (McGraw-Hill, Inc., 1964).

[57] J.C. Collins, *Renormalization. An Introduction to Renormalization, the Renormalization Group, and the Operator-Product Expansion* (Cambridge University Press, Cambridge, 1984); H. Leutwyler, Ann. Phys. 235, 165 (1994); H. Georgi, Ann. Rev. Nucl. Part. Sci. 43, 209 (1993).

[58] Th.A. Rijken and V.G.J. Stoks, Phys. Rev. **46**, 73 (1992).

[59] I. S. Gradshteyn, I. M. Ryzhik, *Table of Integrals, Series, and Products* (Alan Jeffrey, Editor - Academic Press, 1994)

APPENDIX A

INTERACTION HAMILTONIANS

In this appendix we list the explicit expressions of the nuclear and electromagnetic Hamiltonians involved in the calculation of the nuclear potential and electromagnetic current operators. The notation utilized in this appendix has been defined Sec. II.1.

A.1 PION AND NUCLEON INTERACTION HAMILTONIANS

The interaction Hamiltonians involving nucleon and pion fields are derived from the effective chiral Lagrangian approach formulated in Refs. [1, 2]. The Hamiltonians implied by the πNN, and $\pi\pi NN$ χEFT Lagrangians read

$$H_{\pi NN} = \frac{g_A}{F_\pi} \int d\mathbf{x}\, N^\dagger(\mathbf{x})\, [\boldsymbol{\sigma} \cdot \nabla \pi_a(\mathbf{x})]\, \tau_a\, N(\mathbf{x})\ , \tag{235}$$

$$H_{\pi\pi NN} = \frac{1}{F_\pi^2} \int d\mathbf{x}\, N^\dagger(\mathbf{x})\, [\boldsymbol{\pi}(\mathbf{x}) \times \boldsymbol{\Pi}(\mathbf{x})] \cdot \boldsymbol{\tau}\, N(\mathbf{x})\ , \tag{236}$$

where σ_a and τ_a are the spin and isospin Pauli matrices.

The four-fermion contact interaction of order Q^0 is expressed in terms of the two LECs C_S, and C_T,

$$H_{\rm CT0} = \sum_{\alpha=S,T} \frac{C_\alpha}{2} \int d\mathbf{x}\, \left[N^\dagger(\mathbf{x})\, \boldsymbol{\Gamma}_\alpha\, N(\mathbf{x})\right] \cdot \left[N^\dagger(\mathbf{x})\boldsymbol{\Gamma}_\alpha N(\mathbf{x})\right]\ , \tag{237}$$

where we have defined

$$\boldsymbol{\Gamma}_S = 1\ , \quad \boldsymbol{\Gamma}_T = \boldsymbol{\sigma}\ . \tag{238}$$

The last set of interaction Hamiltonians consists of four-nucleon contact terms involving two gradients acting on the nucleons' fields [2, 3]:

$$H_{\rm CT2,1} = C_1' \int d\mathbf{x}\, \left[\left[N^\dagger \nabla N\right]^2 + \left[(\nabla N)^\dagger N\right]^2\right]\ , \tag{239}$$

$$H_{\rm CT2,2} = C_2' \int d\mathbf{x}\, \left[N^\dagger \nabla N\right] \cdot \left[(\nabla N)^\dagger N\right]\ , \tag{240}$$

$$H_{\rm CT2,3} = C_3' \int d\mathbf{x}\, \left[N^\dagger N\right] \left[N^\dagger \nabla^2 N + \left[\nabla^2 N\right]^\dagger N\right]\ , \tag{241}$$

$$H_{\rm CT2,4} = i\, C_4' \int d\mathbf{x}\, \left[\left[N^\dagger \nabla N\right]\cdot\left[(\nabla N)^\dagger \times \boldsymbol{\sigma} N\right]+\left[(\nabla N)^\dagger N\right]\cdot\left[N^\dagger \boldsymbol{\sigma} \times \nabla N\right]\right], \tag{242}$$

$$H_{\rm CT2,5} = i\, C_5' \int d\mathbf{x}\, \left[N^\dagger N\right] \left[(\nabla N)^\dagger \cdot \boldsymbol{\sigma} \times \nabla N\right]\ , \tag{243}$$

$$H_{\text{CT2,6}} = i\,C_6' \int d\mathbf{x}\,\left[N^\dagger \boldsymbol{\sigma} N\right] \cdot \left[\left[\nabla N\right]^\dagger \times \nabla N\right] , \tag{244}$$

$$H_{\text{CT2,7}} = (C_7'\delta_{ik}\delta_{jl} + C_8'\delta_{il}\delta_{kj} + C_9'\delta_{ij}\delta_{kl})$$
$$\int d\mathbf{x}\,\left[\left[N^\dagger \sigma_k \partial_i N\right]\left[N^\dagger \sigma_l \partial_j N\right] + \left[(\partial_i N)^\dagger \sigma_k N\right]\left[(\partial_j N)^\dagger \sigma_l N\right]\right], \tag{245}$$

$$H_{\text{CT2,8}} = (C_{10}'\delta_{ik}\delta_{jl} + C_{11}'\delta_{il}\delta_{kj} + C_{12}'\delta_{ij}\delta_{kl})$$
$$\int d\mathbf{x}\,\left[N^\dagger \sigma_k \partial_i N\right]\left[(\partial_j N)^\dagger \sigma_l N\right] , \tag{246}$$

$$H_{\text{CT2,9}} = \left(\frac{1}{2} C_{13}'\left(\delta_{ik}\delta_{jl} + \delta_{il}\delta_{kj}\right) + C_{14}'\delta_{ij}\delta_{kl}\right)$$
$$\int d\mathbf{x}\,\left[(\partial_i N)^\dagger \sigma_k \partial_j N + (\partial_j N)^\dagger \sigma_k \partial_i N\right]\left[N^\dagger \sigma_l N\right] . \tag{247}$$

For brevity the spatial dependence of the nucleon fields has been suppressed.

Finally, when discussing the renormalization of the two-body currents at tree level in Sec. IV.2.4, we also need to consider the following Hamiltonians involving three- and four-pion interactions,

$$H_{3\pi NN} = -\frac{g_A}{F_\pi^3} \int d\mathbf{x}\,\boldsymbol{\pi}^2(\mathbf{x})\,N^\dagger(\mathbf{x})\,\left[\boldsymbol{\sigma} \cdot \nabla \pi_a(\mathbf{x})\right]\,\tau_a\,N(\mathbf{x}) , \tag{248}$$

$$H_{4\pi} = \frac{1}{2\,F_\pi^2} \int d\mathbf{x}\,\left[\left[\boldsymbol{\pi}^2(\mathbf{x})\,\boldsymbol{\Pi}^2(\mathbf{x}) - \boldsymbol{\pi}^2(\mathbf{x})\,\nabla \pi_a(\mathbf{x}) \cdot \nabla \pi_a(\mathbf{x}) + \text{h.c.}\right] - m_\pi^2\,\left[\boldsymbol{\pi}^2(\mathbf{x})\right]^2\right] , \tag{249}$$

obtained by including corrections up to $\boldsymbol{\pi}^2(\mathbf{x})/F_\pi^2$ in the expansion of D^{-1} factors, where $D \equiv 1 + \boldsymbol{\pi}^2(\mathbf{x})/F_\pi^2$, entering the chiral Lagrangians [1].

A.2   ELECTROMAGNETIC INTERACTIONS

In this section we list the electromagnetic interaction Hamiltonians of 'minimal' and 'non-minimal' nature.

A.2.1   Minimal Electromagnetic Hamiltonians

The 'minimal' Hamiltonians are obtained from the strong Hamiltonians by gauging the pion and nucleon derivative couplings:

$$\nabla \pi_\mp(\mathbf{x}) \rightarrow \left[\nabla \mp i\,e\mathbf{A}(\mathbf{x})\right]\pi_\mp(\mathbf{x}) , \tag{250}$$

$$\nabla N(\mathbf{x}) \rightarrow \left[\nabla - i\,e\,e_N\mathbf{A}(\mathbf{x})\right]N(\mathbf{x}) , \tag{251}$$

where $e > 0$ is the charge, $e_N = (1 + \tau_z)/2$, and $\mathbf{A}(\mathbf{x})$ is the photon field given in Eq. (15). As an example, we discuss more in detail the derivation of the $\gamma\pi\pi$ interaction. The free pion Hamiltonian reads

$$
\begin{aligned}
H_\pi &= \int d\mathbf{x} \left[\Pi_+(\mathbf{x}) \Pi_-(\mathbf{x}) + \nabla\pi_+(\mathbf{x}) \cdot \nabla\pi_-(\mathbf{x}) + m_\pi^2\, \pi_+(\mathbf{x})\, \pi_-(\mathbf{x}) \right] \\
&+ \frac{1}{2} \int d \left[\mathbf{x}\, \Pi_z^2(\mathbf{x}) + \nabla^2\pi_z(\mathbf{x}) + m_\pi^2\pi_z^2(\mathbf{x}) \right] ,
\end{aligned}
\tag{252}
$$

where we have separated the charged from the neutral pion field components. Minimal substitution into the charged pion derivative couplings leads to

$$
\begin{aligned}
H_\pi &\rightarrow\ H_\pi + H_{\pi\pi\gamma} = H_\pi - \int d\mathbf{x}\, \mathbf{A}(\mathbf{x}) \cdot \mathbf{j}_\pi(\mathbf{x}) \\
&= H_\pi + i\, e \int d\mathbf{x}\, \mathbf{A}(\mathbf{x}) \cdot \left[\pi_+(\mathbf{x})\nabla\pi_-(\mathbf{x}) - \nabla\pi_+(\mathbf{x})\pi_-(\mathbf{x}) \right] ,
\end{aligned}
\tag{253}
$$

where we have kept terms linear in the vector field $\mathbf{A}(\mathbf{x})$, and $\mathbf{j}_\pi(\mathbf{x})$ is the pion current defined as

$$
\mathbf{j}_\pi(\mathbf{x}) = -i\, e\, \left[\pi_+(\mathbf{x})\nabla\pi_-(\mathbf{x}) - \nabla\pi_+(\mathbf{x})\pi_-(\mathbf{x}) \right] .
\tag{254}
$$

In terms of the isospin cartesian components π_a, the $\gamma\pi\pi$ Hamiltonian is then given by

$$
H_{\pi\pi\gamma} = -e\, \epsilon_{abz} \int d\mathbf{x}\, \mathbf{A}(\mathbf{x}) \cdot \left[\nabla\pi_a(\mathbf{x}) \right] \pi_b(\mathbf{x}) .
\tag{255}
$$

Similarly, minimal substitution in the pion derivative couplings entering the Hamiltonians of Eqs.(235)-(236) and Eqs. (248)-(249) leads to the corresponding electromagnetic interaction Hamiltonians

$$
H_{\gamma\pi NN} = -e\frac{g_A}{F_\pi}\epsilon_{abz} \int d\mathbf{x}\, \mathbf{A}(\mathbf{x}) \cdot N^\dagger(\mathbf{x})\, \boldsymbol{\sigma}\, \tau_a N(\mathbf{x})\, \pi_b(\mathbf{x}) ,
\tag{256}
$$

$$
H_{\gamma\pi\pi NN} = -\frac{e}{2\, m_N}\frac{1}{F_\pi^2} \int d\mathbf{x}\, \mathbf{A}(\mathbf{x}) \cdot \left[N^\dagger(\mathbf{x})\left[i\,(\overrightarrow{\nabla} - \overleftarrow{\nabla}) + \boldsymbol{\sigma} \times (\overrightarrow{\nabla} + \overleftarrow{\nabla}) \right] \tau_a N(\mathbf{x}) \right]
$$
$$
\times \left[\pi_a(\mathbf{x})\pi_z(\mathbf{x}) - \delta_{a,z}\boldsymbol{\pi}^2(\mathbf{x}) \right] ,
\tag{257}
$$

$$
H_{\gamma 3\pi NN} = e\frac{g_A}{F_\pi^3}\epsilon_{abz} \int d\mathbf{x}\, \mathbf{A}(\mathbf{x}) \cdot N^\dagger(\mathbf{x})\, \boldsymbol{\sigma}\, \tau_a N(\mathbf{x})\, \pi_b(\mathbf{x})\, \boldsymbol{\pi}^2(\mathbf{x}) ,
\tag{258}
$$

$$
H_{\gamma 4\pi} = e\frac{2}{F_\pi^2}\, \epsilon_{abz} \int d\mathbf{x}\, \mathbf{A}(\mathbf{x}) \cdot \left[\nabla\pi_a(\mathbf{x}) \right] \pi_b(\mathbf{x})\boldsymbol{\pi}^2(\mathbf{x}) .
\tag{259}
$$

The electromagnetic Hamiltonians from four-nucleon contact interactions are obtained by minimal substitution in the derivatives acting on the nucleon' fields entering

Eqs.(239)-(247):

$$
\begin{aligned}
H_{\mathrm{CT}\gamma,1} &= -i\,e\,C_1' \int d\mathbf{x}\,\mathbf{A}\cdot \Big[[N^\dagger(\overrightarrow{\nabla}-\overleftarrow{\nabla})N](N^\dagger e_N N) \\
&\quad + (N^\dagger e_N N)[N^\dagger(\overrightarrow{\nabla}-\overleftarrow{\nabla})N]\Big]\,,
\end{aligned}
\tag{260}
$$

$$
H_{\mathrm{CT}\gamma,2} = -i\,e\,C_2' \int d\mathbf{x}\,\mathbf{A}\cdot \Big[(N^\dagger e_N N)\,[(\nabla N)^\dagger N] - (N^\dagger\nabla N)(N^\dagger e_N N)\Big]\,,
\tag{261}
$$

$$
H_{\mathrm{CT}\gamma,3} = -i\,e\,C_3' \int d\mathbf{x}\,\mathbf{A}\cdot (2\,N^\dagger N)[N^\dagger(\overrightarrow{\nabla}-\overleftarrow{\nabla})e_N N]\,,
\tag{262}
$$

$$
\begin{aligned}
H_{\mathrm{CT}\gamma,4} &= e\,C_4' \int d\mathbf{x}\,\mathbf{A}\cdot \Big[[N^\dagger(\overrightarrow{\nabla}+\overleftarrow{\nabla})N] \times (N^\dagger\boldsymbol{\sigma}\,e_N N) \\
&\quad + (N^\dagger e_N N)[N^\dagger(\overrightarrow{\nabla}+\overleftarrow{\nabla})\times \boldsymbol{\sigma}N]\Big]\,,
\end{aligned}
\tag{263}
$$

$$
H_{\mathrm{CT}\gamma,5} = e\,C_5' \int d\mathbf{x}\,\mathbf{A}\cdot (N^\dagger N)[N^\dagger(\overrightarrow{\nabla}+\overleftarrow{\nabla})\times \boldsymbol{\sigma}\,e_N N]\,,
\tag{264}
$$

$$
H_{\mathrm{CT}\gamma,6} = e\,C_6' \int d\mathbf{x}\,\mathbf{A}\cdot (N^\dagger\boldsymbol{\sigma}N)\times [N^\dagger(\overrightarrow{\nabla}+\overleftarrow{\nabla})e_N N]\,,
\tag{265}
$$

$$
\begin{aligned}
H_{\mathrm{CT}\gamma,7} &= -i\,e\,(C_7'\,\delta_{ik}\,\delta_{jl} + C_8'\,\delta_{il}\,\delta_{kj} + C_9'\,\delta_{ij}\,\delta_{kl}) \\
&\quad \times \int d\mathbf{x}\Big[A_j\,[N^\dagger(\overrightarrow{\partial_i}-\overleftarrow{\partial_i})\,\sigma_k N](N^\dagger\,\sigma_l\,e_N N) \\
&\quad + A_i\,(N^\dagger\,\sigma_k\,e_N N)\,[N^\dagger(\overrightarrow{\partial_j}-\overleftarrow{\partial_j})\,\sigma_l N]\Big]\,,
\end{aligned}
\tag{266}
$$

$$
\begin{aligned}
H_{\mathrm{CT}\gamma,8} &= i\,e\,(C_{10}'\,\delta_{ik}\,\delta_{jl} + C_{11}'\,\delta_{il}\,\delta_{kj} + C_{12}'\,\delta_{ij}\,\delta_{kl}) \\
&\quad \times \int d\mathbf{x}\,\Big[A_j\,(N^\dagger\,\sigma_k\,\partial_i N)\,(N^\dagger\,\sigma_l\,e_N N) \\
&\quad - A_i\,(N^\dagger\,\sigma_k\,e_N N)[(\partial_j N)^\dagger\,\sigma_l\,N]\Big]\,,
\end{aligned}
\tag{267}
$$

$$
\begin{aligned}
H_{\mathrm{CT}\gamma,9} &= i\,e\,\left(\frac{1}{2}\,C_{13}'\,(\delta_{ik}\,\delta_{jl} + \delta_{il}\,\delta_{kj}) + C_{14}'\,\delta_{ij}\,\delta_{kl}\right) \\
&\quad \times \int d\mathbf{x}\Big[A_j\,[N^\dagger(\overrightarrow{\partial_i}-\overleftarrow{\partial_i})\,\sigma_k\,e_N N](N^\dagger\,\sigma_l\,N) \\
&\quad + A_i\,[N^\dagger(\overrightarrow{\partial_j}-\overleftarrow{\partial_j})\,\sigma_k\,e_N N](N^\dagger\,\sigma_l\,N)\Big]\,.
\end{aligned}
\tag{268}
$$

A.2.2 Non-minimal Electromagnetic Hamiltonians

The interactions of individual nucleons with the electromagnetic field are described by the following Hamiltonian:

$$
\begin{aligned}
H_{\gamma NN} &= \frac{e}{2\,m_N} \int d\mathbf{x}\,N^\dagger(\mathbf{x})\Big[i\,e_N\left[-\overleftarrow{\nabla}\cdot\mathbf{A}(\mathbf{x}) + \mathbf{A}(\mathbf{x})\cdot\overrightarrow{\nabla}\right] \\
&\quad - \mu_N\,\boldsymbol{\sigma}\cdot\nabla\times\mathbf{A}(\mathbf{x})\Big]N(\mathbf{x})\,,
\end{aligned}
\tag{269}
$$

with

$$\kappa_N = (\kappa_S + \kappa_V \tau_z)/2 \ , \qquad \mu_N = e_N + \kappa_N \ , \tag{270}$$

where κ_S and κ_V are the isoscalar and isovector combinations of the anomalous magnetic moments of the proton and neutron ($\kappa_S = -0.12$ n.m. and $\kappa_V = 3.706$ n.m.). The expression in Eq. (269) results from considering the non-relativistic limit of the effective Hamiltonian with non-minimal couplings

$$H_{\gamma NN}^{\mathrm{R}} = e \int \mathrm{d}\mathbf{x} \, \overline{\psi}_N(\mathbf{x}) \left[e_N \, A^\mu(\mathbf{x}) \gamma_\mu + \frac{\kappa_N}{4 \, m_N} \sigma_{\mu\nu} F^{\mu\nu}(\mathbf{x}) \right] \psi_N(\mathbf{x}) \ , \tag{271}$$

where $\psi_N(\mathbf{x})$ is the spinor fields describing the nucleon, and $F^{\nu\lambda}(\mathbf{x})$ is the electromagnetic field tensor. The Bjorken and Drell conventions [56] are used for relativistic four-vectors, γ-matrices, and Dirac spin-1/2 spinors, except that the latter are taken to be normalized as $u^\dagger(\mathbf{p}, s) u(\mathbf{p}, s) = 1$.

In addition to the one-body electromagnetic Hamiltonians, there is a $\gamma \pi NN$ coupling Hamiltonian involving gradients acting on the pion field and on the vector potential respectively [6], whose expression is

$$\begin{aligned} H_{\gamma\pi NN}^{(2)} = & \ \frac{e}{F_\pi} \int \mathrm{d}\mathbf{x} \, N^\dagger(\mathbf{x}) \Big[d_8' \, \nabla \pi_z(\mathbf{x}) + d_9' \, \tau_a \, \nabla \pi_a(\mathbf{x}) \\ & - \ d_{21}' \, \epsilon_{zab} \, \tau_a \, \boldsymbol{\sigma} \times \nabla \pi_b(\mathbf{x}) \Big] N(\mathbf{x}) \cdot \nabla \times \mathbf{A}(\mathbf{x}) \ , \end{aligned} \tag{272}$$

and d_8', d_9', and d_{21}' are related to the original couplings given by Fettes $et \ al.$ [6] via $d_8' = 8 \, [d_8 + g_A/(64 \, m_N^2)]$ and similarly for d_9', and $d_{21}' = 2 \, d_{21} + d_{22}$.

Finally, there is a set of contact non-minimal electromagnetic interactions Hamiltonians involving two additional LECs [21].

$$\begin{aligned} H_{\mathrm{CT}\gamma,\mathrm{nm}} = & \ \frac{e}{2} \int \mathrm{d}\mathbf{x} \, \Big[C_{15}' \, N^\dagger \sigma_k N \, N^\dagger N \\ & + \ C_{16}' \, \big(N^\dagger \sigma_k \, \tau_z N \, N^\dagger N - N^\dagger \sigma_k N \, N^\dagger \tau_z N \big) \Big] \epsilon_{ijk} \, F_{ij} \ . \end{aligned} \tag{273}$$

APPENDIX B

STRONG AND ELECTROMAGNETIC VERTICES

The interaction Hamiltonians in Appendices A.1 and A.2 are assumed to be normal-ordered. Explicit expressions for the associated vertices are easily derived (these expressions include the $1/\sqrt{2\omega_{k_i}}$ factors from pion fields) :

B.1 STRONG-INTERACTION VERTICES

$$\langle \mathbf{p}', \chi'; \mathbf{k}, a \mid H_{\pi NN} \mid \mathbf{p}, \chi \rangle = -i\frac{g_A}{F_\pi}\frac{\boldsymbol{\sigma} \cdot \mathbf{k}}{\sqrt{2\,\omega_k}}\,\tau_a \ , \tag{274}$$

$$\langle \mathbf{p}', \chi'; \mathbf{k}_1, a; \mathbf{k}_2, b \mid H_{\pi\pi NN} \mid \mathbf{p}, \chi \rangle = -\frac{i}{F_\pi^2}\frac{\omega_{k_1} - \omega_{k_2}}{\sqrt{4\,\omega_{k_1}\,\omega_{k_2}}}\,\epsilon_{abc}\tau_c \ , \tag{275}$$

$$\langle \mathbf{p}'_1, \chi'_1; \mathbf{p}'_2, \chi'_2 \mid H_{\mathrm{CT},0} \mid \mathbf{p}_1, \chi_1; \mathbf{p}_2, \chi_2 \rangle = \sum_{\alpha=S,T} C_\alpha\,\boldsymbol{\Gamma}_{1\alpha} \cdot \boldsymbol{\Gamma}_{2\alpha} \ , \tag{276}$$

$$\begin{aligned}
\langle \mathbf{p}', \chi'; \mathbf{k}_1, a; \mathbf{k}_2, b; \mathbf{k}_3, c \mid H_{3\pi NN} \mid \mathbf{p}, \chi \rangle = {} & \frac{2\,i\,g_A}{F_\pi^3}\frac{1}{\sqrt{8\,\omega_{k_1}\,\omega_{k_2}\,\omega_{k_3}}}\Big(\boldsymbol{\sigma} \cdot \mathbf{k}_1\,\tau_a\,\delta_{bc} \\
& + \ \boldsymbol{\sigma} \cdot \mathbf{k}_2\,\tau_b\,\delta_{ca} + \boldsymbol{\sigma} \cdot \mathbf{k}_3\,\tau_c\,\delta_{ab}\Big) \ , \tag{277}
\end{aligned}$$

$$\begin{aligned}
\langle \mathbf{k}_1, a; \mathbf{k}_2, b; \mathbf{k}_3, c; \mathbf{k}_4, d \mid H_{4\pi} \mid 0 \rangle = {} & -\frac{4}{F_\pi^2}\frac{1}{\sqrt{16\,\omega_{k_1}\,\omega_{k_2}\,\omega_{k_3}\,\omega_{k_4}}} \\
& \times \ \Big[\delta_{ab}\,\delta_{cd}\left(k_{1\mu}k_2^\mu + k_{3\mu}k_4^\mu + m_\pi^2\right) \\
& + \ \delta_{ac}\,\delta_{bd}\left(k_{1\mu}k_3^\mu + k_{2\mu}k_4^\mu + m_\pi^2\right) \\
& + \ \delta_{ad}\,\delta_{bc}\left(k_{1\mu}k_4^\mu + k_{2\mu}k_3^\mu + m_\pi^2\right)\Big] \ . \tag{278}
\end{aligned}$$

B.2 ELECTROMAGNETIC-INTERACTION VERTICES

$$\langle \mathbf{p}', \chi'; \mathbf{k}, a \mid H_{\gamma\pi NN} \mid \mathbf{p}, \chi; \mathbf{q}, \lambda \rangle = e\frac{g_A}{F_\pi}\frac{\boldsymbol{\sigma}}{\sqrt{2\,\omega_k}} \cdot \frac{\hat{\mathbf{e}}_{\mathbf{q}\lambda}}{\sqrt{2\,\omega_q}}\,\epsilon_{zab}\tau_b \ , \tag{279}$$

$$\langle \mathbf{k}_1, a; \mathbf{k}_2, b \mid H_{\gamma\pi\pi} \mid \mathbf{q}, \lambda \rangle = i\,e\,\frac{\mathbf{k}_1 - \mathbf{k}_2}{\sqrt{4\,\omega_{k_1}\,\omega_{k_2}}} \cdot \frac{\hat{\mathbf{e}}_{\mathbf{q}\lambda}}{\sqrt{2\,\omega_q}}\,\epsilon_{zab} \ , \tag{280}$$

$$\langle \mathbf{p}', \chi'; \mathbf{k}_1, a; \mathbf{k}_2, b \mid H_{\gamma\pi\pi NN} \mid \mathbf{p}, \chi; \mathbf{q}, \lambda \rangle = -\frac{e}{F_\pi^2} \frac{1}{\sqrt{4\,\omega_{k_1}\,\omega_{k_2}}}$$

$$\frac{\hat{\mathbf{e}}_{\mathbf{q}\lambda}}{\sqrt{2\,\omega_q}} \cdot \frac{(\mathbf{p}' + \mathbf{p}) + i\,\boldsymbol{\sigma} \times (\mathbf{p}' - \mathbf{p})}{2\,m_N} \quad (\delta_{az}\,\tau_b + \delta_{bz}\,\tau_a - 2\,\delta_{ab}\,\tau_z) \ , \quad (281)$$

$$\langle \mathbf{p}', \chi'; \mathbf{k}_1, a; \mathbf{k}_2, b; \mathbf{k}_3, c \mid H_{\gamma\,3\pi NN} \mid \mathbf{p}, \chi; \mathbf{q}, \lambda \rangle = -2\,e\,\frac{g_A}{F_\pi^3} \frac{\boldsymbol{\sigma}}{\sqrt{8\,\omega_{k_1}\,\omega_{k_2}\,\omega_{k_3}}} \cdot \frac{\hat{\mathbf{e}}_{\mathbf{q}\lambda}}{\sqrt{2\,\omega_q}}$$

$$\tau_d \ (\epsilon_{zad}\,\delta_{bc} + \epsilon_{zbd}\,\delta_{ca} + \epsilon_{zcd}\,\delta_{ab}) \ , \quad (282)$$

$$\langle \mathbf{k}_1, a; \mathbf{k}_2, b; \mathbf{k}_3, c; \mathbf{k}_4, d \mid H_{\gamma\,4\pi} \mid \mathbf{q}, \lambda \rangle = -i\,e\,\frac{4}{F_\pi^2} \frac{1}{\sqrt{16\,\omega_{k_1}\,\omega_{k_2}\,\omega_{k_3}\,\omega_{k_4}}} \frac{\hat{\mathbf{e}}_{\mathbf{q}\lambda}}{\sqrt{2\,\omega_q}}$$

$$\Big[\delta_{cd}\,\epsilon_{zab}(\mathbf{k}_1 - \mathbf{k}_2) + \delta_{ab}\,\epsilon_{zcd}(\mathbf{k}_3 - \mathbf{k}_4)$$

$$+ \delta_{bd}\,\epsilon_{zac}(\mathbf{k}_1 - \mathbf{k}_3) + \delta_{ad}\,\epsilon_{zbc}(\mathbf{k}_2 - \mathbf{k}_3)$$

$$+ \delta_{ac}\,\epsilon_{zbd}(\mathbf{k}_2 - \mathbf{k}_4) + \delta_{bc}\,\epsilon_{zad}(\mathbf{k}_1 - \mathbf{k}_4) \Big] \ , (283)$$

$$\langle \mathbf{p}', \chi' \mid H_{\gamma NN} \mid \mathbf{p}, \chi; \mathbf{q}, \lambda \rangle = -\frac{e}{2\,m_N} \frac{\hat{\mathbf{e}}_{\mathbf{q}\lambda}}{\sqrt{2\,\omega_q}} \cdot \Big[e_N\,(\mathbf{p}' + \mathbf{p}) + i\,\mu_n\,\boldsymbol{\sigma} \times \mathbf{q} \Big]. \ (284)$$

In these expressions $\mathbf{p}$ denotes the nucleon momentum in spin-isospin states specified by χ, while the $\mathbf{k}$'s and $a, b, \ldots$ denote pion momenta in isospin states $a, b, \ldots$, and $\mathbf{q}$ and λ the photon momentum and polarization state. For brevity, on the r.h.s. of the equations above the spin-isospin states of the nucleon as well as the δ-functions enforcing three-momentum conservation, are not shown explicitly. In Eq. (278), the notation $k_i^\mu k_{j\mu}$ denotes the combination $\omega_{k_i}\omega_{k_j} - \mathbf{k}_i \cdot \mathbf{k}_j$. Finally, vertices in which one or more pions are in the initial state are obtained from those listed in Eqs. (274)–(275), (277), (278), (280), and (283) by replacing $\mathbf{k}_i \to -\mathbf{k}_i$ and/or $\omega_{k_i} \to -\omega_{k_i}$ (of course, the energy replacements are not to be carried out in the pion-field normalization factors). For example,

$$\langle \mathbf{p}', \chi'; \mathbf{k}_1, a \mid H_{\pi\pi NN} \mid \mathbf{p}, \chi; \mathbf{k}_2, b \rangle = -\frac{i}{F_\pi^2} \frac{\omega_{k_1} + \omega_{k_2}}{\sqrt{4\,\omega_{k_1}\,\omega_{k_2}}} \epsilon_{abc}\tau_c \ . \quad (285)$$

B.3 FOUR-NUCLEON VERTICES

Strong Contact Vertices

The vertices induced by the contact interaction Hamiltonians are listed below. The notation is the same as in Appendix B.1, but for

$$\langle H_{\text{CT2D}_i} \rangle \equiv \langle \mathbf{p}_1', \chi_1'; \mathbf{p}_2', \chi_2' \mid H_{\text{CT2D},i} \mid \mathbf{p}_1, \chi_1; \mathbf{p}_2, \chi_2 \rangle \ , \qquad i = 1, \ldots, 9 \ , \quad (286)$$

and

$$\langle H_{\mathrm{CT2D,1}} \rangle \;=\; -2\,C_1'\,(\mathbf{p}_1 \cdot \mathbf{p}_2 + \mathbf{p}_1' \cdot \mathbf{p}_2')\;, \tag{287}$$

$$\langle H_{\mathrm{CT2D,2}} \rangle \;=\; C_2'\,(\mathbf{p}_1 \cdot \mathbf{p}_2' + \mathbf{p}_1' \cdot \mathbf{p}_2)\;, \tag{288}$$

$$\langle H_{\mathrm{CT2D,3}} \rangle \;=\; -\,C_3'\,\bigl(\mathbf{p}_1^2 + \mathbf{p}_1'^{\,2} + \mathbf{p}_2^2 + \mathbf{p}_2'^{\,2}\bigr)\;, \tag{289}$$

$$\langle H_{\mathrm{CT2D,4}} \rangle \;=\; i\,C_4'\,(\boldsymbol{\sigma}_1 + \boldsymbol{\sigma}_2) \cdot (\mathbf{p}_1 \times \mathbf{p}_2' - \mathbf{p}_1' \times \mathbf{p}_2)\;, \tag{290}$$

$$\langle H_{\mathrm{CT2D,5}} \rangle \;=\; i\,C_5'\,(\boldsymbol{\sigma}_1 \cdot \mathbf{p}_1 \times \mathbf{p}_1' + \boldsymbol{\sigma}_2 \cdot \mathbf{p}_2 \times \mathbf{p}_2')\;, \tag{291}$$

$$\langle H_{\mathrm{CT2D,6}} \rangle \;=\; -i\,C_6'\,(\boldsymbol{\sigma}_1 \cdot \mathbf{p}_2 \times \mathbf{p}_2' + \boldsymbol{\sigma}_2 \cdot \mathbf{p}_1 \times \mathbf{p}_1')\;, \tag{292}$$

$$\begin{aligned}
\langle H_{\mathrm{CT2D,7}} \rangle \;=\; -2\bigl[& C_7'\,(\boldsymbol{\sigma}_1 \cdot \mathbf{p}_1\,\boldsymbol{\sigma}_2 \cdot \mathbf{p}_2 + \boldsymbol{\sigma}_1 \cdot \mathbf{p}_1'\,\boldsymbol{\sigma}_2 \cdot \mathbf{p}_2') \\
& +C_8'\,(\boldsymbol{\sigma}_1 \cdot \mathbf{p}_2\,\boldsymbol{\sigma}_2 \cdot \mathbf{p}_1 + \boldsymbol{\sigma}_1 \cdot \mathbf{p}_2'\,\boldsymbol{\sigma}_2 \cdot \mathbf{p}_1') \\
& +C_9'\,\boldsymbol{\sigma}_1 \cdot \boldsymbol{\sigma}_2\,(\mathbf{p}_1 \cdot \mathbf{p}_2 + \mathbf{p}_1' \cdot \mathbf{p}_2') \bigr]\;,
\end{aligned} \tag{293}$$

$$\begin{aligned}
\langle H_{\mathrm{CT2D,8}} \rangle \;=\; \bigl[& C_{10}'\,(\boldsymbol{\sigma}_1 \cdot \mathbf{p}_1'\,\boldsymbol{\sigma}_2 \cdot \mathbf{p}_2 + \boldsymbol{\sigma}_1 \cdot \mathbf{p}_1\,\boldsymbol{\sigma}_2 \cdot \mathbf{p}_2')\;, \\
& +\,C_{11}'\,(\boldsymbol{\sigma}_1 \cdot \mathbf{p}_2'\,\boldsymbol{\sigma}_2 \cdot \mathbf{p}_1 + \boldsymbol{\sigma}_1 \cdot \mathbf{p}_2\,\boldsymbol{\sigma}_2 \cdot \mathbf{p}_1')\;, \\
& +\,C_{12}'\,\boldsymbol{\sigma}_1 \cdot \boldsymbol{\sigma}_2\,(\mathbf{p}_1 \cdot \mathbf{p}_2' + \mathbf{p}_1' \cdot \mathbf{p}_2) \bigr]\;,
\end{aligned} \tag{294}$$

$$\begin{aligned}
\langle H_{\mathrm{CT2D,9}} \rangle \;=\; C_{13}'\bigl(& \boldsymbol{\sigma}_1 \cdot \mathbf{p}_2\,\boldsymbol{\sigma}_2 \cdot \mathbf{p}_2' + \boldsymbol{\sigma}_1 \cdot \mathbf{p}_1'\,\boldsymbol{\sigma}_2 \cdot \mathbf{p}_1 \\
& +\boldsymbol{\sigma}_1 \cdot \mathbf{p}_2'\,\boldsymbol{\sigma}_2 \cdot \mathbf{p}_2 + \boldsymbol{\sigma}_1 \cdot \mathbf{p}_1\,\boldsymbol{\sigma}_2 \cdot \mathbf{p}_1' \bigr) \\
& +2\,C_{14}'\,\boldsymbol{\sigma}_1 \cdot \boldsymbol{\sigma}_2\,(\mathbf{p}_1 \cdot \mathbf{p}_1' + \mathbf{p}_2 \cdot \mathbf{p}_2')\;.
\end{aligned} \tag{295}$$

Electromagnetic Contact Vertices

The vertices induced by the contact electromagnetic-interaction Hamiltonians are listed below. The notation is the same as in Appendix B.1, but for

$$\langle H_{\mathrm{CT\gamma},i} \rangle \;\equiv\; \langle \mathbf{p}_1', \chi_1'; \mathbf{p}_2', \chi_2' \mid H_{\mathrm{CT\gamma},i} \mid \mathbf{p}_1, \chi_1; \mathbf{p}_2, \chi_2; \mathbf{q}, \lambda \rangle\;, \qquad i = 1, \ldots, 9\;,$$

$$\langle H_{\mathrm{CT\gamma,nm}} \rangle \;\equiv\; \langle \mathbf{p}_1', \chi_1'; \mathbf{p}_2', \chi_2' \mid H_{\mathrm{CT\gamma,nm}} \mid \mathbf{p}_1, \chi_1; \mathbf{p}_2, \chi_2; \mathbf{q}, \lambda \rangle\;, \tag{296}$$

and

$$\langle H_{\mathrm{CT\gamma,1}} \rangle \;=\; 2\,e\,C_1'\left[e_1\,(\mathbf{p}_2 + \mathbf{p}_2') + e_2\,(\mathbf{p}_1 + \mathbf{p}_1') \right] \cdot \frac{\hat{\mathbf{e}}_{\mathbf{q}\lambda}}{\sqrt{2\,\omega_q}}\;, \tag{297}$$

$$\langle H_{\mathrm{CT\gamma,2}} \rangle \;=\; -\,e\,C_2'\left[e_1\,(\mathbf{p}_2 + \mathbf{p}_2') + e_2\,(\mathbf{p}_1 + \mathbf{p}_1') \right] \cdot \frac{\hat{\mathbf{e}}_{\mathbf{q}\lambda}}{\sqrt{2\,\omega_q}}\;, \tag{298}$$

$$\langle H_{\mathrm{CT\gamma,3}} \rangle \;=\; 2\,e\,C_3'\left[e_1\,(\mathbf{p}_1 + \mathbf{p}_1') + e_2\,(\mathbf{p}_2 + \mathbf{p}_2') \right] \cdot \frac{\hat{\mathbf{e}}_{\mathbf{q}\lambda}}{\sqrt{2\,\omega_q}}\;, \tag{299}$$

$$\langle H_{\text{CT}\gamma,4} \rangle = -i\,e\,C_4'\,(\boldsymbol{\sigma}_1 + \boldsymbol{\sigma}_2) \times \left[e_1\,(\mathbf{p}_2 - \mathbf{p}_2') + e_2\,(\mathbf{p}_1 - \mathbf{p}_1')\right] \cdot \frac{\hat{\mathbf{e}}_{\mathbf{q}\lambda}}{\sqrt{2\,\omega_q}} \,, \tag{300}$$

$$\langle H_{\text{CT}\gamma,5} \rangle = -i\,e\,C_5'\left[e_1\,\boldsymbol{\sigma}_1 \times (\mathbf{p}_1 - \mathbf{p}_1') + e_2\,\boldsymbol{\sigma}_2 \times (\mathbf{p}_2 - \mathbf{p}_2')\right] \cdot \frac{\hat{\mathbf{e}}_{\mathbf{q}\lambda}}{\sqrt{2\,\omega_q}} \,, \tag{301}$$

$$\langle H_{\text{CT}\gamma,6} \rangle = i\,e\,C_6'\left[e_1\,\boldsymbol{\sigma}_2 \times (\mathbf{p}_1 - \mathbf{p}_1') + e_2\,\boldsymbol{\sigma}_1 \times (\mathbf{p}_2 - \mathbf{p}_2')\right] \cdot \frac{\hat{\mathbf{e}}_{\mathbf{q}\lambda}}{\sqrt{2\,\omega_q}} \,, \tag{302}$$

$$\begin{aligned}
\langle H_{\text{CT}\gamma,7} \rangle = 2\,e\,\Big[& C_7'[e_1\,(\mathbf{p}_2 + \mathbf{p}_2') \cdot \boldsymbol{\sigma}_2\,\boldsymbol{\sigma}_1 + e_2\,(\mathbf{p}_1 + \mathbf{p}_1') \cdot \boldsymbol{\sigma}_1\,\boldsymbol{\sigma}_2] \\
& + C_8'[e_1\,(\mathbf{p}_2 + \mathbf{p}_2') \cdot \boldsymbol{\sigma}_1\,\boldsymbol{\sigma}_2 + e_2\,(\mathbf{p}_1 + \mathbf{p}_1') \cdot \boldsymbol{\sigma}_2\,\boldsymbol{\sigma}_1] \\
& + C_9'\,\boldsymbol{\sigma}_1 \cdot \boldsymbol{\sigma}_2[e_1\,(\mathbf{p}_2 + \mathbf{p}_2') + e_2\,(\mathbf{p}_1 + \mathbf{p}_1')]\Big] \cdot \frac{\hat{\mathbf{e}}_{\mathbf{q}\lambda}}{\sqrt{2\,\omega_q}} \,,
\end{aligned} \tag{303}$$

$$\begin{aligned}
\langle H_{\text{CT}\gamma,8} \rangle = -e\,\Big[& C_{10}'[e_1\,(\mathbf{p}_2 + \mathbf{p}_2') \cdot \boldsymbol{\sigma}_2\,\boldsymbol{\sigma}_1 + e_2\,(\mathbf{p}_1 + \mathbf{p}_1') \cdot \boldsymbol{\sigma}_1\,\boldsymbol{\sigma}_2] \\
& + C_{11}'[e_1\,(\mathbf{p}_2 + \mathbf{p}_2') \cdot \boldsymbol{\sigma}_1\,\boldsymbol{\sigma}_2 + e_2\,(\mathbf{p}_1 + \mathbf{p}_1') \cdot \boldsymbol{\sigma}_2\,\boldsymbol{\sigma}_1] \\
& + C_{12}'\,\boldsymbol{\sigma}_1 \cdot \boldsymbol{\sigma}_2[e_1\,(\mathbf{p}_2 + \mathbf{p}_2') + e_2\,(\mathbf{p}_1 + \mathbf{p}_1')]\Big] \cdot \frac{\hat{\mathbf{e}}_{\mathbf{q}\lambda}}{\sqrt{2\,\omega_q}} \,,
\end{aligned} \tag{304}$$

$$\begin{aligned}
\langle H_{\text{CT}\gamma,9} \rangle = -e\,\Big[& C_{13}'\big[e_1\,(\mathbf{p}_1 + \mathbf{p}_1') \cdot \boldsymbol{\sigma}_1\,\boldsymbol{\sigma}_2 + e_1\,(\mathbf{p}_1 + \mathbf{p}_1') \cdot \boldsymbol{\sigma}_2\,\boldsymbol{\sigma}_1 \\
& \qquad + e_2\,(\mathbf{p}_2 + \mathbf{p}_2') \cdot \boldsymbol{\sigma}_1\,\boldsymbol{\sigma}_2 + e_2\,(\mathbf{p}_2 + \mathbf{p}_2') \cdot \boldsymbol{\sigma}_2\,\boldsymbol{\sigma}_1\big] \\
& + 2\,C_{14}'\,\boldsymbol{\sigma}_1 \cdot \boldsymbol{\sigma}_2[e_1\,(\mathbf{p}_1 + \mathbf{p}_1') + e_2\,(\mathbf{p}_2 + \mathbf{p}_2')]\Big] \cdot \frac{\hat{\mathbf{e}}_{\mathbf{q}\lambda}}{\sqrt{2\,\omega_q}} \,,
\end{aligned} \tag{305}$$

$$\begin{aligned}
\langle H_{\text{CT}\gamma,\text{nm}} \rangle = {} & i\,e\,C_{15}'\,(\boldsymbol{\sigma}_1 + \boldsymbol{\sigma}_2) \times \mathbf{q} \cdot \frac{\hat{\mathbf{e}}_{\mathbf{q}\lambda}}{\sqrt{2\,\omega_q}} \\
& + C_{16}'\,(\tau_{1,z} - \tau_{2,z})\,(\boldsymbol{\sigma}_1 - \boldsymbol{\sigma}_2) \times \mathbf{q} \cdot \frac{\hat{\mathbf{e}}_{\mathbf{q}\lambda}}{\sqrt{2\,\omega_q}} \,.
\end{aligned} \tag{306}$$

APPENDIX C

DIMENSIONAL REGULARIZATION OF KERNELS

In this appendix we report a list of general integration formulae [18, 20], useful to carry out the regularization of the various kernels occurring in the potential and current operators. Dimensional regularization is used for the sake of simplicity: being a mass independent regularization scheme, it respects the power counting. In this sense, dimensional regularization is the natural regularization scheme for effective field theories. In dimensional regularization the loop momenta are formally unbounded. Nevertheless, once the renormalization program has been carried out—once all divergences have been absorbed by a redefinition of the LECs at a given order—the choice of the regularization procedure becomes irrelevant at that order [57], even though the numerical values of the renormalized LECs will depend on the adopted renormalization scheme. We are dealing here with perturbative renormalization: the effective field theory is renormalizable order by order in the chiral expansion, as we explicitly verify up to N³LO for the currents and the potential. We do not address the issue of non-perturbative renormalization of the dynamical equation used to compute observables (*e.g.* the Lippmann-Schwinger equation), for which we adopt a cut-off regularization.

C.1 USEFUL INTEGRALS

We utilize the Feynman parameterization

$$\frac{1}{AB} = \int_0^1 \mathrm{d}y \, \frac{1}{[yA + (1-y)B]^2} \, , \tag{307}$$

and, in order to simplify the energy factors entering the kernels, we make use of the integral representations [58]:

$$\frac{1}{\omega_+ + \omega_-} = \frac{2}{\pi} \int_0^\infty \mathrm{d}\beta \, \frac{\beta^2}{(\omega_+^2 + \beta^2)(\omega_-^2 + \beta^2)} \, , \tag{308}$$

$$\frac{1}{\omega_+ \omega_- (\omega_+ + \omega_-)} = \frac{2}{\pi} \int_0^\infty \mathrm{d}\beta \, \frac{1}{(\omega_+^2 + \beta^2)(\omega_-^2 + \beta^2)} \, . \tag{309}$$

Having defined

$$\int_{\mathbf{p}} \equiv \int \frac{\mathrm{d}^d p}{(2\pi)^d} \, , \tag{310}$$

we have:

$$\int_{\mathbf{p}} \frac{1}{(p^2 + A)^\alpha} = \frac{1}{(4\pi)^{d/2}} \frac{\Gamma(\alpha - d/2)}{\Gamma(\alpha)} A^{-(\alpha - d/2)} , \tag{311}$$

$$\int_{\mathbf{p}} \frac{p^2}{(p^2 + A)^\alpha} = \frac{1}{(4\pi)^{d/2}} \frac{d}{2} \frac{\Gamma(\alpha - d/2 - 1)}{\Gamma(\alpha)} A^{-(\alpha - d/2 - 1)} , \tag{312}$$

$$\int_{\mathbf{p}} \frac{p^4}{(p^2 + A)^\alpha} = \frac{1}{(4\pi)^{d/2}} \frac{d\,(d+2)}{4} \frac{\Gamma(\alpha - d/2 - 2)}{\Gamma(\alpha)} A^{-(\alpha - d/2 - 2)} , \tag{313}$$

where $\Gamma(z)$ is the Γ-function satisfying $z\,\Gamma(z) = \Gamma(z+1)$, with asymptotic behavior for $z \to 0$ given by

$$\Gamma(z) = \frac{1}{z} - \gamma + \left(\frac{\gamma^2}{2} + \frac{\pi^2}{12} \right) z + O(z^2) , \tag{314}$$

and $\gamma \approx 0.5772$ is the Euler-Mascheroni constant. However, we note that, in order to preserve physical dimensions, a renormalization scale μ has to be introduced, and therefore a factor μ^{3-d} should be understood in Eq. (310).

Finally, we use the following relations [59] to evaluate

$$\int \mathrm{d}x \ln|x^2 - a^2| = x \ln|x^2 - a^2| - 2\,x + a \ln\left| \frac{x+a}{x-a} \right| , \tag{315}$$

$$\int \mathrm{d}x\, x^2 \ln|x^2 - a^2| = \frac{1}{3}\left(x^3 \ln|x^2 - a^2| - \frac{2}{3}x^3 - 2\,a^2 x + a^3 \ln\left| \frac{x+a}{x-a} \right| \right) , \tag{316}$$

$$\int \mathrm{d}x\, x^4 \ln|x^2 - a^2| = \frac{1}{5}\left(x^5 \ln|x^2 - a^2| - \frac{2}{5}x^5 - \frac{2}{3}a^2 x^3 - 2\,a^4 x \right.$$
$$\left. + a^5 \ln\left| \frac{x+a}{x-a} \right| \right) . \tag{317}$$

C.2 REGULARIZATION OF THE KERNELS

As an example, we sketch the regularization of the kernel $I^{(0)}(k)$, given by

$$I^{(0)}(k) = \int_{\mathbf{p}} \frac{1}{\omega_+ \omega_- (\omega_+ + \omega_-)} = \frac{2}{\pi} \int_{\mathbf{p}} \int_0^\infty \mathrm{d}\beta \frac{1}{(\omega_+^2 + \beta^2)(\omega_-^2 + \beta^2)} , \tag{318}$$

where $\omega_\pm = \sqrt{(\mathbf{p} \pm \mathbf{k})^2 + 4\,m_\pi^2}$. Using the Feynman integral parameterization of Eq. (307) with $A = \omega_+^2 + \beta^2$ and $B = \omega_-^2 + \beta^2$, we obtain

$$I^{(0)}(k) = \frac{2}{\pi} \int_{\mathbf{p}} \int_0^1 \mathrm{d}y \int_0^\infty \mathrm{d}\beta \left[[\mathbf{p} + (2\,y - 1)\,\mathbf{k}]^2 + 4\,[m_\pi^2 - y\,(y-1)\,k^2] + \beta^2 \right]^{-2}$$

$$= \frac{1}{2} \int_{\mathbf{p}} \int_0^1 \mathrm{d}y \left[p^2 + 4\,[m_\pi^2 - y\,(y-1)\,k^2] \right]^{-3/2} , \tag{319}$$

where in the second line we have also shifted the integration variable $\mathbf{p} \to \mathbf{p} + (2\,y - 1)\,\mathbf{k}$. The integral over $\mathbf{p}$ is reduced to the form given in Eq. (311) with $d = 3$, $\alpha = 3/2$, and $A = 4\,[m_\pi^2 - y\,(y-1)\,k^2]$. With this choice of d and α, we are left with a Γ-function of vanishing argument. In order to isolate the divergent part of the integral, we set $d = 3 - \epsilon$ and study its asymptotic behavior for $\epsilon \to 0^+$. Using

$$\Gamma\left(\frac{\epsilon}{2}\right) = \frac{2}{\epsilon} - \gamma + O(\epsilon) , \tag{320}$$

$$\Gamma\left(\frac{3}{2}\right) = \frac{\sqrt{\pi}}{2} , \tag{321}$$

$$\left(\frac{A}{4\,\pi}\right)^{-\epsilon/2} = 1 - \frac{\epsilon}{2}\ln\frac{A}{4\,\pi} + O(\epsilon^2) , \tag{322}$$

we find, neglecting $O(\epsilon)$ terms,

$$I^{(0)}(k) = \frac{1}{8\,\pi^2}\left(\ln\pi + \frac{2}{\epsilon} - \gamma\right) - \frac{1}{8\,\pi^2}\int_0^1 \mathrm{d}y \ln\left[\frac{m_\pi^2}{\mu^2} - y\,(y-1)\,\frac{k^2}{\mu^2}\right] . \tag{323}$$

After setting $y \to (x+1)/2$ and making use of Eq. (315), we obtain:

$$I^{(0)}(k) = -\frac{1}{8\,\pi^2}\left(\frac{s}{k}\ln\frac{s+k}{s-k} - \frac{2}{\epsilon} + \gamma - \ln\pi + \ln\frac{m_\pi^2}{\mu^2} - 2\right) , \tag{324}$$

where $s = \sqrt{4\,m_\pi^2 + k^2}$.

The kernels

$$I^{(2)}(k) = \int_{\mathbf{p}} \frac{p^2}{\omega_+\,\omega_-\,(\omega_+ + \omega_-)} , \tag{325}$$

$$I_{ij}^{(2)}(\mathbf{k}) = \int_{\mathbf{p}} \frac{p_i\,p_j}{\omega_+\,\omega_-\,(\omega_+ + \omega_-)} , \tag{326}$$

can be easily evaluated as shown above. We find:

$$\begin{aligned}
I^{(2)}(k) &= \frac{1}{24\,\pi^2}\left[\frac{2\,s^3}{k}\ln\frac{s+k}{s-k} + 2\,k^2\left(-\frac{2}{\epsilon} + \gamma - \ln\pi + \ln\frac{m_\pi^2}{\mu^2} - \frac{5}{3}\right)\right.\\
&\quad + \left.18\,m_\pi^2\left(-\frac{2}{\epsilon} + \gamma - \ln\pi + \ln\frac{m_\pi^2}{\mu^2} - \frac{11}{9}\right)\right] ,
\end{aligned} \tag{327}$$

$$
\begin{aligned}
I_{ij}^{(2)}(\mathbf{k}) \;=\; & \frac{1}{24\,\pi^2}\,\delta_{ij}\left[\frac{s^3}{k}\ln\frac{s+k}{s-k} + k^2\left(-\frac{2}{\epsilon}+\gamma-\ln\pi+\ln\frac{m_\pi^2}{\mu^2}-2\right)\right.\\
& +\;6\,m_\pi^2\left(-\frac{2}{\epsilon}+\gamma-\ln\pi+\ln\frac{m_\pi^2}{\mu^2}-\frac{5}{3}\right)\Bigg]\\
& -\;\frac{1}{24\,\pi^2}\frac{k_i k_j}{k^2}\left[\frac{s^3}{k}\ln\frac{s+k}{s-k}\right.\\
& +\;k^2\left(-\frac{2}{\epsilon}+\gamma-\ln\pi+\ln\frac{m_\pi^2}{\mu^2}-\frac{8}{3}\right)-8\,m_\pi^2\Bigg]\,.
\end{aligned}
\tag{328}
$$

Next, we note that

$$
f(\omega_+,\omega_-)\equiv\frac{\omega_+^2+\omega_+\omega_-+\omega_-^2}{\omega_+^3\,\omega_-^3\,(\omega_++\omega_-)}=-\frac{1}{2}\frac{\mathrm{d}}{\mathrm{d}\,m_\pi^2}\frac{1}{\omega_+\,\omega_-\,(\omega_++\omega_-)}\,,
\tag{329}
$$

from which we obtain:

$$
J^{(0)}(k)\;=\;\int_{\mathbf{p}}f(\omega_+,\omega_-)=\frac{1}{8\,\pi^2}\frac{1}{k\,s}\ln\frac{s+k}{s-k}\,,
\tag{330}
$$

$$
\begin{aligned}
J^{(2)}(k)\;=\;\int_{\mathbf{p}}p^2 f(\omega_+,\omega_-)=&-\frac{1}{8\,\pi^2}\left[\frac{2\,s}{k}\ln\frac{s+k}{s-k}\right.\\
&+\;3\left(-\frac{2}{\epsilon}+\gamma-\ln\pi+\ln\frac{m_\pi^2}{\mu^2}-\frac{2}{3}\right)\Bigg]\,,
\end{aligned}
\tag{331}
$$

$$
\begin{aligned}
J_{ij}^{(2)}(\mathbf{k})\;=\;\int_{\mathbf{p}}p_i p_j f(\omega_+,\omega_-)=&-\frac{1}{8\,\pi^2}\delta_{ij}\left[\frac{s}{k}\ln\frac{s+k}{s-k}\right.\\
&+\;\left(-\frac{2}{\epsilon}+\gamma-\ln\pi+\ln\frac{m_\pi^2}{\mu^2}-\frac{4}{3}\right)\Bigg]\\
&+\;\frac{1}{8\,\pi^2}\frac{k_i k_j}{k^2}\left(\frac{s}{k}\ln\frac{s+k}{s-k}-2\right)\,,
\end{aligned}
\tag{332}
$$

$$
\begin{aligned}
J^{(4)}(k)\;=\;\int_{\mathbf{p}}p^4 f(\omega_+,\omega_-)=&\frac{1}{8\,\pi^2}\left[\frac{8\,s^3}{3\,k}\ln\frac{s+k}{s-k}\right.\\
&+\;30\,m_\pi^2\left(-\frac{2}{\epsilon}+\gamma-\ln\pi+\ln\frac{m_\pi^2}{\mu^2}-\frac{29}{45}\right)\\
&+\;\frac{5}{3}\,k^2\left(-\frac{2}{\epsilon}+\gamma-\ln\pi+\ln\frac{m_\pi^2}{\mu^2}-\frac{12}{5}\right)\Bigg]\,.
\end{aligned}
\tag{333}
$$

The set of kernels involving the energy factor

$$
\frac{2\,\omega_++\omega_-}{2\,\omega_+^3\,\omega_-\,(\omega_++\omega_-)^2}
$$

can be reduced to those of type $J^{(2n)}(k)$ by noting that

$$
\int_{\mathbf{p}}\frac{2\,\omega_++\omega_-}{2\,\omega_+^3\,\omega_-\,(\omega_++\omega_-)^2}=\frac{1}{4}\int_{\mathbf{p}}\frac{\omega_+^2+\omega_+\omega_-+\omega_-^2}{\omega_+^3\,\omega_-^3\,(\omega_++\omega_-)}=\frac{1}{4}\,J^{(0)}(k)\,,
\tag{334}
$$

and similarly for $J^{(2)}(k)$, $J^{(2)}_{ij}(\mathbf{k})$, $J^{(4)}(k)$.

The kernels involving the energy factor $g(\omega_+, \omega_-)$,

$$
\begin{aligned}
g(\omega_+, \omega_-) &= \frac{3}{2} \frac{2\omega_+ + \omega_-}{\omega_+^5 \omega_- (\omega_+ + \omega_-)^2} + \frac{\omega_+ + 2\omega_-}{\omega_+^3 \omega_-^3 (\omega_+ + \omega_-)^2} \\
&= -\frac{1}{2} \frac{\mathrm{d}}{\mathrm{d}\, m_\pi^2} \frac{2\omega_+ + \omega_-}{2\omega_+^3 \omega_- (\omega_+ + \omega_-)^2} \ ,
\end{aligned}
\tag{335}
$$

easily follow from

$$
K^{(0)}(k) = \int_\mathbf{p} g(\omega_+, \omega_-) = -\frac{1}{8} \frac{\mathrm{d}}{\mathrm{d}m_\pi^2}\, J^{(0)}(k) = \frac{1}{16} \frac{\mathrm{d}^2}{\mathrm{d}(m_\pi^2)^2}\, I^{(0)}(k) \ ,
\tag{336}
$$

and similarly for $K^{(2n)}(k)$, leading to:

$$
K^{(0)}(k) = \int_\mathbf{p} g(\omega_+, \omega_-) = \frac{1}{64\pi^2} \left[\frac{2}{k\, s^3} \ln \frac{s+k}{s-k} + \frac{1}{s^2\, m_\pi^2} \right] \ ,
\tag{337}
$$

$$
K^{(2)}(k) = \int_\mathbf{p} p^2\, g(\omega_+, \omega_-) = \frac{1}{64\pi^2} \left[\frac{4}{k\, s} \ln \frac{s+k}{s-k} + \frac{1}{m_\pi^2} \right] \ ,
\tag{338}
$$

$$
\begin{aligned}
K^{(2)}_{ij}(\mathbf{k}) &= \int_\mathbf{p} p_i\, p_j\, g(\omega_+, \omega_-) \\
&= \frac{1}{64\pi^2} \delta_{ij} \left[\frac{2}{k\, s} \ln \frac{s+k}{s-k} \right] - \frac{1}{64\pi^2} \frac{k_i k_j}{k^2} \left[\frac{2}{k\, s} \ln \frac{s+k}{s-k} - \frac{1}{m_\pi^2} \right] \ ,
\end{aligned}
\tag{339}
$$

$$
\begin{aligned}
K^{(4)}(k) &= \int_\mathbf{p} p^4\, g(\omega_+, \omega_-) \\
&= -\frac{1}{64\pi^2} \left[\frac{16\, s}{k} \ln \frac{s+k}{s-k} - \frac{k^2}{m_\pi^2} + 30 \left(-\frac{2}{\epsilon} + \gamma - \ln \pi + \ln \frac{m_\pi^2}{\mu^2} \right) \right] ,
\end{aligned}
\tag{340}
$$

$$
\begin{aligned}
K^{(4)}_{ij}(\mathbf{k}) &= \int_\mathbf{p} p^2\, p_i\, p_j\, g(\omega_+, \omega_-) \\
&= -\frac{1}{64\pi^2} \delta_{ij} \left[\frac{8\, s}{k} \ln \frac{s+k}{s-k} + 10 \left(-\frac{2}{\epsilon} + \gamma - \ln \pi + \ln \frac{m_\pi^2}{\mu^2} - \frac{8}{15} \right) \right] \\
&\quad + \frac{1}{64\pi^2} \frac{k_i k_j}{k^2} \left[\frac{8\, s}{k} \ln \frac{s+k}{s-k} + \frac{k^2}{m_\pi^2} - 16 \right] \ .
\end{aligned}
\tag{341}
$$

Finally, for the kernel entering diagram e) in Fig. 7, we obtain

$$
\begin{aligned}
L(k) &= \int_\mathbf{p} \frac{(\omega_+ - \omega_-)^2}{\omega_+ \omega_- (\omega_+ + \omega_-)} = \int_\mathbf{p} \left[-\frac{4}{(\omega_+ + \omega_-)} + \frac{2}{\omega_+} \right] \\
&= -\frac{1}{6\pi^2} \left[\frac{s^3}{k} \ln \frac{s+k}{s-k} - 8\, m_\pi^2 + k^2 \left(-\frac{2}{\epsilon} + \gamma - \ln \pi + \ln \frac{m_\pi^2}{\mu^2} - \frac{8}{3} \right) \right] ,
\end{aligned}
\tag{342}
$$

while for the constants $M^{(n)}$ entering Eqs. (80)–(81),

$$M^{(1)} = \int_{\mathbf{p}} \frac{1}{\omega_p} = \frac{m_\pi^2}{8\pi^2} \left(-\frac{2}{\epsilon} + \gamma - \ln 4\pi + \ln \frac{m_\pi^2}{\mu^2} - 1 \right) , \tag{343}$$

$$M^{(3)} = \int_{\mathbf{p}} \frac{p^2}{\omega_p^3} = \frac{3\,m_\pi^2}{8\pi^2} \left(-\frac{2}{\epsilon} + \gamma - \ln 4\pi + \ln \frac{m_\pi^2}{\mu^2} - \frac{1}{3} \right) . \tag{344}$$

APPENDIX D

RECOIL CORRECTIONS

Consider the set of time-ordered diagrams, displayed in Fig. 40 and denoted as type i) in Fig. 28. It is easily seen that recoil corrections in diagrams a)+b) and i)+j) cancel out the contributions associated with diagrams c)+d) and k)+l), respectively, so that the expression for type i) diagrams in Fig. 28—which happens to vanish—results from diagrams e)-h). Let N denote the product of the four vertices in diagrams a)-d); then the contribution of diagrams a)+b) is given by
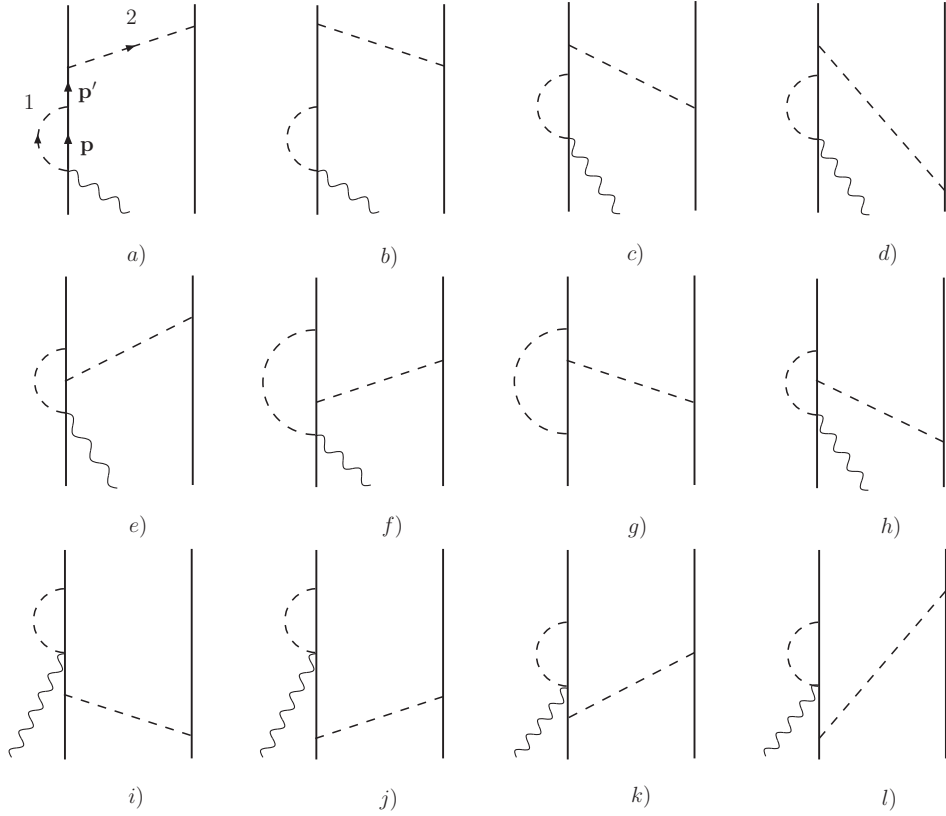

FIG. 40: Set of time-ordered diagrams for the contribution illustrated by the single diagram i) in Fig. 28. Notation as in Fig. 20.

$$
\text{a) + b) of Fig. 14} = \frac{N}{(E_i - E_p' - E_2 + i\eta)(E_i - E_p - E_2 - \omega_1 + i\eta)} \times
$$
$$
\left[\frac{1}{E_i - E_1' - E_2 - \omega_2 + i\eta} + \frac{1}{E_i - E_p' - E_2' - \omega_2 + i\eta}\right] , \quad (345)
$$

where the labeling of the momenta is as in panel a), and E_p and E'_p are the energies of the intermediate nucleons. The expression in square brackets above can be expanded as

$$\left[\dots\right] \simeq -\frac{1}{\omega_2}\left[2 + \frac{E_i - E'_p - E_2}{\omega_2}\right] \ , \tag{346}$$

where use has been made of (overall) energy conservation, $E_i = E'_1 + E'_2$, and hence

$$\text{a}) + \text{b}) \text{ of Fig. 14} = (\text{terms in iterated LS equation}) - \frac{N}{\omega_2^2\,(E_i - E_p - E_2 - \omega_1 + i\eta)} \ . \tag{347}$$

The second term above in the static limit reduces to $N/(\omega_1\,\omega_2^2)$, which exactly
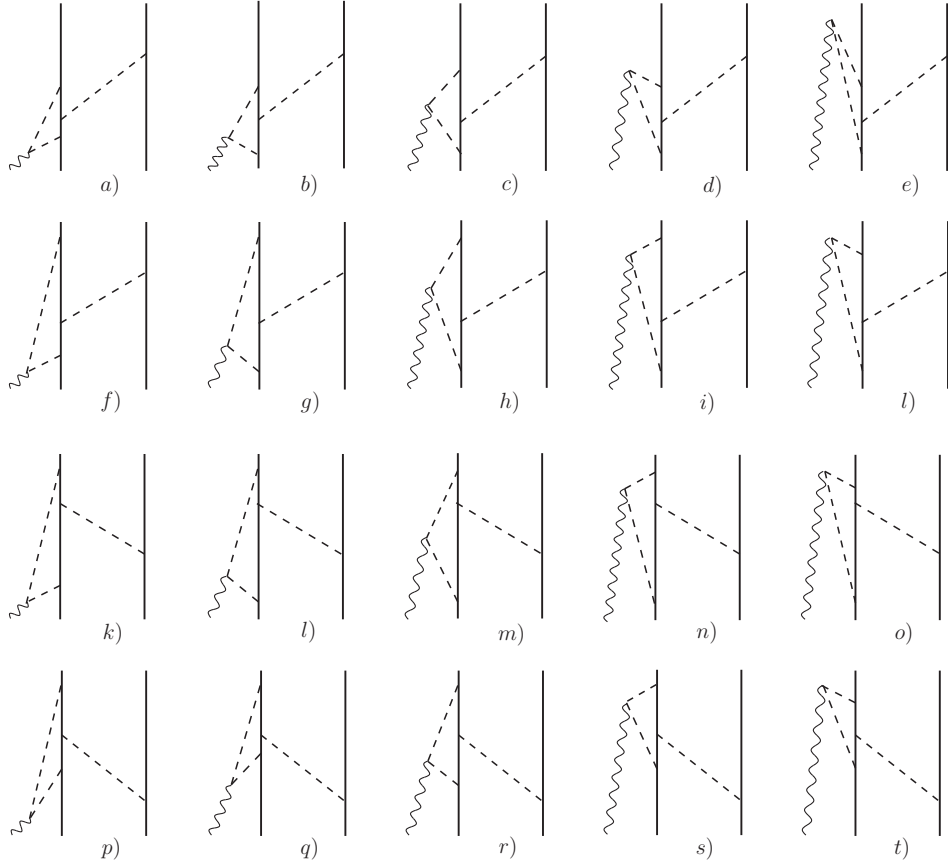

FIG. 41: Subset of time-ordered diagrams for the contribution illustrated by the single diagram j) in Fig. 28. See text for discussion. Notation as in Fig. 20.

cancels the contribution of diagrams c)+d). These exact cancellations persist also in the k)-l) as well as u)-v) type diagrams of Figs. 28 and 29, so that in computing their

contributions we only take into account the subset of (twenty, see below) time-ordered diagrams of topology as shown in those figures.

For the type j) contribution we find that the cancellation between irreducible and recoil-corrected reducible diagrams is only partial, and the result given in Eq. (170) corresponds to taking into account only the irreducible diagrams illustrated in Fig. 41 (the same subset considered in the evaluation of type u)-v) above). However, the remaining irreducible and recoil-corrected reducible diagrams produce an additional contribution of the form

$$
e \frac{g_A^4}{F_\pi^4} N_{ij}(\mathbf{q}) \left[(\boldsymbol{\tau}_1 \times \boldsymbol{\tau}_2)_z (\mathbf{q} \times \mathbf{k}_2)_j + \tau_{2,z} \left[\mathbf{q} \times (\boldsymbol{\sigma}_1 \times \mathbf{k}_2) \right]_j \right] \frac{\boldsymbol{\sigma}_2 \cdot \mathbf{k}_2}{\omega_{k_2}^2}
$$
$$
+ \ e \frac{g_A^4}{2\,F_\pi^4} N_i(\mathbf{q})\, \tau_{2,z} \frac{\boldsymbol{\sigma}_1 \cdot \mathbf{k}_2\, \boldsymbol{\sigma}_2 \cdot \mathbf{k}_2}{\omega_{k_2}^2} + 1 \rightleftharpoons 2 \ , \tag{348}
$$

where the kernels N_{ij} and N_i are

$$
N_{ij}(\mathbf{q}) \ = \ \int_\mathbf{p} \frac{p_i\, p_j}{\omega_+^2\, \omega_-^2\, (\omega_+ + \omega_-)} \ , \tag{349}
$$
$$
N_i(\mathbf{q}) \ = \ \int_\mathbf{p} p_i\, (p^2 - q^2) \frac{\omega_+ - \omega_-}{\omega_+^2\, \omega_-^2\, (\omega_+ + \omega_-)^2} \ , \tag{350}
$$

which, however, does not lead to a Hermitian current density, since this would require $\mathbf{j}(\mathbf{k}_1, \mathbf{k}_2) = \mathbf{j}^\dagger(-\mathbf{k}_1, -\mathbf{k}_2)$. We have ignored this contribution.

APPENDIX E

TRANSLATIONALLY INVARIANT MAGNETIC MOMENTS

In this appendix we list the translationally invariant contributions to the magnetic moment—Eq. (212)—associated with currents a)-e) and i) in Fig. 25. Currents of type a), d), g), and i) have been properly renormalized, and their final expressions are given in Eqs. (147)–(150). The translationally invariant magnetic moments generated by them is obtained by inserting the corresponding expressions into Eq. (212). In particular, the magnetic moment associated with the currents of type c) and g) vanishes, while the remaining renormalized currents give

$$
\overline{\boldsymbol{\mu}}_{\mathrm{T,a}}(\mathbf{k}) = \frac{e\,g_A^2}{8\,\pi^2 F_\pi^4}\,\tau_{2,z} G(k)\left[\left(1 - \frac{2\,m_\pi^2}{4\,m_\pi^2 + k^2}\right)\boldsymbol{\sigma}_1 + \frac{2\,m_\pi^2}{4\,m_\pi^2 + k^2}\frac{\mathbf{k}\,\boldsymbol{\sigma}_1\cdot\mathbf{k}}{k^2}\right]
$$
$$
+ \frac{e\,g_A^2}{8\,\pi^2 F_\pi^4}\,\tau_{2,z}\left(\boldsymbol{\sigma}_1 - \frac{\mathbf{k}\,\boldsymbol{\sigma}_1\cdot\mathbf{k}}{k^2}\right) + 1 \rightleftharpoons 2\ , \tag{351}
$$

$$
\overline{\boldsymbol{\mu}}_{\mathrm{T,d}}(\mathbf{k}) = -\frac{e\,g_A^4}{8\pi^2\,F_\pi^4}\tau_{2,z}\,G(k)\left[\left[1 - \frac{2\,m_\pi^2}{4\,m_\pi^2 + k^2} - \frac{8\,m_\pi^4}{(4\,m_\pi^2 + k^2)^2}\right]\boldsymbol{\sigma}_1\right.
$$
$$
+ \left[-\frac{2\,m_\pi^2}{4\,m_\pi^2 + k^2} + \frac{8\,m_\pi^4}{(4\,m_\pi^2 + k^2)^2}\right]\frac{\mathbf{k}\,\boldsymbol{\sigma}_1\cdot\mathbf{k}}{k^2}\Bigg]
$$
$$
- \frac{e\,g_A^4}{8\pi^2\,F_\pi^4}\tau_{2,z}\left[\left(1 - \frac{4\,m_\pi^2}{4\,m_\pi^2 + k^2}\right)\boldsymbol{\sigma}_1\right.
$$
$$
- \left.\left(1 - \frac{4\,m_\pi^2}{4\,m_\pi^2 + k^2}\right)\frac{\mathbf{k}\,\boldsymbol{\sigma}_1\cdot\mathbf{k}}{k^2}\right] + 1 \rightleftharpoons 2\ , \tag{352}
$$

$$
\overline{\boldsymbol{\mu}}_{\mathrm{T,i}}(\mathbf{k}) = \frac{e\,g_A^2}{2\pi^2\,F_\pi^2}\,\tau_{1,z}\,(C_S\,\boldsymbol{\sigma}_1 - C_T\,\boldsymbol{\sigma}_2) + 1 \rightleftharpoons 2\ . \tag{353}
$$

To derive the translationally invariant magnetic moments due to currents of type b) and e) in Fig. 25, we utilize a different strategy. We start from the expressions given in Eqs. (131) and (134). The kernels of these currents involve three pion energies, ω_i with $i = 1, 2, 3$, corresponding to the internal exchanged pions, and their explicit expressions, with reference to Fig. 25, are

$$
\begin{aligned}
\omega_1 &= \left(\mathbf{q}_1^2 + m_\pi^2\right)^{1/2} = \left[(\mathbf{k}_1 + \mathbf{q}_2)^2 + m_\pi^2\right]^{1/2}\ ,\\
\omega_2 &= \left(\mathbf{q}_2^2 + m_\pi^2\right)^{1/2}\ ,\\
\omega_3 &= \left(\mathbf{q}_3^2 + m_\pi^2\right)^{1/2} = \left[(\mathbf{k}_2 - \mathbf{q}_2)^2 + m_\pi^2\right]^{1/2}\ ,
\end{aligned} \tag{354}
$$

with the additional constraint $\mathbf{q}_1 + \mathbf{q}_3 = \mathbf{k}_1 + \mathbf{k}_2 = \mathbf{q}$. We evaluate the magnetic moment associated with these currents by inserting Eqs. (131) and (134) into Eq. (212). The corresponding magnetic moments are then expressed in terms of kernels involving only two-pion energies, since at $\mathbf{q} = 0$ the following relation holds true $\omega_1|_{\mathbf{q}=0} = \omega_3|_{\mathbf{q}=0}$. The dimensional regularization of the kernels is then carried out as illustrated in Appendix C. In particular, we find that the magnetic moments for the currents of type b), and e) read

$$
\begin{aligned}
\boldsymbol{\mu}_{\mathrm{T,b}}(\mathbf{k}) \;=\;& \frac{e\,g_A^2}{2\,F_\pi^4}\,\tau_{2,z}\,\Bigg[\Big[J_{ij}^{(2)}(\mathbf{k}) - k_i\,k_j\,J^{(0)}(k)\Big]\,\sigma_{1,j} \\
& - \Big[J^{(2)}(k) - k^2 J^{(0)}(k)\Big]\,\boldsymbol{\sigma}_1\Bigg] + 1 \rightleftharpoons 2 \;,
\end{aligned}
\tag{355}
$$

$$
\begin{aligned}
\boldsymbol{\mu}_{\mathrm{T,e}}(\mathbf{k}) \;=\;& \frac{2\,e\,g_A^4}{F_\pi^4}\,\tau_{2,z}\,\Bigg[\Big[K^{(4)}(k) - 2\,k^2 K^{(2)}(k) + k^4 K^{(0)}(k)\Big]\,\boldsymbol{\sigma}_1 \\
& - \Big[K_{ij}^{(4)}(\mathbf{k}) - k^2 K_{ij}^{(2)}(\mathbf{k}) - k_i k_j K^{(2)}(k) + k_i k_j k^2 K^{(0)}(k)\Big]\,\sigma_{1,j} \\
& - 4\,\epsilon_{ijk}\,k_k\,(\boldsymbol{\sigma}_1 \times \mathbf{k})_l\,K_{jl}^{(2)}(\mathbf{k})\Bigg] + 1 \rightleftharpoons 2 \;,
\end{aligned}
\tag{356}
$$

where the kernels $J^{(n)}$, and $K^{(n)}$ are defined in Appendix C. The infinite parts of the kernels are dropped, since in Sec. IV.2.3 we showed that the infinite parts of the currents of type b), and e) contribute to renormalize the LECs entering the contact currents at N³LO, therefore the renormalized operators follow from the finite part of the kernels, and are given by

$$
\begin{aligned}
\overline{\boldsymbol{\mu}}_{\mathrm{T,b}}(\mathbf{k}) \;=\;& \frac{e\,g_A^2}{8\,\pi^2 F_\pi^4}\,\tau_{2,z}\,G(k)\Bigg[\left(1 - \frac{2\,m_\pi^2}{4\,m_\pi^2 + k^2}\right)\boldsymbol{\sigma}_1 + \frac{2\,m_\pi^2}{4\,m_\pi^2 + k^2}\,\frac{\mathbf{k}\,\boldsymbol{\sigma}_1\cdot\mathbf{k}}{k^2}\Bigg] \\
& - \frac{e\,g_A^2}{8\,\pi^2 F_\pi^4}\,\tau_{2,z}\,\frac{\mathbf{k}\,\boldsymbol{\sigma}_1\cdot\mathbf{k}}{k^2} + 1 \rightleftharpoons 2 \;,
\end{aligned}
\tag{357}
$$

$$
\begin{aligned}
\overline{\boldsymbol{\mu}}_{\mathrm{T,e}}(\mathbf{k}) \;=\;& -\frac{e\,g_A^4}{8\pi^2\,F_\pi^4}\tau_{2,z}\,G(k)\Bigg[\left[1 + \frac{6\,m_\pi^2}{4\,m_\pi^2 + k^2} - \frac{8\,m_\pi^4}{(4\,m_\pi^2 + k^2)^2}\right]\boldsymbol{\sigma}_1 \\
& + \left[4 - \frac{10\,m_\pi^2}{4\,m_\pi^2 + k^2} + \frac{8\,m_\pi^4}{(4\,m_\pi^2 + k^2)^2}\right]\frac{\mathbf{k}\,\boldsymbol{\sigma}_1\cdot\mathbf{k}}{k^2}\Bigg] \\
& - \frac{e\,g_A^4}{8\pi^2\,F_\pi^4}\tau_{2,z}\Bigg[\left(1 - \frac{4\,m_\pi^2}{4\,m_\pi^2 + k^2}\right)\boldsymbol{\sigma}_1 \\
& - \left(5 - \frac{4\,m_\pi^2}{4\,m_\pi^2 + k^2}\right)\frac{\mathbf{k}\,\boldsymbol{\sigma}_1\cdot\mathbf{k}}{k^2}\Bigg] + 1 \rightleftharpoons 2 \;.
\end{aligned}
\tag{358}
$$

After combining Eqs. (351)–(353) with Eqs. (357)–(358) we are left with the expression of the magnetic moment given in Eq. (213), where we dropped the overline indicating that the LECs have been properly renormalized.

VITA

Saori Pastore

Department of PHYSICS

Old Dominion University

Norfolk, VA 23529

Education:

Old Dominion University, Norfolk, Virginia

M.S., May 2005.

Università degli Studi di Lecce, Lecce, Italy

Degree in Physics, *summa cum laude*, December 2002,

Thesis: Violazione di parità nei processi di diffusione di elettroni da nuclei,

(Parity violating effects in electron-nucleus scattering processes),

Advisor: Dr. G. Co'.

Publications:

L. Girlanda, S. Pastore, R. Schiavilla, M. Viviani,

'Relativity constraints on the two-nucleon contact interaction',

Phys. Rev. C **81**, 034005 (2010).

S. Pastore, L. Girlanda, R. Schiavilla, M. Viviani, and R.B. Wiringa,

'Electromagnetic Currents and Magnetic Moments in χEFT',

Phys. Rev. C **80**, 034004 (2009).

S. Pastore, R. Schiavilla, and J.L. Goity,

'Electromagnetic two-body currents of one- and two-pion range',

Phys. Rev. C **78**, 064002 (2008).

S. Pastore, R. Schiavilla, and J.L. Goity,
'Electromagnetic processes in χEFT', conference proceedings for the 4th Asia-Pacific Conference on *Few-Body Problems in Physics*, Mod. Phys. Lett. **A24**, 931 (2009).

L. Girlanda, S. Pastore, R. Schiavilla, and M. Viviani,
'Electromagnetic structure and reactions of few-nucleon systems in χEFT', conference proceedings for the 19th International IUPAP Conference on *Few-Body Problems in Physics*, EPJ Web of Conferences **3**, 01004 (2010).

L. Girlanda, S. Pastore, R. Schiavilla, and M. Viviani,
'Electromagnetic processes in a chiral effective field theory framework', conference proceedings for the 5th International Conference on *Quarks and Nuclear Physics*, to appear in Chinese Physics C, arXiv:0912.2763.

Workshops and Conferences:

S. Pastore, 'Electromagnetic processes in a chiral effective field theory framework', invited talk at the **5th International Conference on Quarks and Nuclear Physics**, Institute of High Energy Physics, Beijing, China, September 2009

S. Pastore, 'Electromagnetic two-body currents of one- and two-pion range', talk at the **2009 INT Program: Effective Field Theories and the Many-Body Problem**, Institute for Nuclear Theory, Seattle, WA, May 2009

S. Pastore, 'Electromagnetic two-body currents of one- and two-pion range', talk at the **2008 Annual Fall Meeting of the APS Division of Nuclear Physics**, Oakland, CA, October 2008

Typeset using LaTeX.